A Hollow-Shaft Rotor Cooling System for Automotive Traction Motors

Gai Yaohui

A thesis submitted for the degree of

Doctor of Philosophy

School of Engineering

Abstract

Automotive traction motors with demanding power density requirements, are exposed to higher temperature operations, which can have a detrimental effect on the efficiency, reliability and life expectancy of these motors. In order to minimize this level of damaging, a highly effective cooling and ventilating system has to be incorporated into the optimal design of such motors. It can ensure sufficient heat removal from the machine inside. On top of this, a better cooling performance of the rotor will result in higher power density, better field weakening capability and reduced costs.

This thesis addresses a hollow-shaft rotor cooling system for automotive traction motors. In such cooling system, the coolant is forced to pass through a hollow-shaft in order to cool the motor. However, in such case, the heat transfer can be complex due to the secondary flow which will occur as a result of the shaft rotation. As a result, the convective heat transfer coefficient (HTC) correlation of a stationary case is invalid for a hollow-shaft rotor cooling system. The aim of this thesis is to investigate the effects of the rotational velocities, coolant flow rates and coolant temperature, on the thermal performance of this cooling method.

A simplified numerical model based on computational fluid dynamics (CFD) methods was developed to provide a qualitative understanding of the mechanism of convective heat transfer. Then a finite element model (FEM) was constructed to represent the heat transfer of the test rig by considering heat dissipation of conduction and convection. Experiments were then carried out to validate the accuracy of CFD models with the assistance of an analytical lumped-parameter thermal network (LPTN) approach. As a result of such analysis, two new dimensionless correlations of the Nusselt number with the Reynolds number are derived for turbulent and laminar flow, respectively. These correlations can be applied in different geometrical contexts with various axial and rotation flow rates.

Finally, an accurate evaluation of the flow resistance in a rotating shaft has been presented. The rotational friction loss factor in such a hollow-shaft is studied, where the effect of the shaft velocity as well as the coolant flow rate have been accounted for.

Acknowledgements

The author wishes to record his highly appreciation to Dr. James Widmer, Dr. Mohammad Kimiabeigi, Dr. Andy Steven and Prof. Barrie Mecrow who acted as supervisors. Their patient, encouragement, advice and constructive criticism contributed in no small measure to any merit this work may possess.

The author pays profound gratitude to Dr. Xu Deng, Dr. Rafal Wrobel and Dr. Glynn Atkinson for their generosity and selfless support to make this work possible.

The author is sincere grateful to his industrial supervisor Dr. Yew Chuan Chong, Lead Thermal Specialist of Motor Design Ltd, for providing technical aid and guidance throughout.

The author conveys the appreciation to John Smith, Chris Annan, Chris Manning, Allan Wheatley, Sam Burn, Gordon Marshall and James Richardson for their assistance and support on the experimental work.

Special thanks are due to all the UG lab colleagues and in particular Dr. Ruchao Pupadubsin for making author's PhD life more enjoyable.

The author records his deepest gratitude to his families for their love, encouragement and support during his study.

Finally, the author wishes to express the appreciation to Motor Design Ltd. and Newcastle University Overseas Research Scholarship (NUORS) for their financial support of this project.

Table of Contents

List of Figures

List of Tables

List of Symbols

Roman

A	Cross sectional area of a heat path (m^2).
A_i, A_o	Inlet and outlet cross section areas (m^2).
A_l	Linear current density (kA/m).
c_p	Specific heat capacity (J/(kg·K)).
C_f	Air friction coefficient (dimensionless).
D	Hydraulic diameter (m).
E	Electrical field (V/m).
f	Darcy friction factor (dimensionless).
f_s , f_r	Stationary and rotating friction loss factor (dimensionless).
F_g	Geometrical factor (dimensionless).
Gr	Grashof number (dimensionless).
g	Gravitational acceleration (m/s^2).
H	Fin extension (m).
h	Heat transfer coefficient (W/ (m^2·K)).
h_l	Latent heat (kJ/kg).
I_{rms}	RMS (root mean square) current of heater (A).
J	Current density (A/mm^2).
k	Turbulent kinetic energy (m^2/s^2).
k_l	Flow resistance coefficient (dimensionless).
k_s	Sudden expansion and contraction resistance coefficient (dimensionless).
L	Characteristic length of the surface, length of heat transfer path (m).
L_r, L_s	Rotation and stationary region length (m).
L_{ring}	The bearing ring thickness (m).
m	The fluid mass (kg/s).
N	The ratio of the tangential to axial flow velocity (dimensionless).
Nu	Nusselt number (dimensionless).
$Nu_{Natural}$	Natural Nusselt number (dimensionless).

Nu_{Forced}	Forced Nusselt number (dimensionless).
n	Number of fins (dimensionless).
P_a	The active heat transfer (W).
P_{ave}	The average power dissipated from the heater (W).
P_{iron}	Iron loss (W).
P_s	Heat transfer from the shaft to the coolant (W).
P_M, P_E	The mechanical losses and electrical losses (W).
p, P, p'	Pressure, time-averaged Pressure and fluctuating Pressure (Pa).
Δp	Pressure drop (Pa).
$\Delta\, p_s$, $\Delta\, p_r$	Static and rotational pressure drop (Pa).
p_{inlet} , p_{outlet}	Inlet and outlet pressure (Pa).
Pr	Prandtl number (dimensionless).
Q	Flow rate (m^3/s).
$q^{"}$	Heat flux (W/m^2)
R	Thermal resistance (K/W).
R_{cd_a}, R_{cd_r}	Axial and radial thermal resistances of the shaft (K/W).
R_{cd_w}	Thermal resistance of the flow (K/W).
R_{cv}	Thermal resistance of convective heat transfer from the shaft to the coolant (K/W).
R_{heater}	The electric resistance of heater (ohm).
$r_{inner,}\, r_{outer}$	Inner and outer radius of the shaft (m).
Re	Reynold number (dimensionless).
Re_r	Rotational Reynold number (dimensionless).
Re_δ	Couette–Reynolds number (dimensionless).
$T, \Delta T$	Temperature and temperature difference (K).
T_{wall}, T_{fluid}	Wall and fluid temperatures (K).
T_{inlet}, T_{outlet}	Inlet and outlet flow temperatures (K).
T_{inlet_a} , T_{outlet_a}	inlet and outlet flow temperatures in the active part (K).
$T_{ring}, T_{shaft/housing}$	Temperature of bearing and shaft / housing (K).
T_{iw}	Average temperature of the shaft's internal wall (K).
Ta	Taylor number (dimensionless).

t	Fin thickness (m).
S	Fin pitch length (m).
S_{ij}	Strain-rate tensor (s^{-1}).
u, U, u'	Fluid velocity, fluid time-averaged velocity and fluid fluctuating velocity (m/s).
U^+	Dimensionless flow velocity (dimensionless).
u_τ	Friction velocity (m/s).
V	Axial velocity (m/s).
V_r	Tangential velocity (m/s).
W_1, W_2, W_3	Values of the Wattmeter in the three layers of the active part (W).
y	Normal distance from the wall (m).
y^+	Dimensionless wall distance (dimensionless).

Greek

α	Thermal diffusivity (m^3/s).
β	Coefficient of the cubical expansion (dimensionless).
δ	Radial air-gap length (m).
δ_f, δ_i,	Average air gap between fitted bodies, initial interface clearance (m).
δ_{ij}	Kronecker delta (dimensionless).
ε	Turbulent dissipation rate (m^2/s^3); Relative error (dimensionless).
λ	Thermal conductivity (W/(m·K)).
μ	Dynamic viscosity (Pa·s).
μ_t	Turbulent viscosity (Pa·s).
υ	Kinematic viscosity (m^2/s).
ρ	Density (kg/m^3).
σ	Shear stress (kPa).
τ_{turb}	Reynolds stress tensor (Pa).
τ_w	Wall shear stress (Pa).
φ	The roughness coefficient (dimensionless).

ω	Specific dissipation rate (s^{-1}) and angular speed (rad/s).

List of Acronyms

CFD	Computational fluid dynamics.
EFC	Enclosed fan cooled.
EMs	Electric machines.
EVs	Electric vehicles.
FEM	Finite element model.
HTC	Heat transfer coefficient.
HEVs	Hybrid electric vehicles.
LPTN	Lumped parameter thermal network.
OFC	Open fan cooled.
RANS	Reynolds Averaged Navier-Stokes.
RST	Reynolds stress transport.
SST	Shear stress transport.
URANS	Unsteady Reynolds Averaged Navier-Stokes.

1 Introduction

1.1 Background

Climate change is currently having an impact on the weather and ecosystem of our planet. As a result, climate change includes not only what we mean by rising average temperatures, but also severe weather proceedings, shifting the wildlife populations and habitations, and a host of other effects. The increase in greenhouse gas concentrations as a result of human activity is the biggest cause. The main reason for such high levels of greenhouse gases is the burning of fossil fuels. Almost every single sector of the world economy, from manufacturing to agriculture to transportation to energy generation, emits greenhouse gases into the atmosphere. A comprehensive view of global greenhouse gas emissions is shown in Fig. 1-1, which describes the sources and activities across the global economy that produce greenhouse gas emissions, as well as the type and volume of gases associated with each activity [1].

The data in Fig. 1-1 show that transport sector accounts for 15.9% of the total world greenhouse gas emissions, 75% of which come from road transportation. As part of this, the EU has set a target of reducing transport emissions by 60% by 2050 compared to 1990 levels [2]. In addition, the UK has aims to reduce greenhouse gas production to zero by 2050 based on a new government plan to combat climate change [3]. Greenhouse gas emissions from road vehicles can be reduced in two ways: by improving the efficiency of vehicles or by changing the fuel used. Therefore, the emergence of hybrid electric vehicles (HEVs) and electric vehicles (EVs) are promising solutions for decreasing or substituting dependence on fossil fuels and reducing emissions for road transportation [4]. Electric machines (EMs) convert electrical energy into mechanical energy (and vice versa) are key components responsible for optimizing the performance features of HEVs and EVs. In comparison with other applications, automotive traction motors require a high-specific-power density to reduce fuel consumption and extend the traveling range. In addition, such motors also require a small size and low cost. The performance targets set for electric automotive traction motors by the U.S. Department of Energy (DOE) [4] and U.K. Advanced Propulsion Centre (APC) [5] are shown in Table 1-1. The targets illustrate how

developments in electric machines will broadly focus on achieving a significant increase in performance on the one hand and reducing cost on the other [5].

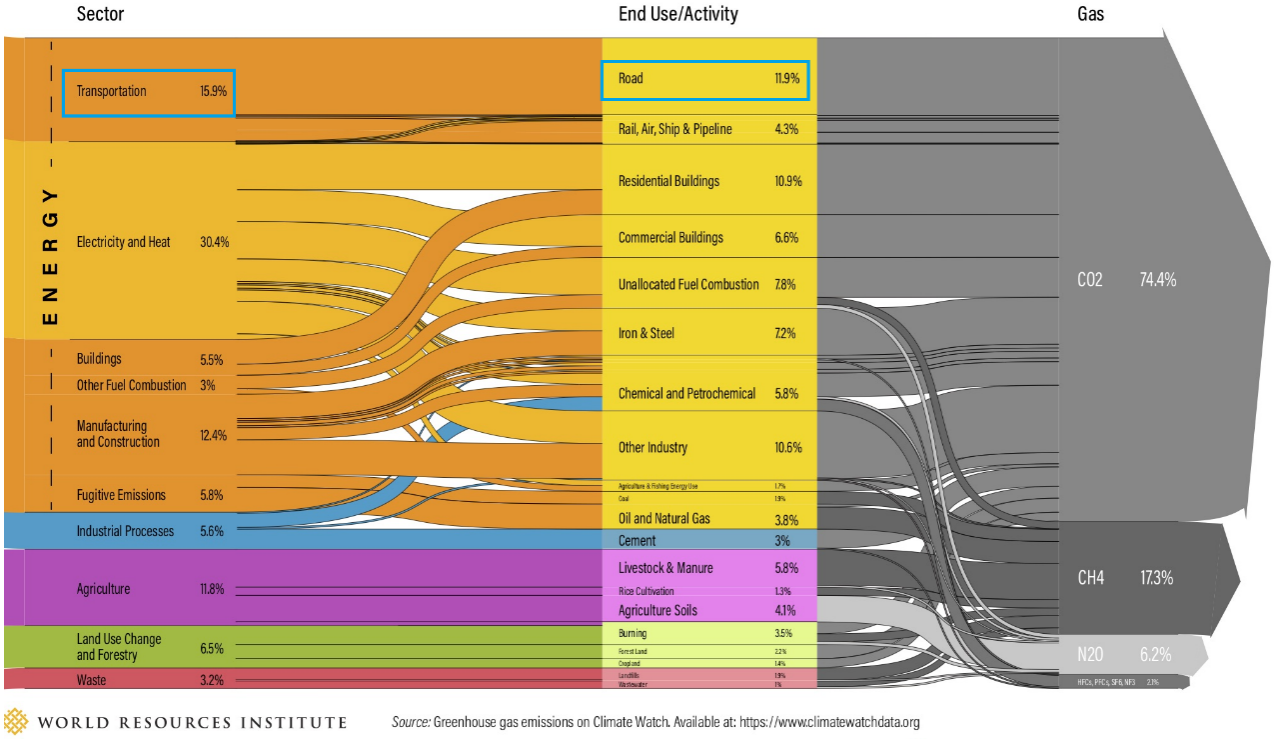

Fig. 1-1. The world greenhouse gas emissions in 2016 (Sector|End Use|Gas) [1].

Table 1-1. Technical targets for electric traction motor.

Year	2017	2020	2025	2035	Reference
Peak Power Density (kW/L)		5.7	50		U.S. Department of Energy (DOE)
Cost ($/kW)		4.7	3.3		
Continuous Power Density (kW/kg, kW/L)	2.5 / 7		7 / 25	9 / 30	U.K. Advanced Propulsion Centre (APC)
Cost ($/kW)	10		5.8	4.5	

The peak power rating targets in Table 1-1 is only expressed for short term operation: the motor overheats if the operating time is too long. The enhancement of peak specific power can be achieved by increasing electric loading, magnetic loading, rotor speed, and design quality [6]. Furthermore, continuous power density targets published by the U.K. APC are more important than peak power because it is a fairer representation of real-life operation compared to the transient peak figure. The continuous power output

is directly associated with the heat-removal capability of critical components within the limits of electrical operation. Thus, thermal constraints impose significant limitations on the final performance of electric motors. Furthermore, effective thermal management will give better electromagnetic performance and longer life expectancy. Firstly, excessively high temperatures can cause accelerated insulation aging [7] and deterioration within some essential components, such as winding conductors [8]. Secondly, the remanence and coercivity of the rare earth magnets are inversely proportional to the temperature. As a result of which, partial or full demagnetization at higher temperatures may occur [9, 10]. In addition, the electrical resistivity of the winding conductors rises in direct proportion to the temperature. This process can lead to a positive feedback in which an accelerated loss and temperature rises occur in the windings [11]. Finally, the thermal impact on the geometrical dimensions of the motor's physical structure, such as a narrowing within the airgap, may alter the motor's nominal performance, or, in serious cases, result in faults and failures [12]. To tackle the thermal challenges in an electric motor, alongside the minimization of the magnetic losses as sources of heat, one needs to carefully address the heat dissipation mechanisms for a given design in order to obtain a balanced heat distribution across different components.

The heat-removal capability of an electric machine depends not only on the passive stack thermal resistance within the machine, but also on the active convective cooling performance of the chosen cooling technology. Passive thermal design refers to the geometric layout, material selection, and thermal interfaces that affect the heat dissipation capacity within the machine, thereby determining the thermal temperature gradient of the machine. Active convective cooling technology is another component that significantly affects the thermal management performance of machines, which is also a cooling mechanism that can ultimately remove heat from the machine and transfer it to the surrounding environment. In order to minimise heating within the motor, a highly effective cooling and ventilating system has to be incorporated into the optimal design of such motors. It can ensure sufficient heat removal from the machine inside.

There are several ways to cool automotive traction motors. Forced air cooling, along with the cooling fins integrated in the housing, is employed in the Tesla Roadster [13]. In such a motor, the internal and external air flows are improved to extract the heat

most effectively. Air cooling is a robust process, which is easily integrated, maintained and operated. However, for some applications, the power-to-dimension ratio of the motor has to be greater, with a higher efficiency and lower noise level. The requisite outputs cannot be attained by air cooling, and a liquid cooling system is often applied. Used a housing water jacket is the most common liquid cooling approach. This is employed in the Toyota Prius [14], the Sonata [15], the Nissan Leaf [16] and the BMW i3 [17]. The main drawback with the housing water jacket cooling system is that the inner rotor is far away from the coolant. This leads to a poor heat dissipation condition within the rotor and causes a serious over-heating problem. In order to overcome this drawback, an extra rotor cooling system is then used in such later-developed vehicles as the Tesla S60 [18]. It is noted that the hybrid cooling schemes are more effective whilst any suitability for the mass production remains a challenge due to the manufacturing complexity.

A proper understanding of the cooling performance in an electric motor is a prerequisite of an accurate and efficient thermal design. The common approaches include the analytical lumped-circuit [19, 20] and numerical methods [21]. The merit of the analytical approach lies in the fact that the network parameters can completely describe the thermal performances of a machine's steady and transient states respectively [22] and can be computed with ease. However, some of the parameters in this model are very complex. Such models even do not exist in the literature. On the other hand, the numerical approaches based on time step Finite Element Method (FEM) and Computational Fluid Dynamics (CFD) are commonly applied to such complicated models. The FEA is a highly accurate tool for modelling the temperature distribution in complex solid parts [23]. In cases where cooling occurs by connecting two different mediums, only CFD can be effective in predicting the coolant heat transfer coefficient (HTC) at the boundaries [24] through the complex shape area. CFD is based on the finite volume technology with the aim of simulating 3-D laminar or turbulent flow with a high degree of accuracy. Reynolds Averaged Navier-Stokes (RANS) equations are mostly used to deal with the 3-D turbulent flow and heat transfer of cooling systems. Six Reynolds stresses need to be calculated in order to close the RANS equations. A common method is to use the eddy viscosity model via the Boussinesq hypothesis which relates to the Reynolds stresses as a function of turbulent viscosity. In order to

calculate turbulent viscosity, various turbulent models are employed to solve one or more transported quantities: for example, in case of the modified turbulent viscosity (Spalart-Allmaras model); the turbulent kinetic energy k and turbulent dissipation rate ε (k-ε model); the specific dissipation rate ω (k-ω model). In addition, the Reynolds stress transport (RST) model known as a second class model is based on a direct calculation of the stress-tensor components, requiring 5 additional transport equations. After that, CFD helps to provide inputs into the FEA and analytical lumped-circuit models. However, the model setup and computations can be highly time-consuming, especially when 3D modelling is necessary.

1.2 Thesis Objectives

Designing a high-power density, low-cost electric motor is critical to improving the overall performance of HEVs and EVs. However, the variance between the maximum power output and the continuous power output of these motors, indicates the current performance has not reached the limits of electromagnetic design. Consequently, an optimized thermal design of automotive traction motors not only substantially increases the rated power of machine, but also achieves excellent reliability and a long service life. Generally speaking, a thermal design uses a closed or an open cooling circuit to achieve a critical temperature balance within an electric motor. Heat from the inner components is conducted to the outer surface of the motor and then is subjected to convective cooling. However, having an internal rotor is usually associated with a poor heat transfer due to the airgap acting as an insulating material. As a consequence of such a difficulty to dissipate the heat, the increased temperature in the rotor may result in partially irreversible demagnetization particularly for permanent magnet machines. On top of this, a better cooling performance of the rotor will result in higher power density, better field weakening capability and reduced costs.

The main objective of this thesis is to produce a rotor cooling system for automotive traction motors which demand a small package as well as high torque and high power density. In the proposed rotor cooling system, the coolant is made to flow through a hole in the shaft. It has been found that the heat transfer of the rotating flow is rather different from that observed in a nonrotating flow. In the literature hitherto, only low rotation speeds have been looked at. Moreover, until now all coolants have been air /

water-based. In reality, most coolants used in the automotive traction motors are oil-based. This means that there is still work to be done in relation to the effects of high rotational speeds on heat exchange. On this basis, the evaluation of the effect of high rotational speeds on heat exchange in oil-based rotor cooling is another main objective of this thesis. In addition, the detailed research activities conducted in this project, are as follows:

- Investigate the state of art of the cooling methods for automotive traction applications;
- Design a hollow-shaft rotor cooling system for automotive traction motors;
- Evaluate the thermal performance of hollow-shaft rotor cooling method;
- Estimate the influent parameters on this cooling system, such as the rotational velocities, coolant flow rates and amount of heat losses;
- Non-dimensionalise the HTC results into an equation using various dimensionless groups;
- Analyse the effects of rotation on the pressure losses for hollow-shaft cooling system.

1.3 Thesis Structure

The thesis is structured as follows:

Chapter 2: Literature Review: describes various convective cooling methods, including the natural, forced air, forced liquid and phase change types. The essential elements for optimizing the cooling performance of each method together with the leading applications are specifically highlighted. In addition, the latest automotive traction motor prototypes and products employing these methods, have been set out and evaluated. Finally, the use of the analytical lumped-circuit and the computational fluid dynamics techniques for calculating the cooling performance are proposed and discussed.

Chapter 3: CFD Modelling of the Heat Transfer Coefficient for a Low Speed Water-Cooled Hollow-Shaft Rotor Cooling System: provides a detailed description of the numerical thermal modelling of a water-cooled hollow-shaft rotor cooling system

and its critical regions; this includes the description of the flow and solid domains, meshing approach, governing equations, turbulent models, boundary conditions and wall treatment setup, moving reference frames, and convective heat transfer calculation.

Chapter 4: Experimental Investigation of a Low Speed Water-Cooled Hollow-Shaft : following the modelling undertaken in Chapter 3, the experiments are used to validate the accuracy of CFD models with the assistance of an analytical LPTN approach. The effects of rotation on heat exchange of the turbulent flow are discussed based on the CFD simulations and the experimental prototype testing.

Chapter 5: Thermal Analysis of a High Speed Oil-Cooled Hollow-Shaft: investigates the effects of high rotational speeds on heat exchange of the laminar flow. On this basis, an oil-based hollow-shaft rotor cooling system is conducted. The various losses, which consist of iron, air friction and bearing losses are identified across a range of operation speeds. Then a finite element model is constructed to represent the heat path taken in the test shaft.

Chapter 6: Experimental Investigation of a High Speed Oil-Cooled Hollow-Shaft Rotor Cooling System: describes the experimental mechanisms, measurement techniques and calibrations using uncertainty analysis. Experiments are then carried out to evaluate the impact parameters of this cooling method.

Chapter 7: Study of Pressure Loss in a Hollow-Shaft Cooling System: determines the effects of rotation on the pressure drop for turbulent and laminar flows. CFD is used to calculate the pressure losses by taking the rotational effect into account. On this basis, the coolant streamline gives a visualization of the flow patterns under the effects of rotation. Then the trend of the pressure losses along the shaft at various rotation rates is explained in detail.

1.4 Contribution to Knowledge

This thesis contributes to knowledge in the following areas:

- A comprehensive overview of the latest studies and analyses of the cooling technologies and computation methods for the automotive traction motors (Chapter 2);

- A detailed description of the numerical thermal modelling of the HTC in a liquid cooled hollow-shaft rotor (Chapter 3);
- Performance comparison of three turbulence models for the prediction of the HTC (Chapter 3 and 4);
- The effects of rotation on HTC for the turbulent and laminar flows (Chapter 4 and 5);
- The impact factors such as coolant flow rate, coolant temperature and the amount of heat loss, on the thermal performance of the hollow-shaft rotor cooling system (Chapter 5 and 6);
- The pressure losses distribution across various distances from the shaft entrance, along with a number of different flow patterns (Chapter 7).

1.5 Published Work

- Y. Gai, M. Kimiabeigi, J. Widmer, Y. Chong, J. Goss, D. Staton, et al., "Shaft cooling and the influence on the electromagnetic performance of traction motors," *in 2017 IEEE International Electric Machines and Drives Conference (IEMDC)*, 2017, pp. 1-6.

- Y. Gai, M. Kimiabeigi, Y. Chong, J. Widmer, J. Goss, A. Steven, D. Staton, et al., "Modelling the Friction Loss in a Hollow-Shaft Water-Cooled Rotor of Traction Motors," *in 2018 XXIIIth International Conference on Electrical Machines (ICEM),* 2018, pp. 1297-1302.

- Y. Gai, M. Kimiabeigi, Y. Chong, J. Widmer, J. Goss, A. Steven, D. Staton, et al., "On the Measurement and Modelling of the Heat Transfer Coefficient of a Hollow-Shaft Rotary Cooling System for a Traction Motor," *IEEE Transactions on Industry Application*, vol. 54, pp. 5978-5987, 2018.

- Y. Gai, M. Kimiabeigi, Y. Chong, J. Widmer, X. Deng, M. Popescu, J. Goss, D. Staton, et al., "Cooling of Automotive Traction Motors: Schemes, Examples and Computation Methods," *IEEE Transactions on Industrial Electronics*, vol. 66, pp. 1681-1692, 2019.

- Y. Gai, Y. Chong, J. Goss, M. Popescu, " Power Loss and Thermal Analysis of a Hollow-Shaft Rotor Cooling System," submitted at *2019 22nd International Conference on Electrical Machines and systems (ICEMS)*, 2019, pp. 1-6.
- Y. Gai, J. Widmer, A. Steven, Y. Chong, M. Kimiabeigi, J. Goss, M. Popescu, " Numerical and Experimental Calculation of CHTC in an Oil-Based Shaft Cooling System for a High Speed High Power PMSM," *IEEE Transactions on Industrial Electronics*, vol. 67, pp. 4371-4380, 2020.

2 Literature Review

While operating an electric motor, heat is generated due to the electromagnetic losses, mechanical power losses and other stray losses that take place in various components within an electric motor. Through conduction, convection and/or radiation, the thermal energy is transferred to a cooling medium [18] on the basis of a temperature difference between the hot and cold bodies. However, a detailed thermal management is essential during critical operating conditions, such as overload running, phase changing and/or asymmetric faults, to avoid failures that are usually due to the local hot spot formation, and material degradation [25-28].

The thermal management of an electric machine includes the design of passive heat transfer path within machines and active convective cooling system. The passive thermal design is affected by material properties, geometrical layout and contact interfaces. This process is considered economical and does not produce any additional parasitic effects such as acoustic noise. The active cooling design is in which an extra source of energy is applied to circulate a fluid with a high heat capacity in order to exchange and extract the heat from the hot surfaces [29]. This active method of cooling applies an external force created by a special device, e.g. pumps, fans to generate sufficient coolant flow to remove heat from the interior parts of a motor. This approach provides a high convection heat transfer capacity but the extra provisions are required for diminishing not only friction losses, but also risks of short circuit faults and corrosion [30]. Table 2-1 lists values of heat transfer coefficients only to give the reader an idea of what a reasonable value might be for the condition listed. A diversification of cooling approaches have been pursued to meet the cooling demands placed on various applications. However, the rapid growth of aerospace and traction industries have brought about increased requirements for electric motors such as compactness, high speed and high power density. This leads to significant rises in temperature in cases where miniaturized motors are involved, thus necessitating a more sophisticated and complicated cooling system to keep the working temperature within a safe range [31, 32]. In this chapter, a detailed analysis of the active type cooling: the natural, forced air, forced liquid and phase change types, are reviewed.

Table 2-1. The typical values for different cooling methods [33-35].

Cooling method		σ, kPa	A_l, kA/m	J, A/mm^2	h, W/(m^{2}K)
Natural convection		-	-	1.5-5	5-30
Forced gas cooled	Air	<15	<80	5-10	20-300
	Hydrogen	<25	70-110	7-12	100–1000
Forced liquid cooled	Indirect	20-60	90-130	7-20	100-10000
	Direct	60-100	100-200	10-30	200-25000
	Phase change	-	-	-	500–50000

2.1 Natural Passive Cooling

Natural convective cooling uses the on-site energy, combined with the configuration of motor components to dissipate heat. The housing is main path to remove the heat from inner components to ambient. The design of the housing need to be optimized in order to maximize the rate of convective heat dissipation.

In practice, correlations of convective heat transfer h that have been developed for natural cooling to show that Nusselt number Nu mainly depends on Grashof number Gr and Prandtl number Pr [36], defined as the following equations :

$$Nu = h \cdot L/\lambda \tag{2-1}$$

$$Nu_{Natural} = f(Gr, Pr) \tag{2-2}$$

$$Gr = \frac{g\beta\rho^2(T_{wall} - T_{fluid})L^3}{\mu^2} \tag{2-3}$$

$$Pr = \mu \cdot c_p/\lambda \tag{2-4}$$

where L is the characteristic length of the surface; λ is the thermal conductivity; β is the coefficient of the cubical expansion; g is the gravitational acceleration; ρ is the density; T_{wall}, T_{fluid} are the wall and fluid temperatures respectively; μ is the dynamic viscosity; and c_p is the specific heat capacity.

A suitably designed finned housing can improve the heat transfer coefficient value compared to a non-finned housing. The cooling fins are normally placed on the surface of the housing, and are oriented in such a way that do not disturb the natural airflow. There are two types of fins with regards to the direction relative to the motor shaft, one being the radial fin array [37], the other an axial fin array [38].

The heat transfer rate from fins to the ambient may rise either by increasing the heat transfer coefficient and/or fin surface area. However, the natural convection heat transfer coefficient depends on the temperature difference between ambient and fin surface. A common practice to improve the natural convection heat transfer is to extend the fin area; however, this increases the resistance of the air flow which in turn diminishes the gain factor. The optimization of the fin extension (H), fin pith (S) and the fin thickness (t) which are illustrated in Fig. 2-1, is the main approach to increase the natural cooling performance [39-44]. The key design objective must be to maximize the rate of the heat dissipation, whereas minimizing the weight and volume of the cooling fins, based on which the correlation in (2-2) can be rewritten as (2-5) with the fin geometrical parameters involved.

$$Nu_{Natural} = f(Gr, Pr, f(H, S, t)) \tag{2-5}$$

The natural cooling approach, however, is appropriate only for low or medium-power motors or large electric motors with sufficient heat transfer areas.

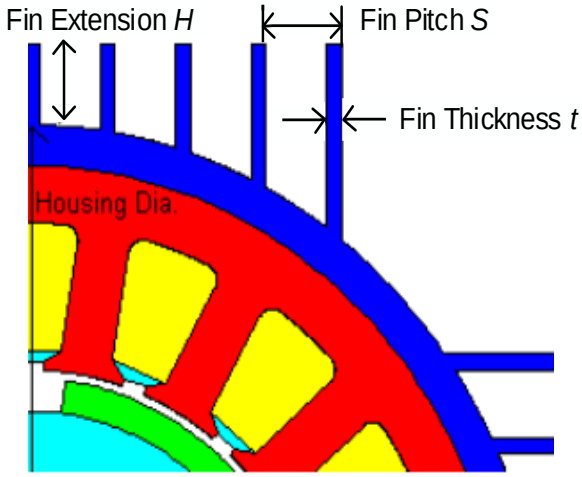

Fig. 2-1. Fin configuration geometry.

2.2 Forced Cooling

Forced cooling is a more popular approach than the passive type discussed in Section 2.1, as more power dense and compact motors are being introduced to the market. As compared to the natural cooling, the forced cooling uses an external device and source of power to create sufficient coolant flow to exchange and extract the heat from the hotter components. The Reynolds Number Re is used to determine the flow patterns,

so-called flow regimes, under different cooling media and architectures, and can be analytically estimated by (2-6).The heat transfer based on the forced convection method can be defined as a function of Re and Pr in accordance with (2-7) [36],

$$Re = \frac{\rho DV}{\mu} \tag{2-6}$$

$$Nu_{Forced} = f(Re, Pr) \tag{2-7}$$

where D is the hydraulic diameter; V is the axial velocity.

2.2.1 Forced Air

In a forced air cooling system, a fan or a blower is employed to generate the continual passage of air through a motor or over its exterior. Depending on the enclosure of a motor, forced air can be divided into two different varieties: an enclosed fan cooled (EFC) motor and an open fan cooled (OFC) motor.

An EFC motor consists of an inner and an outer flow circuit. These are displayed in Fig. 2-2 [45, 46]. The recirculating air from the inner circuit brings heat from the inner motor to the housing frame, where an outer flow circuit functions as a heat sink. The EFC configuration prevents a free exchange of air between the inside and the outside of the motor. An internal fan, either integral to the rotor or mounted on the shaft, circulates air inside the enclosure which promotes the heat transfer to the frame. An exterior fan, makes the surrounding air pass over the housing, thus removing heat to the ambient environment. However, the efficiency of a shaft-mounted fan is limited by the speed of shaft. Hence an external fan or blower is employed to generate the optimal level of air pressure independently of the shaft speed. For an EFC approach, the recirculated air is often cooled via the ambient air through the external frames in case of the small motors or by an air-to-water heat exchanger in case of the large motors. The key benefit of the EFC scheme is that the interior parts are better protected against pollutants which may block the ventilation ducts, with the risk of impeding the airflow. Furthermore, the cooling performance can be improved by replacing the air with a suitable gas that has higher heat conduction and higher specific heat capacity than air, e.g. hydrogen [47]. This is owing to the fact that the smaller and lighter gas molecules can result in a lower windage loss and better heat transfer than air.

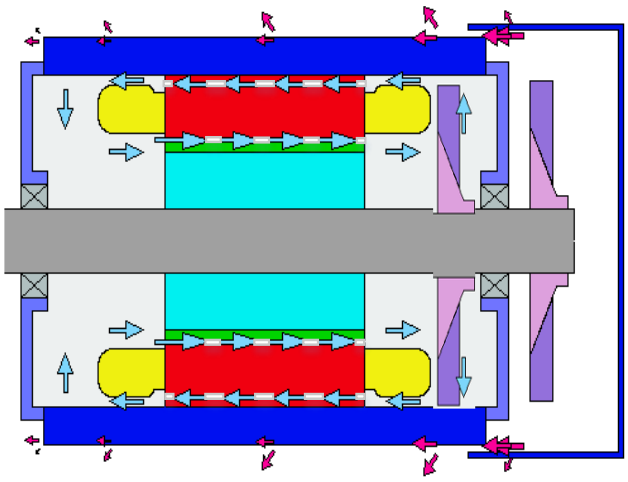

Fig. 2-2. The ventilation structure of an EFC motor.

An OFC motor ventilation structure is illustrated in Fig. 2-3. The coolant air is continuously drawn from the ambient environment into the motor enclosure, and not re-circulated. Since, in this method, the motor is exposed to the environmental contaminants, provisions such as using filtering or employing indirect air channels need to be in place to prevent particles or moisture from entering the motor [48]. Because of the accumulated pollutants, OFC motors are regularly dismantled for a clean-up operation once every two or three years [49].

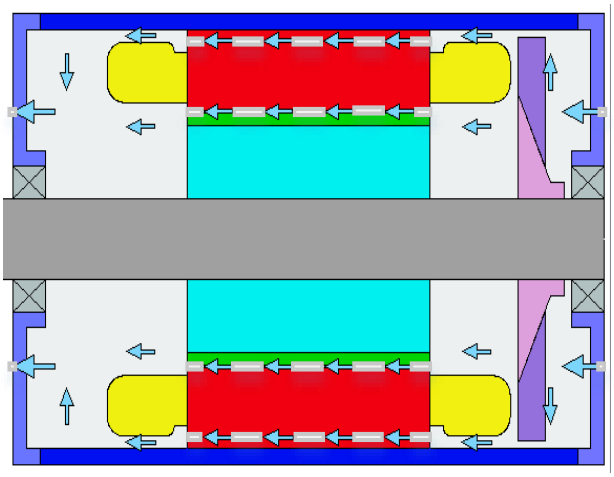

Fig. 2-3. The ventilation structure of an OFC motor.

The cooling performance of the forced air motors strongly depends on how large the surface contact areas is between the coolant and the motor components. This can be improved by adding geometrical modification such as cutting multiple air slots into the shaft, rotor, or the stator core [50].

In a fan based cooling system, the fan provides a differential pressure to make the coolant air flow. Fig. 2-4 shows the relationship between the fan characteristic and the motor enclosure system resistance curve, as well as the operating pressure and flow rate at the intersection point. The bending of the fan characteristic curve is due to the energy losses, and can be improved by optimizing the aerodynamic structure of the blades. A new kind of axial fan with forward-swept and inclined blades is employed in [51-53] to reduce the ventilation resistance inside an electric motor, as is illustrated in Fig. 2-5. Further enhancement in cooling can be achieved by various retrofit methods, such as adding internal air baffles to an EFC motor [54], or by interrupting any combination of flows from occurring especially at high rotor speed [55], as is shown in Fig. 2-6, where the flow guard is used to prevent the outflow from rotor ducts interfering with the outflow from annular gap.

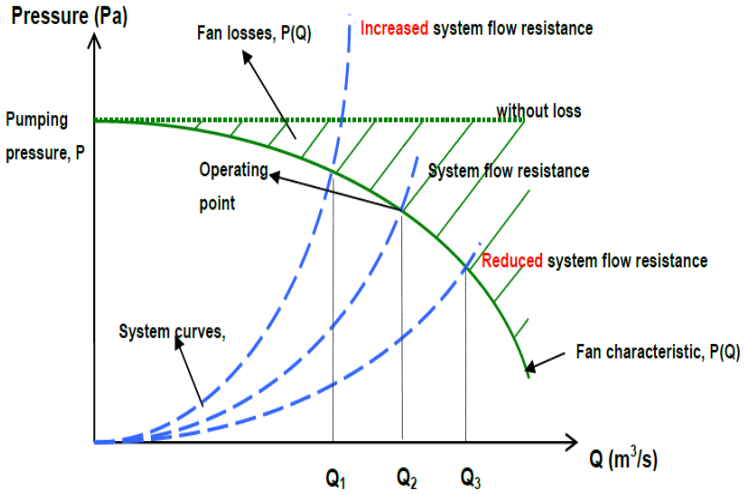

Fig. 2-4. A typical fan characteristic curve [55].

Fig. 2-5. The axial fan with forward swept and inclined blades [53].

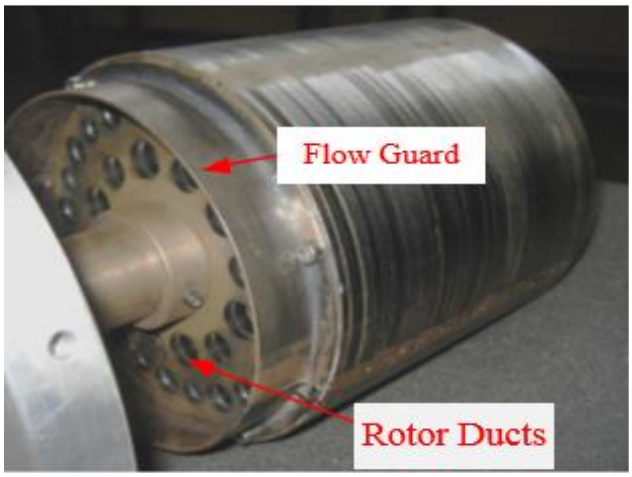

Fig. 2-6. Arrangement of flow guard [55].

One of the major challenges associated with fan cooling is the emission of acoustic noise, especially at a high speed fan operation. Several noise mitigation methods have been proposed by the literature:

- using forward-swept inclined fans [51, 52];
- using a better aero-foil shape blade cross-section [56];
- using inlet bell-mouth entry [57];
- using composite materials for blades [57];
- reducing the number of blades [56, 57];
- using irregular-pitch-blade fan [45, 57, 58];
- using a mixed flow (both axial and radial) fan [56].

2.2.2 Forced Liquid

A forced liquid cooling solution is suitable in particular applications, especially for high-power electric motors, where the requisite outputs cannot be attained by EFC or OFC motors. Forced liquid cooling approaches such as those that are designed for electric motors are presented in Fig. 2-7. In such a cooling system, the forced liquid passes through the housing jacket, stator channels and/or rotor channels. However, the forced liquid cooling system suffers from a number of weaknesses, such as stains, corrosion, leakage and contamination. The remaining stains inside of cooling channels may lead to a significant rise in flow resistance, which causes a decrease in the cooling effectiveness. The most common liquid coolant in thermal management of electric motors is water. The reason why water is chosen is primarily due to the high relative

heat capacity of this liquid. In addition, a number of components are available for commercial applications, such as ethylene glycol and water (EGW) 50/50 and engine oil.

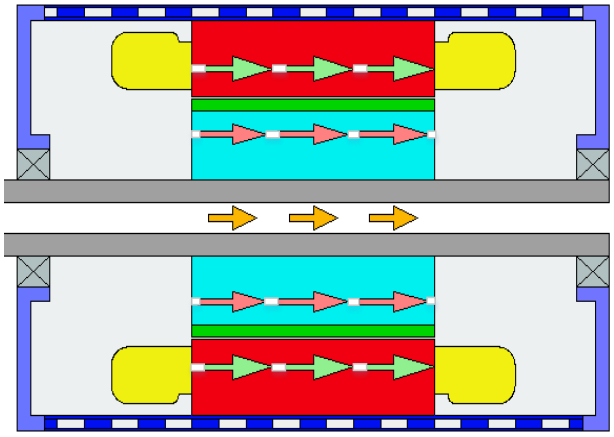

Fig. 2-7. The forced liquid cooling models.

2.2.2.1 Housing Water Jacket

The cooling via a housing jacket is the most common forced cooling approach. This is where the liquid flows through the cooling channels situated in a thermally conductive frame above the stator stack [32, 59-61]. The heat generated in the coils, as well as in the stator and rotor laminations, is initially transferred to the cooling housing through conduction, and is, then transferred to the ambient environment via convection in the coolant fluid. The efficiency of the liquid cooling technique heavily depends on the geometrical clearance and the resultant thermal resistance between the laminated stator core and the cooling housing.

The effects of different parameters on the contact thermal resistance between the laminated stator core and the frame, such as shrink fit pressure, thermal paste use etc., were experimentally investigated in [62]. A ferrite magnet motor design, [63], is used to verify the effect of the contact interfaces on the stator winding and magnet temperature. The results at 10000 rpm/55.5 kW, as is shown in Fig. 2-8, are based on an analytical method using Motor-CAD and these indicate that a poor contact between the stator and frame encourages an increase in the temperature of the winding and the magnet, with the maximum possible increase being about 40 ˚C. An alternative to water in a liquid cooling system, includes Shell Tellus oil premium 22 [64], and Statoil

transmission oil [65], which are provided from the lubricating oil already applied to the gearbox system.

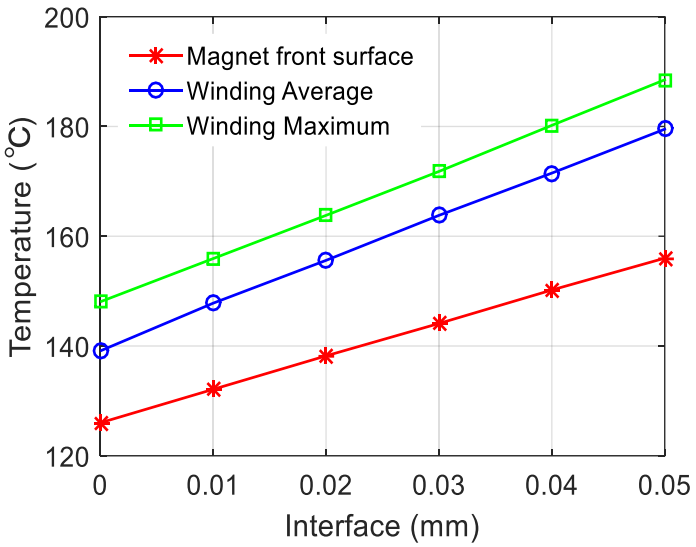

Fig. 2-8. Sensitivity analysis of the stator and housing contact interfaces on components temperature.

Whilst a housing jacket provides a sufficient heat transfer for the active part of the stator winding, it is, usually, inadequate to dissipate the heat from the end winding and rotor due to the high thermal resistance between the heat source and the coolant. This can be particularly problematic for motors with long end windings, such as distributed wound motors with few pole numbers.

2.2.2.2 Stator Cooling

A further method of liquid cooling is via cooling slots cut directly into the stator laminations. These are located in the stator yoke [66-70] or the winding slots [71-73]. Even if the coolant gets closer to the windings and the laminations, resulting in a smaller thermal resistance, care must be taken to prevent the cooling slots from disturbing the magnetic flux in the stator core [74, 75]. In [66], the effects of an evenly spaced number of different water slots on the average temperatures of winding (T1), winding epoxy (T2), slot insulation (T3), iron core mover (T4), have been shown in Fig. 2-9. These effects are based on finite element (FE) simulations to demonstrate the effectiveness of the approach for this water-cooled permanent magnet linear motor. It is worth noting that the maximum number of water pipe slots should be chosen as a tradeoff between the ease of manufacture and the required temperature rise limitations.

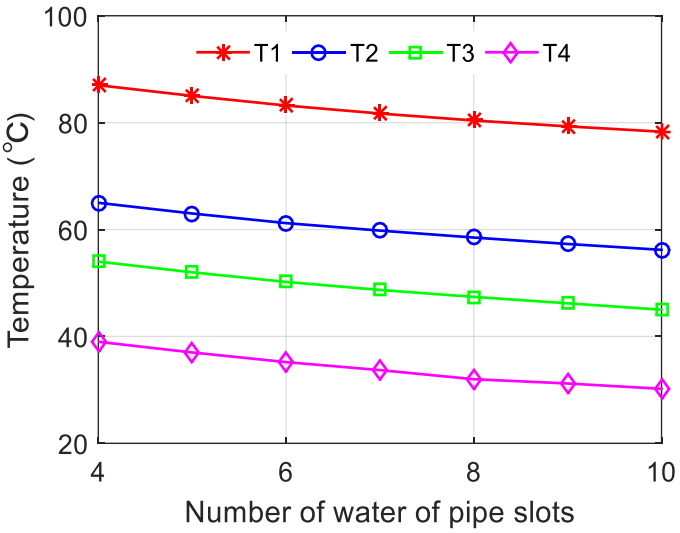

Fig. 2-9. Stator winding maximum temperature at various flow speeds with different water slots based on FE simulations [66].

Using a wet stator is a less commonly employed way of stator cooling. In this less common method, a fluid with a high heat transfer coefficient, such as hydraulic oil [76], is made to pass through the armature end windings and the stator laminations. A sleeve is introduced to prevent the liquid from entering the air gap in order to avoid windage loss, as illustrated in Fig. 2-10. This cooling approach provides the minimum thermal resistance between the coolant and the heat source, providing the best heat transfer capability [77].

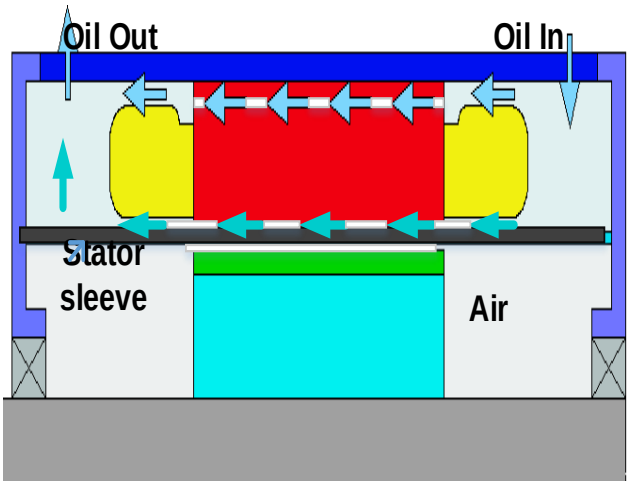

Fig. 2-10. Wet stator cooling system.

2.2.2.3 Rotor Cooling

Having an internal rotor is usually associated with a poor heat transfer due to the airgap acting as an insulating material. Poor heat transfer leads to a loss of electromagnetic performance. To enhance the heat transfer, the enclosed air can be replaced by a high density thermal conductivity medium, i.e. water or oil [76]. After that, the motor is totally flooded and the rotor and stator surfaces are directly flushed by a coolant. However, a direct liquid cooling method is not an economical and practical one. This is due to the extra provisions required for diminishing not only the friction losses, but also risks of short circuit faults and corrosion [76]. Reference [78] introduces an annular gap between the winding and the airgap for slotless motors. This is where the coolant is brought closer to the rotor. As a rotary part, the direct liquid cooling apparatus of a rotor is difficult to manufacture. As a results, a hollow shaft cooling system [21, 79-83]as an indirect way of dissipating heat can be employed. Fig. 2-11 presents a shaft cooling system, where the coolant is introduced into the system via a coupling connected to a stationary inner tube and is driven back to the gap between the injection tube and the hollow shaft [31].

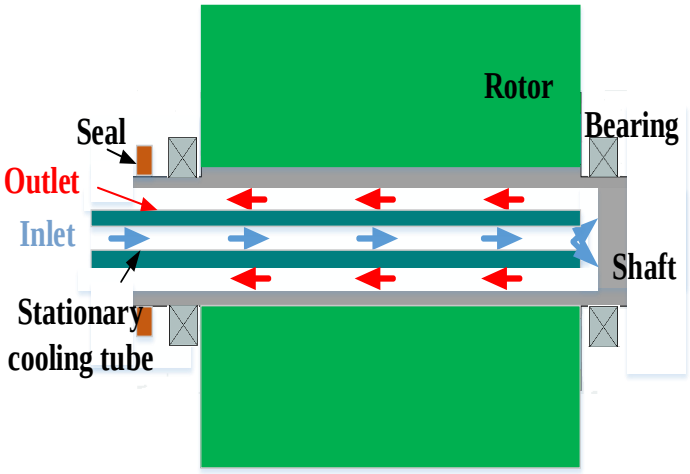

Fig. 2-11. Indirect rotor cooling scheme.

The heat transfer characteristics of the rotor cooling system are complex. A secondary flow will occur as a result of the rotation while the cold and dense fluid in the center tends to move radially to the wall due to the Centrifugal and Coriolis Effect. Consequently, the convection heat transfer coefficient correlations of a stationary case is invalid for rotor cooling [84] and the rotational Reynold number Re_r must be introduced to estimate the effect of the rotation. The typical form of the convection

correlation for rotating flow is defined as (2-8) (2-9) [84]. Reference [21, 84] have experimentally and theoretically demonstrated that the rotational speed can significantly increase the convective heat transfer in the rotor cooling above the stationary condition.

$$Nu = f(Pr, Re, Re_r) \tag{2-8}$$

$$Re_r = 0.5 * \rho D V_r / \mu \tag{2-9}$$

where V_r is the tangential velocity.

2.2.2.4 Phase Change

In a phase change cooling system, a coolant is applied in such a way that at least a portion of the coolant is transformed into vapour upon heating. The principle of a phase change loop is illustrated in Fig. 2-12. A refrigerant is pumped into the heat source as an evaporator, at which point, after absorbing the thermal energy, is transformed into a gaseous state. The heated gas is then recycled back into the compressor, releasing thermal energy. The refrigerant at the liquid state is pumped back again as a new cycle begins. Phase change cooling systems provide high heat dissipation rates at higher operation temperatures with a considerably smaller working volume than a single phase [85]. The simplest phase change cooling scheme is a heat pipe. It is a closed pipe filled with a dedicated working fluid. In manufacturing terms, heat pipes can easily be installed in electric motors. However, the heat transfer capability of a heat pipe depends on the dimensions and the temperature drop between the two ends [34].

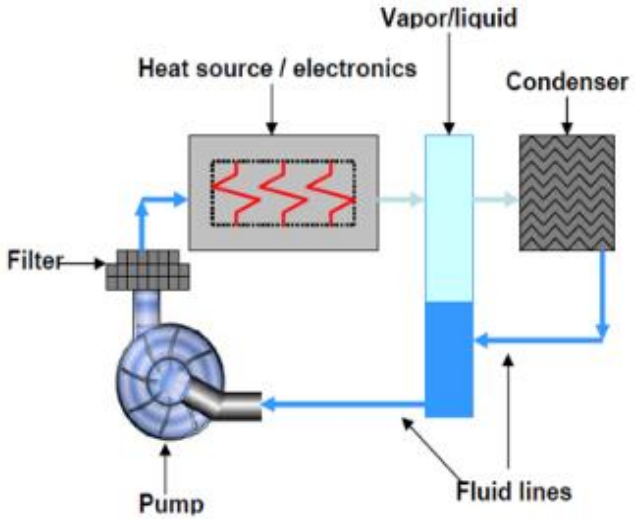

Fig. 2-12. Primary components of a phase change cooling loop.

Spray cooling [86-88] is another cooling technique which involves a phase change. Spray cooling of the stator and rotor end turns is depicted in Fig. 2-13. A cooler liquid is sprayed onto the end-windings and/or rotor via nozzles. After moving over various surfaces on the inside of the motor, the coolant is partially evaporated into a gaseous state (phase change), which is condensed back into liquid in the condenser and drained out into the reservoir along with the unevaporated coolant. Spray cooling can be used to transfer large amounts of energy through the latent heat of evaporation and create uniform temperatures without reducing magnetic field fluctuations or creating electric noise. Despite these advantages, spray cooling is considered excessively complex insofar as it requires nozzles with high pressure [89]. The submerged double jet impingement method [90] and experimental approach [29] are used for calculating the heat transfer coefficients of the spray cooling.

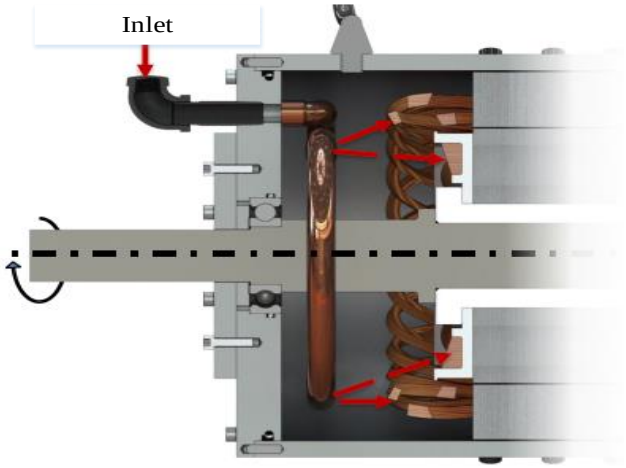

Fig. 2-13. A spray cooling on the stator and rotor end windings [91].

2.2.2.5 Hybrid Approach

In most cases, an electric motor can work reliably under conditions of substantial overloading by applying a single method of cooling. However, for the high power density applications, such as traction motors, a single cooling method may not be sufficient. On this basis, a combined forced-air and liquid cooling system have been applied in [37, 61, 67, 92]. The results relating to the rise in temperature for 30 kW traction motor compare individual and coupled cooling systems, as is shown in Fig. 2-14. It is noted that the coupled cooling schemes are more effective whilst any

suitability for the mass production remains a challenge due to the manufacturing complexity [31].

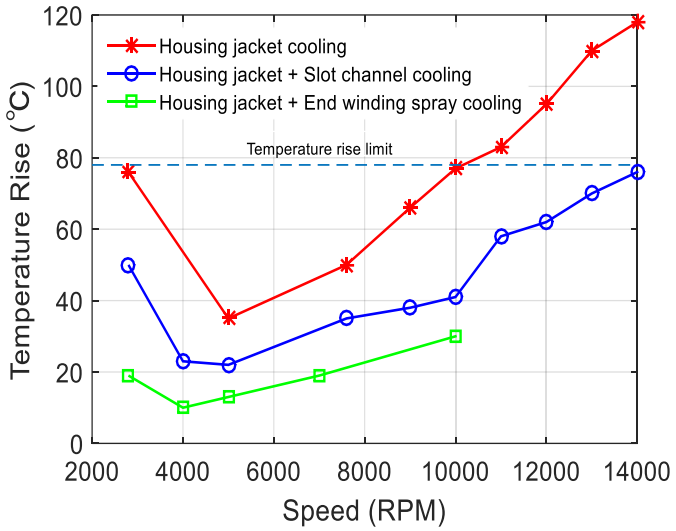

Fig. 2-14. The performance comparison for various cooling system [31].

2.3 Traction Applications

The Nissan-leaf electric motor shown in Fig. 2-15 (a) uses a water jacket for cooling an interior permanent magnet traction motor. Three cooling channels in Fig. 2-15 (b) are provided in the frame above the stator stack in parallel using EGW 50/50 as a coolant to ensure a sufficient cooling performance.

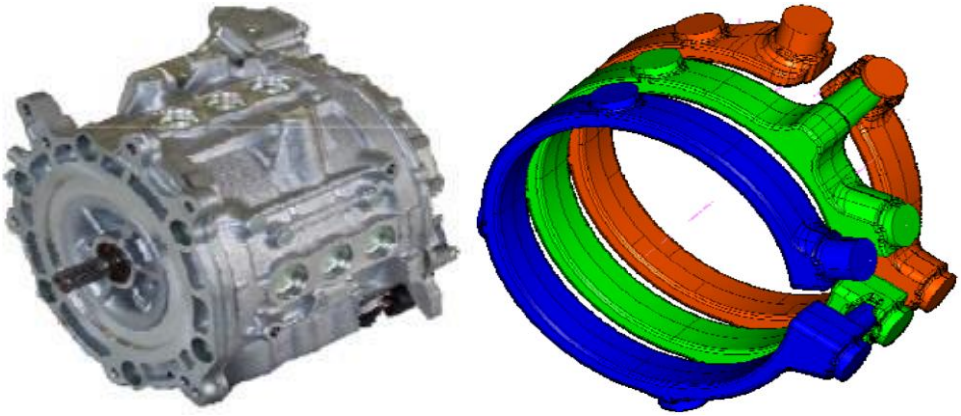

Fig. 2-15. a) Nissan-leaf electric motor b) Model of cooling water channels [18].

In Fig. 2-16 [72], a forced cooling fluid flows through the slot cooling tubes (with the option of being connected in series or parallel). The slot cooling tubes are placed inside the winding slots, adjacent to the coils.

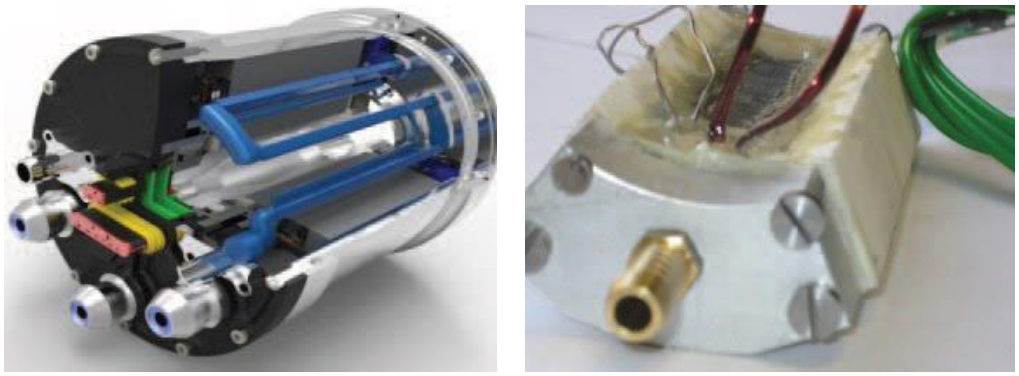

Fig. 2-16. Slot duct cooling for the whole motor (left) and single teeth prototype (right) [55].

A plurality of heat pipes are inserted in the stator slots in [60], as is displayed in Fig. 2-17 (a). All the heat pipes are extended into a cooling chamber that can be filled with oil or some other cooling fluid. Another example in [93], Fig. 2-17 (b) discloses a heat pipe that is located in the motor hollow axle, where a metallic plate as a heat exchanger is mounted at the end of the heat pipe.

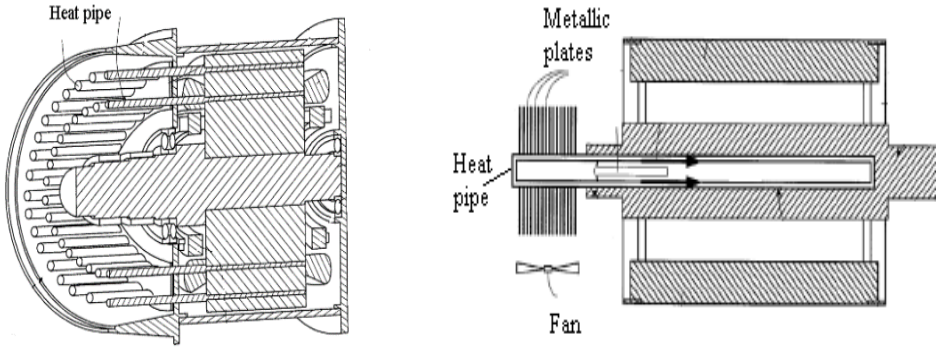

Fig. 2-17. Motor assembly with heat pipe cooling system [71, 73].

The Zytek electric traction motor [94], as is shown in Fig. 2-18, deploys a dual cooling system, a self-ventilated cooling where internal forced air flows through the rotor axial ducts, as well as the airgap of the motor, in combination with a housing water jacket. The recirculating air brings heat from the inner motor to the heat exchanger.

A list of the various cooling methods installed in the traction motors has been shown in Table 2-2, where the continuous peak power densities that can identify the performance of cooling methods are provided in detail. It is noted that the continuous peak power density depends not only on the active convective cooling method, but also on the passive thermal resistance within the machine.

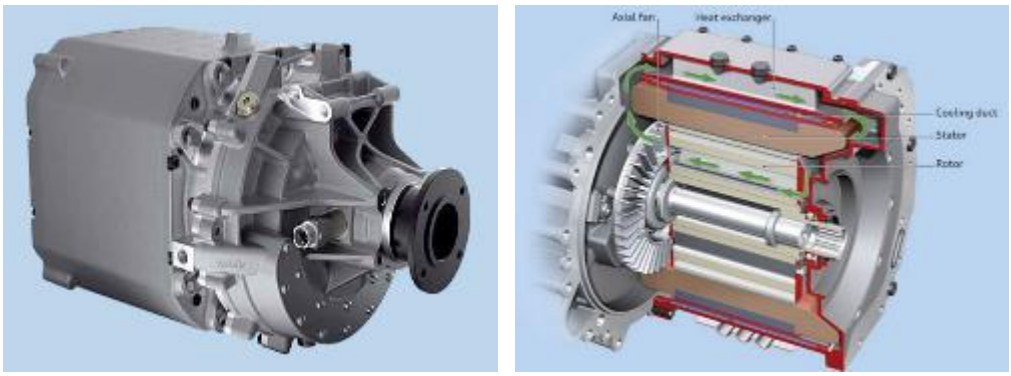

Fig. 2-18. ZYTEK high power density PMSM with dual cooling system [94].

Table 2-2. The various cooling methods applied for automotive traction motors.

Model	Peak Power (kW)	Continuous Power (kW)	Mass / Volume (kg/L)	Peak Power Density: (kW/kg, kW/L)	Continuous Peak Power Density: (kW/kg, kW/L)	Cooling methods + Reference
Lexus LS600h 2008	110	<50	45 / 16.7	2.5 / 6.6	< 1.1 / < 2.99	Housing jacket [17] [14]
Renault Zoe 2010	70	50	36 /-	1.94 / -	1.39 / -	Housing jacket [95]
Toyota Prius 2010	60	<50	36.7 / 12.5	1.6 / 4.8	< 1.36 / < 4	Housing jacket [14]
Tesla Roadster 2012	215	-	53 / -	4.05 / -	- / -	Inner forced air + Fined housing + outer fan [13]
Tesla S60 2013	225	134	76.4 / -	2.9 / -	1.75 / -	Housing jacket + Shaft cooling [96]
FreedomCAR 2014	55	30	< 35 / < 9.7	>1.5 / >5.7	> 0.9 / > 3.1	Housing jacket + End winding spray + Rotor cooling [31]
Mercedes-Benz 250e 2015	132	65	- / -	- / -	- / -	Housing jacket [97]
BMW i3 2016	125	75	42 / 13.6	3.0 / 9.2	1.79 / 5.5	Housing jacket [17, 98]
Zytek 2019	170	125	75 / -	2.3 /-	1.7 / -	Housing jacket + Forced fan cooling [94]

2.4 Computation Methods

An accurate understanding of the cooling performance in an electric motor is a prerequisite of an accurate and efficient thermal design. The key parameters to achieve this goal are the convective heat transfer, flow resistance, and fan performance in case of fan cooled systems, etc., while the common approaches include analytical lumped-circuit and numerical methods.

2.4.1 Analytical Approach

The analytical approach can be subdivided into two main calculation types: heat-transfer and flow-network analyses. Both of them are based on readily available empirical correlations in the thermal analytical literature and have the advantage of being fast. In the lumped-circuit thermal network, the convective heat transfer between the surface of the motor components and the coolant is described by convection thermal resistance defined as (2-10). The temperature of the motor components allow predictions based on the convection thermal resistances for a given power distribution. In the flow network, a drop in pressure takes place due to the flow restrictions (e.g. friction, expansion, contraction). Any loss in pressure Δp is usually quantified with an empirical loss coefficient (k_l) based upon the flow of kinetic energy, defined as (2-11). The dimensionless correlations used for calculating the convection heat transfer coefficient and the flow resistance coefficient are reported in Table 2-3 and Table 2-4 respectively.

$$R = 1/hA \tag{2-10}$$

$$\Delta p = k_l \cdot \frac{1}{2}\rho V^2 \tag{2-11}$$

The lumped-parameter models are used to present the thermal behaviour of the cooling system. The more nodes of the model, the higher accuracy results be achieved. However, the more comprehensive calculation process and more time are needed. A commercial software Motor-CAD is used to well establish analytical lumped circuit analysis software package which dedicates to the thermal analysis of cooling system. Reference [99] presents two LPTN thermal models for 15 kW and 5,5 kW EFC induction motors. The thermal model is used to identify the performance of the fan cooling system. Reference [100] describes a thermal network of winding water cooling

system for a synchronous machine. As a result, the winding temperature can be estimated by thermal model without thermal sensors. Reference [101] calculates the maximum temperature in the copper winding for an air-cored generator. An estimated convective heat transfer of 50 W/(m^{2}·K) from empire correlatives was used in the calculation, while an average value of 60 W/(m^{2}·K) was measured from the prototype.

Due to the operating temperatures inside the large machines varying significantly depending on location, thermal modelling using only a lumped parameter thermal model is not sufficient to predict the temperature distribution precisely.

Table 2-3. The flow resistance coefficient.

Friction loss coefficient		
Stationary pipe $k_l = f_s \cdot L/D$	$f_s = \begin{Bmatrix} 64/Re; Re < 2300 \\ 0.316/Re^{0.25}, 4000 < Re < 10000 \end{Bmatrix}$	[102]
Rotating shaft $k_l = f_r \cdot L/D$	$\frac{f_r}{f_s} = \begin{Bmatrix} 1; V_r/V < 0.35 \\ 0.579(V_r/V)^{-0.52}; 0.35 \le V_r/V \le 0.8 \\ 0.47(V_r/V)^{-1.42}; 0.8 < V_r/V) < 1.2 \end{Bmatrix}$	[103]
Air gap $k_l = f_r \cdot L/D$	$\frac{f_r}{f_s} = \{1 + (7/8)^2 (Re_r/2Re)^2\}^{0.38}$	[104]
Rotor ducts $k_l = f_r \cdot L/D$	$\frac{f_r}{f_s} = \begin{Bmatrix} 0.5{Re_r}^{0.16} Re^{-0.03}; 900 < Re < 9880 \\ 0.842{Re_r}^{0.023} Re^{0.002}; Re > 9880 \end{Bmatrix}$	[105]
Sudden expansion, contraction loss coefficient		
Stationary pipe	$k_l = (1 - A_i/A_o)^2;$	[102]
Entrance of air gap	$k_l = 0.1(V_r/V)^2 - 0.06(V_r/V);\ V_r/V > 1$	[106]
Entrance of Rotor ducts	$k_l = 0.234(V_r/V)^2 - 0.043(V_r/V); V_r/V > 0.5$	[107]

Table 2-4. Heat transfer coefficient of various cooling system.

Natural cooling		
Cylinder housing	$Nu = \begin{Bmatrix} 0.525(Gr \cdot Pr)^{0.25}; Gr \cdot Pr < 10^9 \\ 0.129(Gr \cdot Pr)^{0.33}; Gr \cdot Pr > 10^9 \end{Bmatrix}$	[36]
Finned housing	$Nu = \begin{Bmatrix} 5.22 \cdot 10^{-3}(Gr \cdot Pr \cdot nS/L)^{0.57}(S/L)^{0.412}(H/L)^{0.656}; \\ 10^6 < Gr \cdot Pr \cdot nS/L < 2.5 \cdot 10^7 \\ 2.78 \cdot 10^{-3}(Gr \cdot Pr \cdot NS/L)^{0.57}(S/L)^{0.412}(H/L)^{0.656}; \\ 2.5 \cdot 10^7 < Gr \cdot Pr \cdot nS/L < 1.5 \cdot 10^8 \end{Bmatrix}$	[108]
Forced cooling		
Cylinder housing	$Nu = \begin{Bmatrix} 0.664Re^{0.5} \cdot Pr^{0.33};\ Re < 5 \cdot 10^5; 0.6 < Pr < 50 \\ (0.037Re^{0.8} - 871) \cdot Pr^{0.33};\ Re > 5 \cdot 10^5 \end{Bmatrix}$	[36]
Finned housing	$Nu = 0.03Re^{0.8}\{1 - 0.23(L/S)^{0.5}(L - H/L)^{1.5}\};$ For turbulent flow	[38]
Housing jacket	$Nu = \begin{Bmatrix} 3.66 + 0.668Re \cdot Pr \cdot D/L \cdot/\{1 + 0.04(Re \cdot Pr \cdot D/L)^{0.667}\}; \\ 2300 < Re \\ 0.125m(Re - 1000) \cdot Pr/\{1 + 4.49m^{0.5}(Pr^{0.667} - 1)\}; \\ 3000 < Re < 5 \cdot 10^6, m = (0.79 \ln Re - 1.64)^{-2} \end{Bmatrix}$	[109]
Rotational hollow shaft	$Nu = \begin{Bmatrix} 0.019Re^{0.93} + 8.51 \cdot 10^{-6}Re_r^{1.45}; \\ 0 < Re < 3 \cdot 10^4, 1.6 \cdot 10^3 < Re_r < 2.77 \cdot 10^5 \\ 2.85 \cdot 10^{-4}Re_r^{1.19};\ Re_r > 2.77 \cdot 10^5 \end{Bmatrix}$	[84]
Spray cooling	$Nu = Pr^{0.4}\{0.785Re^{0.5} \cdot L/D \cdot A_r + 0.0257Re^{0.83} \cdot L/L^* \cdot (1 - A_r)\};$ $A_r = \frac{\pi(1.9d)^2}{L^2}, L^* = \frac{0.5 \cdot (1+\sqrt{2})L - 3.8d}{2}$	[90]
Heat pipe	$Nu = 4.728 \cdot 10^{-7}Re^{1.986}\, c_p \Delta T/h_l$	[110]

2.4.2 Numerical Approach

The numerical approaches based on the time step Finite Element Analysis (FEA) and Computational Fluid Dynamics (CFD) methods are commonly applied to the complicated cases (e.g. in case of a rotor duct, or a mounted fan system). However, the model setup and computations can be highly time-consuming especially when 3D modelling in necessary. More importantly, accurate modeling of numerical methods are highly dependent on input components such as material properties, data for material interfaces and boundary conditions.

The FEA is a highly accurate tool for modelling the solid conduction heat transfer. However, FEA suffers from the problems with uncertainty in the computation of thermal

resistances due to interfaces and convection [111]. Furthermore, in case of the cooling by connecting two different media, CFD needs to be employed to predict the coolant velocity distribution and pressure drops in the cooling ducts as well as the coolant heat transfer coefficient at the boundaries through the complex shape area. CFD is based on the finite volume technology with the aim of simulating 3-D laminar or turbulent flow with a high degree of accuracy. The main challenges of CFD modelling for convective heat transfer include selections of meshing approach, governing equations, and turbulent models, as well as the setup of boundary conditions, wall treatment and moving reference frames. On this basis, the applications and comparisons of the most used turbulent models are shown in Table 2-5. In addition, a fundamental description of the numerical thermal modelling of the hollow-shaft cooling and its critical regions will present in next chapter.

Table 2-5. The applications and comparisons of tubule models.

Model	Applications	Comments	Time cost
Standard k-ε	[30] addresses the flow velocity, the drop in pressure and the HTC of water in the water jacket cooling channels.	Robust industry standard model, and only valid for fully turbulent flows. Performs poorly for complex flows involving separation and strong streamline curvature.	Low
Realizable k-ε	[112] studies the HTC between air and stator of an air-cooled machine; [113] investigates the characteristic curve of a fan.	Performance generally exceeds the standard k - ε model. Performs well for complex flows with large strain rates, but still suffers from the inherent limitations of an isotropic eddy-viscosity model.	
Standard k-ω	[114] investigates the HTC of end windings for an EFC motor.	The k-ω models improve performance for boundary layers as compared to k-ε. Suitable for wall-bounded boundary layer, free shear, separated and low-Reynolds number (i.e. transitional) flows. But sensitivity to freestream	
Shear stress transport (SST) k-ω	[115] studies the flow, thermal and windage losses characteristics of fan blades;[21] addresses the HTC associated with a shaft-cooling of the traction motors.	Performs well for swirling flows without requiring sublayer damping and improves the separation flow prediction. Less sensitive to freestream than the standard model.	
RST	[116] investigates the heat transfer on the outward corrugated tube.	The RST model has the potential to predict complex flows more accurately than eddy viscosity models due to specific Reynolds Stress Tensor are calculated directly by taking account of the effects of turbulence anisotropy [117].	High

The friction coefficients and heat transfer coefficients are need to be predicted near the wall. Thus, it is crucially to choose the right combination of near wall mesh resolution and wall treatment. In addition, the turbulent flows are significantly affected by the presence of walls. The k-ε and RST models are mainly valid for turbulent core flows that occur away from the walls; and hence they are coupled with wall functions to bridge them with the calculated variables in the viscosity-affected region. The k-ω models are designed to be applicable throughout the boundary layer with a sufficient near-wall mesh.

Moreover, the accuracy of the CFD analysis also depends on the quality of the data input by the user, e.g. the mesh size, the boundary condition and the material properties.

2.5 Summary

A summary of practical methods and apparatuses for various types of cooling of automotive traction motors has been presented. Depending on the capacity and installation conditions of an electric motor, a single or a number of cooling techniques can be applied accordingly. Although the analytical approach is often limited to the geometrics and topologies and while the accuracy depends on a number of empirical correlations, this approach can still offer a fast and simple preliminary solution. If we use FEA effectively in modelling the solid conduction of heat, it is essential that a predicted heat transfer boundary needs to be defined. The CFD may provide detailed insights to into the kinds of outputs achieved from the cooling system, while being computationally laborious and time intensive. A combination of the empirical formulations and the computational technologies can benefit from both analytical and numerical approaches, whereupon a relatively simple and more accurate thermal model might be obtained.

3 CFD Modelling of the Heat Transfer Coefficient for a Low Speed Water-Cooled Hollow-Shaft Rotor Cooling System

Testing of a complete machine may not be applicable in this study because it is difficult to directly measure the loss and temperature of the rotor when using a complete machine. On this basis, an aluminium tube was selected to represent the shaft considering the complexity and cost of manufacturing for the first test reported in Chapters 3 and 4. More importantly, the turbulent flow generated within the aluminium tube hole is an ideal model for mathematical analysis [118]. This is because there are no further flow disturbances in the tube due to changes in flow direction and flow cross-sectional area. In addition, the maximum rotational speed of water-cooled shaft is 4500 rpm. The second test rig in Chapters 5 and 6 utilized a complex shaft that can be widely applied in real traction motors. The coolant for this test was oil-based regarded as laminar flow, which are used in the most automotive traction motors. In addition, the testing speed has been increased up to 30,000 rpm, where such high speed meets the requirements of most traction motors. The two test rigs employed different ways of generating heat: driving the shaft to rotate, forcing the coolant into the rotating shaft and collecting the coolant from the outlet. These provide various practical solutions for creating such hollow-shaft cooling systems in the electric machine. These can provide designers with some ideal choices, based on speed and cost requirements.

3.1 Introduction

Determination of the HTC is a critical parameter essential to the accurate thermal modelling of electrical motors. However, in cases where a hollow-shaft rotor cooling system is employed, calculation of heat transfer can be complex. A secondary flow will occur as a result of the shaft rotation. Consequently, due to the centrifugal and Coriolis effect, the cold and dense fluid in the centre will move radially to the wall. As a result, the convective HTC correlations of a stationary case is invalid for a hollow-shaft rotor cooling system. Reference [119] observes that the rotation has a destabilizing effect on a laminar flow, which entail a enhance heat transfer rate. Reference [118] points

out that the flow is initially turbulent, whilst the rotation reduces the heat transfer rate due to the stabilizing effect. However, these studies are relevant to cases where a high value in the length to diameter ratio is attained. Reference [120] shows that at the entrance of the pipe, the rotation causes a destabilization on the flow resulting in a swirling. This is due to the large shear caused by the rotating pipe wall. Reference [84] concludes that the pipe rotation entails an increase heat exchange between the moving wall and the air. However, in the literature hitherto there are still limitations in relation to how the unique governing correlations or trends for the liquid coolant convection HTC on a rotating system have been described.

A numerical simulation method may provide reliable estimates regarding the convective HTC of complicated rotary systems [21]. In [121], the HTC of the air-cooled rotor surface is investigated using the standard k-ε model with the standard near wall treatment. The predicted values derived from the CFD model tend to produce a 30% variation as compared with the experimental results. Different Reynolds-Averaged Navier-Stokes (RANS) turbulence models were used to calculate the HTC of the air-gap for a hydro-generator rotor-stator system [122]. By comparing the HTC results with the experimental data obtained from [123], all turbulence models mirror the general trend of the experimental results. The shear stress transport (SST) model, moreover, shows a better agreement with such results.

This chapter addresses the hollow-shaft rotor cooling of a traction motor. As is depicted in Fig. 3-1, the coolant is forced to pass through a hollow-shaft via two rotary couplings in order to cool the motor. The derivations of the convective HTC by CFD are presented. For a CFD study, the mesh of model is necessary for pre-processing procedure. The domain of model is divided into computational cells and nodes. Then, the integral form of the conservation laws is transformed into discrete algebraic equations in each element, which is known as finite volume method. In this chapter, the governing equations of CFD are presented, then the solution methods used in the commercial software STAR-CCM+ [124], deployed in the thesis, will be discussed.

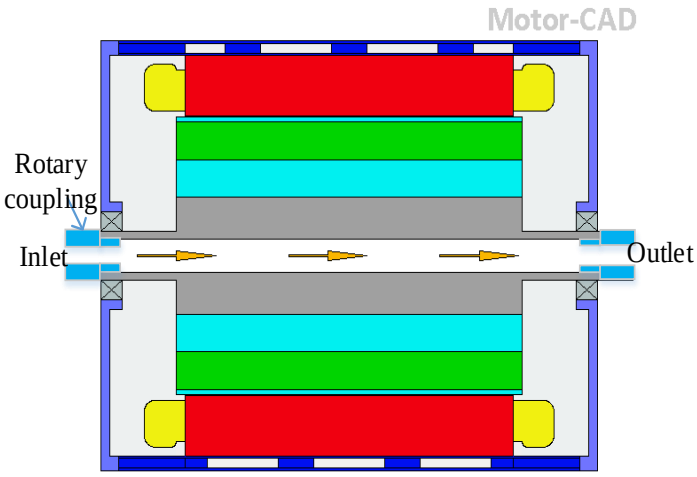

Fig. 3-1. Hollow-shaft rotor cooling scheme.

3.2 The Hollow-Shaft Modelling and Mesh Definition

A three dimensional mesh of the hollow shaft shown in Fig. 3-2 is used to simulate the flow dynamic and heat transfer in the STAR-CCM+ [124]. The active part of the shaft is 150 mm in length with an internal hole (for the passage of coolant) of 12 mm in diameter. Fig. 3-3 shows a symmetrical cross section of the model. The white region refers to the solid shaft, in relation to which the computational cells need to be calculated using the heat energy equation. Whereas for the fluid regions (as represented by the blue domain), not only the heat equation but also the flow and RANS equations need to be resolved. As for the properties of the coolant and the shaft in the CFD model, pure water and aluminium are used to represent them respectively. The water is assumed to be an incompressible Newtonian fluid with constant fluid properties.

Polyhedral mesher is employed to generate a volume mesh that is composed of polyhedral-shaped cells. A conformal mesh is created encompassing separate geometrical parts without interrupting the continuity of the mesh between the solid and the fluid domains. In addition, prism layer mesh is used to add prismatic cell layers next to wall boundaries to capture velocity and thermal boundary layers at the wall. The mesh size is set to be 2 mm and 10 prime layers are used to generate orthogonal prismatic cells next to wall surfaces with ratio of 1.4 for layer stretching. As a result, the total number of computational cells of fluid is approximately 0.15 million, whereas for solid, it is about 0.25 million.

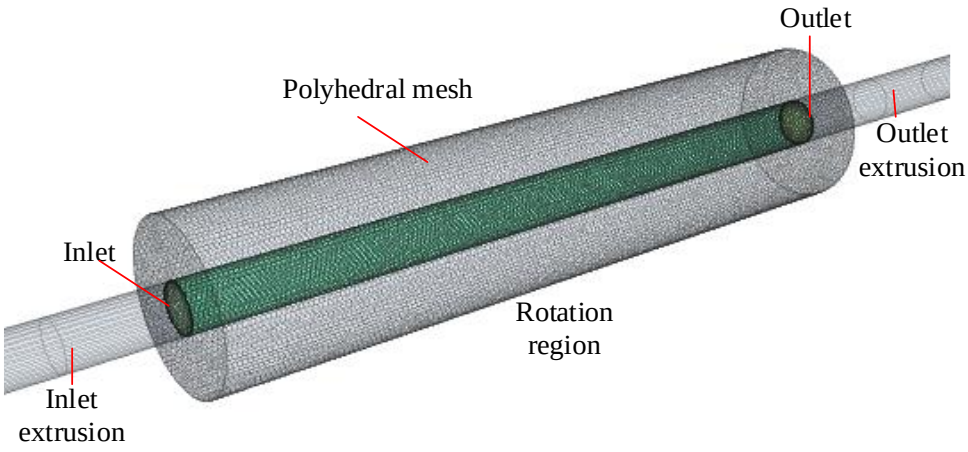

Fig. 3-2. 3D mesh.

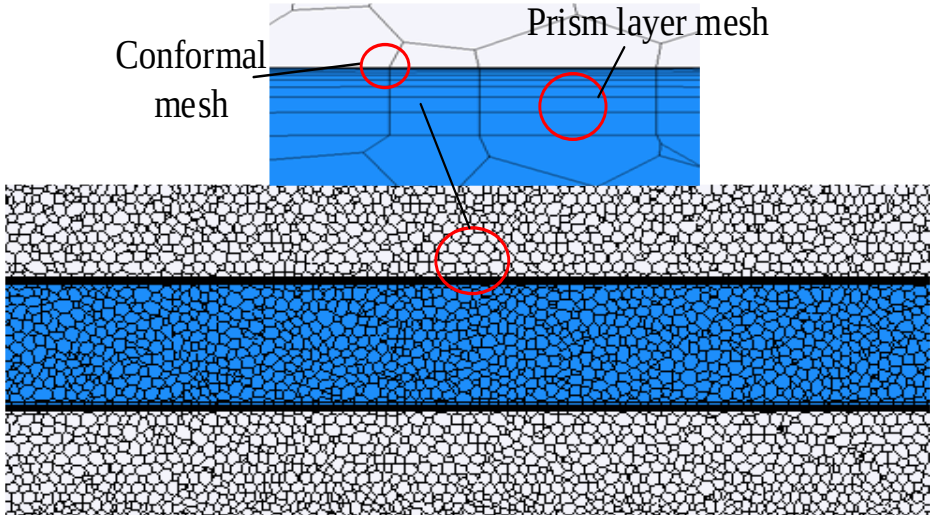

Fig. 3-3. Mesh setup for cross section plane (Grey – Solid, Blue – Liquid) models.

3.3 Governing Equations

3.3.1 Reynolds Averaged Navier-Stokes (RANS) Equations

The incompressible Navier-Stokes equations in conservation form are following [125]:

$$\frac{\partial u_i}{\partial x_i} = 0 \tag{3-1}$$

$$\rho \frac{\partial u_i}{\partial t} + \rho \frac{\partial u_i}{\partial x_j}\left(u_j u_i\right) = -\frac{\partial p}{\partial x_i} + \frac{\partial}{\partial x_j}\left(2\mu S_{ij}\right) \tag{3-2}$$

Where u is the fluid velocity component, S_{ij} is the strain-rate tensor.

For turbulent flow, the field properties become random functions of space and time. Hence, the field variables u_i and p_i are decomposed into time-averaged and fluctuating components as

$$u_i = U_i + u_i', p_i = P_i + p_i' \tag{3-3}$$

Substituting (3-3) into (3-1) (3-2) and the RANS equations are following [126]:

$$\frac{\partial U_i}{\partial x_i} = 0 \tag{3-4}$$

$$\rho \frac{\partial U_i}{\partial t} + \rho \frac{\partial}{\partial x_j}(U_i U_j) = -\frac{\partial P}{\partial x_i} + \frac{\partial}{\partial x_j}(2\mu S_{ij} - \rho\overline{u_i' u_j'}) \tag{3-5}$$

$$S_{ij} = \frac{1}{2}(\frac{\partial U_i}{\partial x_j} + \frac{\partial U_j}{\partial x_i}) \tag{3-6}$$

The quantity $\tau_{turb} = -\rho\overline{u_i' u_j'}$ is known as the Reynolds stress tensor which is symmetric and thus has six components.

$$\tau_{turb} = -\rho\overline{u_i' u_j'} = -\rho\begin{pmatrix} \overline{u'u'} & \overline{u'v'} & \overline{u'w'} \\ \overline{u'v'} & \overline{v'v'} & \overline{v'w'} \\ \overline{u'w'} & \overline{v'w'} & \overline{w'w'} \end{pmatrix} \tag{3-7}$$

By the application of (3-4), (3-5) can then be expressed as:

$$\frac{\partial U_i}{\partial t} + U_j \frac{\partial U_i}{\partial x_i} = -\frac{\partial P}{\partial x_i} + \upsilon \frac{\partial^2 U_i}{\partial x_i \partial x_j} - \frac{\partial \overline{u_i' u_j'}}{\partial x_j} \tag{3-8}$$

By decomposing the instantaneous properties into time-averaged and fluctuating components, additional unknown quantities are introduced. The same number of closure equations are necessary to solve these unknowns. In the following section, several approaches (turbulence models) are described in order to solve the RANS equations.

3.3.2 Energy Equation

Based on the first law of thermodynamics, the energy change of the fluid element is equivalent to the heat into this element plus the work done by the surface forces. However, the energy change due to the mechanical force is neglectable. This energy only important for the flow with the high viscosity and velocity gradient. On this basis, the energy conservation equation can be expressed as following [127]:

$$\rho C_p U_j \frac{\partial T}{\partial x_j} = \lambda \frac{\partial^2 T}{\partial x_j \partial x_j} \tag{3-9}$$

Not only the solid region but also the fluid domain, the heat equation needs to be calculated. For the solid heat conduction, the velocity components are set to be zero.

3.4 Turbulent Models

A rotating reference frame is created to model the scenario where, alongside the coolant, the rotation of the shaft for the steady state takes place. A constant rotational force is generated to mimic rotating effects in the rotating domain. Based on the finding in [120], the rotation may destabilize the flow due to the large shear caused by the rotating pipe wall. The rotational speed of 4500 rpm is sufficient to trigger turbulence at the entrance of the pipe with a rotation Reynolds number Re_r of up to 1.5×10^4. Therefore in the present study, turbulent models are employed to provide closure to the RANS equations. The choice of the turbulence model depends on its accuracy concerning the Reynolds stresses and the heat dissipation. On this basis, three improved turbulent models selected and compared in order to provide a better understanding of the rotating effect on the flow:

- A Realizable k-ε model with a two-layer enhanced wall treatment;
- A SST k-ω model with a non-linear constitutive relation;
- A Reynolds Stress Transport (RST) model.

3.4.1 Eddy Viscosity Models

Eddy viscosity models are based on Boussinesq assumption to model the Reynolds stresses tensor as a function of mean flow quantities. In this assumption, the Reynolds stresses is linked to the mean strain rate of deformation through eddy viscosity μ_t, and defined as (3-10). Two different eddy viscosity models (k-ε and k-ω) are used to calculate the turbulent eddy-viscosity in this thesis.

$$-\rho\overline{u_i u_j} = 2\mu_t S_{ij} - \frac{2}{3}\rho k \delta_{ij} \tag{3-10}$$

Where k is the turbulence kinetic energy; δ_{ij} is the Kronecker delta which is a function of two variations, δ_{ij} = 1, if $i = j$ and δ_{ij} = 0 otherwise.

3.4.1.1 Realizable k-ε

The k-ε models are a good compromise between robustness and accuracy for a larger range of flow configurations. In this model, the turbulent eddy-viscosity is defined as a function of the turbulent kinetic energy (k) and the turbulent dissipation rate (ε). The transport equations for the k and the ε are defined as [128]:

$$\frac{\partial}{\partial t}(\rho k) + \frac{\partial}{\partial x_i}(\rho k U_i) = \frac{\partial}{\partial x_i}\left[(\mu + \frac{\mu_t}{\sigma_k})\frac{\partial k}{\partial x_i}\right] + G - \rho\varepsilon \tag{3-11}$$

$$\frac{\partial}{\partial t}(\rho\varepsilon) + \frac{\partial}{\partial x_i}(\rho\varepsilon\overline{U_i}) = \frac{\partial}{\partial x_i}\left[\left(\mu + \frac{\mu_t}{\sigma_\varepsilon}\right)\frac{\partial \varepsilon}{\partial x_i}\right] + C_{\varepsilon 1}P_\varepsilon\varepsilon - C_{\varepsilon 2}\varepsilon^2\rho/(k + \sqrt{\frac{\mu_t\varepsilon}{\rho}}) \tag{3-12}$$

The turbulent eddy viscosity μ_t is determined as:

$$\mu_t = \rho C_\mu \frac{k^2}{\varepsilon} \tag{3-13}$$

$$G = 2\mu_t {S_{ij}}^2 - \frac{2}{3}\rho\frac{\partial u_i'}{\partial x_i} - \frac{2}{3}\mu_t(\frac{\partial u_i'}{\partial x_i})^2 \tag{3-14}$$

$$P_\varepsilon = \sqrt{2S_{ij}S_{ji}} \tag{3-15}$$

The turbulence model coefficients σ_k, σ_k, and $C_{\varepsilon 2}$ and the auxiliary relations of $C_{\varepsilon 1}$ and C_μ are described in [117].

In comparison with the standard model, the Realizable k-ε model includes a new transport equation for ε. Furthermore, a critical coefficient C_μ is used to express a function of the flow velocity and turbulence properties rather than assumed constant [128]. On these bases, the Realizable k-ε model can generally make the results more accurate.

The two-layer approach allows the k-ε model to be employed in the viscous-affected layer. In this approach, the values of the ε and μ_t in the layer next to the wall are determined as the function of wall distance. On other hand, the turbulent dissipation rate ε in the near-wall layer are blended smoothly based on the values from far from the wall [129] .Moreover, the turbulent kinetic energy k is specified across the full flow regime. This explicit calculations of ε and μ_t offer the better results than the damping function methods [117]. In spite of the fact that the two-layer models are very expensive

in terms of computational time. Accurate prediction of the near-wall resolution is crucially for modelling the heat transfer from the wall.

3.4.1.2 Shear-Stress Transport k-ω Model

The k-ω turbulence model is also a two-equation model that solves transport equations for the turbulent kinetic energy k and the specific dissipation rate ω, defined as (3-16) (3-17) [130]. This models are similar to k-ε models, but with the turbulent dissipation rate replaced by the ω, which is defined as the dissipation rate per unit turbulent kinetic energy ($\omega \propto \varepsilon/k$) — in order to determine the turbulent eddy viscosity.

$$\frac{\partial}{\partial t}(\rho k) + \frac{\partial}{\partial x_i}(\rho k U_i) = \frac{\partial}{\partial x_i}\left[(\mu + \sigma_k \mu_t)\frac{\partial k}{\partial x_i}\right] + P_k - \rho\beta^* \omega k \tag{3-16}$$

$$\frac{\partial}{\partial t}(\rho \omega) + \frac{\partial}{\partial x_i}(\rho \omega U_i) = \frac{\partial}{\partial x_i}\left[(\mu + \sigma_\omega \mu_t)\frac{\partial \omega}{\partial x_i}\right] + P_\omega - \rho\beta\omega^2 \tag{3-17}$$

$$P_\omega = G_\omega + D_\omega \tag{3-18}$$

$$G_\omega = \rho\gamma\left\{2S_{ij}S_{ji} - \frac{2}{3}\omega\frac{\partial U_i}{\partial x_i} - \frac{2}{3}\frac{\partial^2 U_i}{\partial {x_i}^2}\right\} \tag{3-19}$$

$$D_\omega = 2\rho(1 - F_1)\frac{\sigma_{\omega 2}}{\omega}\frac{\partial k}{\partial x_i}\frac{\partial \omega}{\partial x_i} \tag{3-20}$$

The turbulent eddy viscosity μ_t is computed as:

$$\mu_t = \rho\frac{k}{\omega} \tag{3-21}$$

The turbulence model coefficients and auxiliary relations of $\beta*$, β, F_1, γ, σ_k, σ_ω and $\sigma_{\omega 2}$ are described [117].

The advantage of using the k-ω model is to improve the performance for boundary layers under adverse pressure gradients by applying throughout the boundary layer [130]. Moreover, the computation of wall distance is not required in this model. The disadvantage of the original k-ω model is that the computation of boundary layer is sensitive to the values of ω in the free-stream. This problem does not exist for the k-ε models, and was addressed by Menter, who recognized that the turbulent dissipation rate ε can be transformed into specific dissipation rate ω transport equation by variable substitution [131]. Finally, Menter introduced a linear constitutive equation after the modification and then named this model as SST k-ω model.

For SST Menter's original model uses the modulus of the vorticity tensor rather than strain rate tensor. However, the linear relation between the Reynolds stresses and the mean strain rate tends to strongly under predict the anisotropy of turbulence. Turbulence is anisotropic in the strong swirl flow. Moreover, this anisotropy of the Reynolds stresses not only affects the flow field but also the turbulent transport of scalars, such as temperature. To account this anisotropy of turbulence, the non-linear functions of the strain and vorticity-rate tensor are proposed. This non-linear constitutive relation of SST k-ω model perform better than the liner models in anisotropic turbulence.

3.4.2 Reynolds Stress Transport Models

The swirl is generally associated with the flows. Therefore, accurate modeling of turbulent swirling flows is important. Common turbulence models used in engineering calculations are eddy viscosity models which include zero-equation and two-equation models. However, it has long been recognized that this type of eddy viscosity model is not appropriate for predicting swirling flows. In fact, the deficiency of eddy viscosity models for swirling flows can be analytically demonstrated by modelling a fully developed rotating pipe flow. Measured swirl velocity in the pipe varies approximately as the square of the normalized radius, however, eddy viscosity models produce an exact linear profile of the swirl velocity, which describes a solid body rotation.

To avoid this kind of deficiency of eddy viscosity models, Reynolds Stress Transport (RST) models has been suggested for modelling of swirling flows because of its ability to simulate the effects of mean rotation and curvature. RST models, also known as second-moment closure models, directly calculate the components of the specific Reynolds stress tensor in (3-7) by solving their governing transport equations [117]. A direct solution of the stress-tensor components, requiring the solution of 5 additional transport equations. They are usually more accurate in almost all flow configurations, especially when the flow is strongly curved or the flow is undergoing strong rotation. These models tend to be less robust than eddy-viscosity models.

However, this requires solving many complicated second moment transport equations, which involve six Reynolds stresses plus other scalar fluxes and variances. Because of this complexity and the large computer resources required, second moment

transport equation models have not been successfully implemented in combustor swirling flows.

3.5 Boundary Conditions and Wall Treatment

The heat source similar to that of the experiment is applied with a uniform distribution to the shaft surface and can be functionally defined as the heat lost from a machine. The external surface of the shaft is modelled as an adiabatic boundary condition. On this basis, all the heat is dissipated to the coolant through a forced convection between the shaft's internal surface and the fluid. An inlet extrusion region at the inlet boundary is set in order to create a fully turbulent flow. The flow velocity is also set at the top of the inlet extrusion. An extrusion at the flow outlet is also put in place to avoid any flow reverse and, in such a context, 0 pa is defined as any flow that takes place at the top of the outlet extrusion. The inlet temperature and ambient temperature are both fixed at 20 ℃.

The turbulent flows are significantly impacted by the presence of walls. Thus, it is crucially to choose the right combination of near wall mesh resolution and wall treatment. As shown in Fig. 3-4, the near-wall region of the boundary layer can be split into three layers. The viscous sublayer is located in the inner layer, which is dominated by the molecular viscosity and the flow is almost laminar. The mean flow velocity in this layer is only determined by the fluid properties, and distance from the wall. In the outer layer, called the log-law layer, turbulent effect and viscous play a major role. Finally, there is a buffer layer as a transitional layer between the inner layer and the outer layer. To apply the law of the wall, the flow velocity U^+ and wall distance y^+ in the wall velocity profiles are expressed in dimensionless form as [132]:

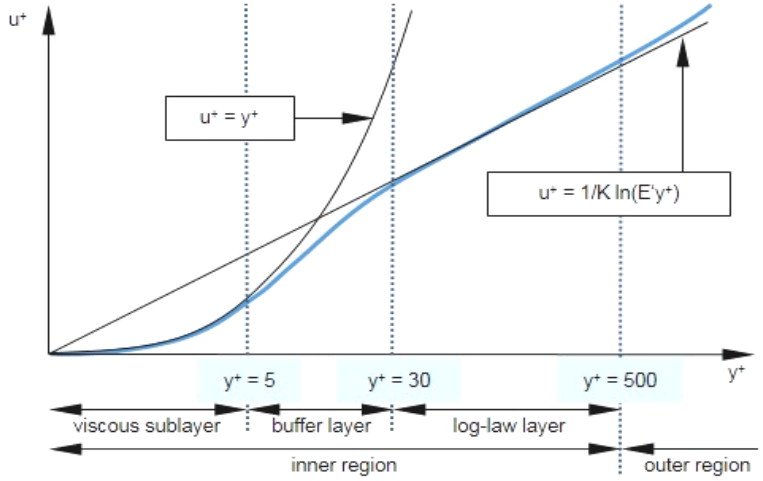

Fig. 3-4. The law of the wall [132].

$$U^+ = \frac{u}{u_\tau} \tag{3-22}$$

$$y^+ = \frac{\rho u_\tau y}{\mu} \tag{3-23}$$

$$u_\tau = \sqrt{\frac{\tau_w}{\rho}} \tag{3-24}$$

where y is normal distance from the wall, u_τ is the friction velocity, defined as τ_w is the wall shear stress.

For $y^+ < 5$,

$$U^+ = y^+ \tag{3-25}$$

For $y^+ > 30$,

$$U^+ = \frac{1}{0.41} ln\, y^+ + 5 \tag{3-26}$$

For $5 < y^+ < 30$, the buffer region can be solved by setting the $y^+ = 11$ as a boundary to distinguish the laminar profile from the turbulent profile.

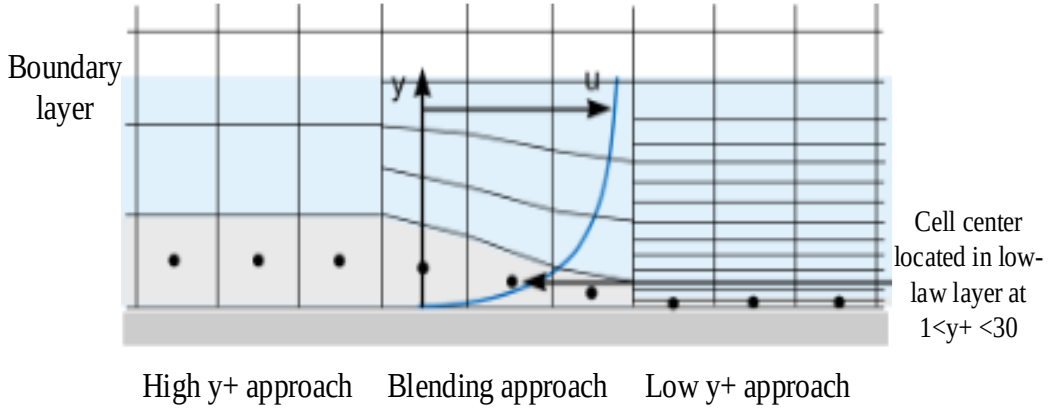

Fig. 3-5. All y+ wall treatment approach [117].

A “Wall Treatment” in STAR-CCM+ is the wall-function approach in order to model near-wall turbulence quantities such as dissipation rate , turbulent kinetic energy and wall shear stress [117]. All y+ Wall Treatment is a hybrid approach, as shown in Fig. 3-5, that seeks to represent the behaviours of the previous two wall treatments (low y+ Wall Treatment and High y+ Wall Treatment) in the limit of very fine or very coarse meshes. It is also developed with the desirable feature of providing reasonable results for intermediate meshes where the cell centroid falls within the buffer layer. Then the final value for these turbulence quantities are then calculated by the blending approach [117].

Hence, an all y+ wall treatment model [28] is applied for the profile of the mean flow quantities in the wall boundary layers. High resolution mesh is created at the wall boundary layer with the wall cell y+ ≤ 0.2, as shown is Fig. 3-6, to achieve accurate predictions in relation to the flow and turbulence parameters. The field functions of u+ and y+ are plotted in Fig. 3-7, This plot shows that the y+ range of data points match the correlations of various layers (shown in Fig. 3-4).

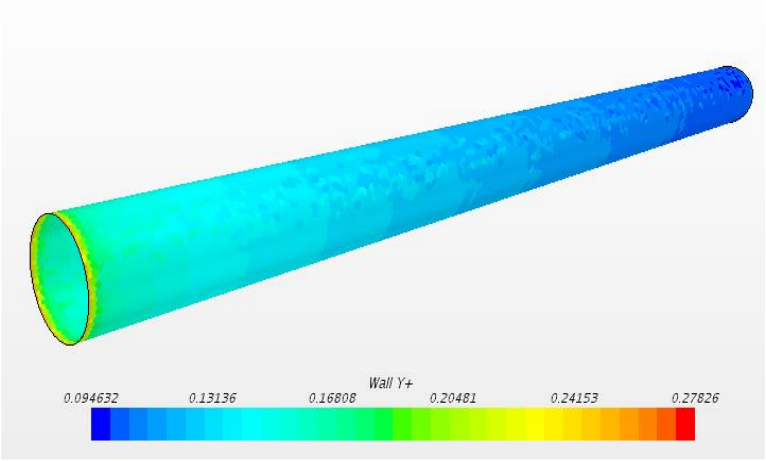

Fig. 3-6. Wall boundary layer y+.

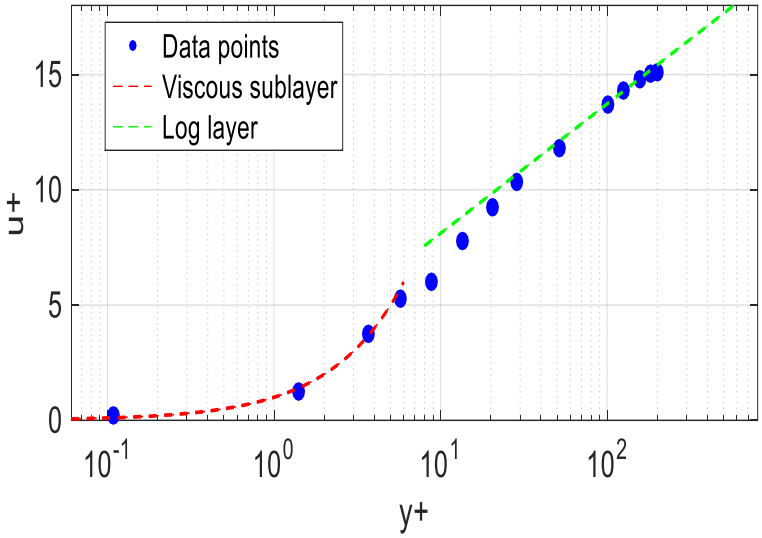

Fig. 3-7. The profiles of y+ and u+ at boundary layer.

3.6 Moving Reference Frames

The rotation strongly affects the flow and pressure drop in the pipe. The rotating modelling in CFD is crucial. A rotating reference frame (MRF) is created to model the scenario where, alongside the coolant, the rotation of the shaft for the steady state takes place. MRF is an efficient method to model a constant rigid motion and solve this motion in steady-state by applying appropriate acceleration into the cell. Moreover, the constant forces can be imposed in the rotating domain to mimic rotating effects without changing the position of cell vertices [133]. This provides a solution to represent the time-averaged behaviour of the flow. However, the MRF approach does not deal with

unsteady flow interaction effects between the moving and the surrounding stationary domains. In order to accurately capture such effects, a transient moving mesh approach should be applied which typically results in highly computational time-consuming. In this study, the MRF techniques are employed due to MRF is a good compromise between computational cost and accuracy.

3.7 Convective Heat Transfer Coefficient

The general formula that defines the heat transfer coefficient associated with a solid wall surrounded by a fluid is:

$$h = \frac{q^{"}}{T_{wall} - T_{fluid}} \tag{3-27}$$

Where $q^{"}$ is the heat flux removed from the wall, T_{wall} is the temperature of the wall and T_{fluid} is a temperature for the surrounding fluid. While the first two terms ($q^{"}$ and T_{wall}) are well defined, the latter T_{fluid} is quite ambiguous and subject to interpretation. However, in CFD it is often useful to get local information about the heat transfer coefficient, e.g. when data needs to be exported for structural analysis. In such cases the fluid temperature can be defined in various ways. CFD it is often useful to get local fluid temperature information about the heat transfer coefficient. However, T_{fluid} is difficult to measure during the test and is often replaced by an alternative fluid temperature. In this simulation, the fluid temperature can be defined as:

$$T_{fluid} = \frac{T_{inlet} + T_{outlet}}{2} \tag{3-28}$$

where T_{inlet}, T_{outlet} are the inlet and outlet flow temperatures,respectively. Please note that there is no "correct" choice for this, each of them is valid if properly interpreted together with their respective reference temperature. This is particularly relevant if the data have to be exported towards an external code.

3.8 Summary

This chapter presents a fundamental description of the numerical thermal modelling of the hollow-shaft cooling and its critical regions. Discussion over the theory behind CFD, mainly focusing on the aspects related to the HTC between a fluid and a solid are

provided here. It is important to understand the physical phenomena of fluid motion and how these phenomena are modelled in CFD.

4 Experimental Investigation of a Low Speed Water-Cooled Hollow-Shaft Rotor Cooling System

In this chapter, the experiments are carried on to validate the accuracy of CFD models which has been described in Chapter 3 with the assistance of an analytical lumped-parameter thermal network (LPTN) approach. This LPTN model is derived and calibrated by the experimental results to represent the heat transfer of the test rig. As a consequence, the values of internal wall temperature of the shaft and the active heat flux, which are both difficult to measure directly, are obtained using the proposed model. Then, the HTC results have been nondimensionalised into an equation using various dimensionless groups and can be applied in different geometrical contexts with various axial and rotation flow rates.

4.1 Test Rig Setup

Fig. 4-1 shows the schematic flow diagram of the experimental apparatus, where a circulation system is illustrated. Cool water is supplied to the hollow-shaft by a chiller. A three-way clamp connection T type valve is used to regulate the flow of water in the system and thus the flow rate is measured by a flow meter.

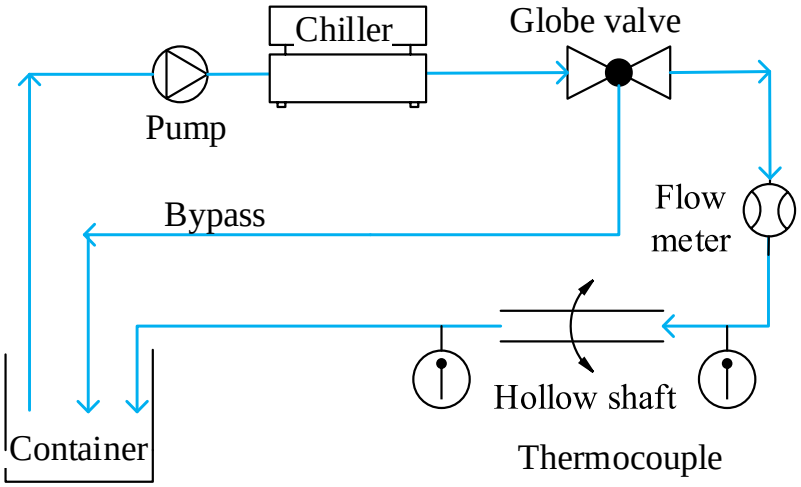

Fig. 4-1. Schematic diagram of the experimental setup.

Fig. 4-2 depicts the test setup. An aluminium tube was selected to represent the shaft. The heat transfer test section consists of a horizontal 12 mm internal diameter aluminium tube. When assembled, the internal active length is 150 mm. The biggest challenge for this test is how to force the coolant into the rotating shaft from a stationary

hose. The rotating part of the shaft is connected to the static part by two pipe rotary couplings, which are devices that provide a seal between the stationary hose and the rotating shaft to permit the flow of fluid in and out. However, with this arrangement, the drive motor cannot be connected through the shaft ends. On this basis, a pulley driven by an electric motor was used to accelerate the shaft to rotate up to 5000 rpm.

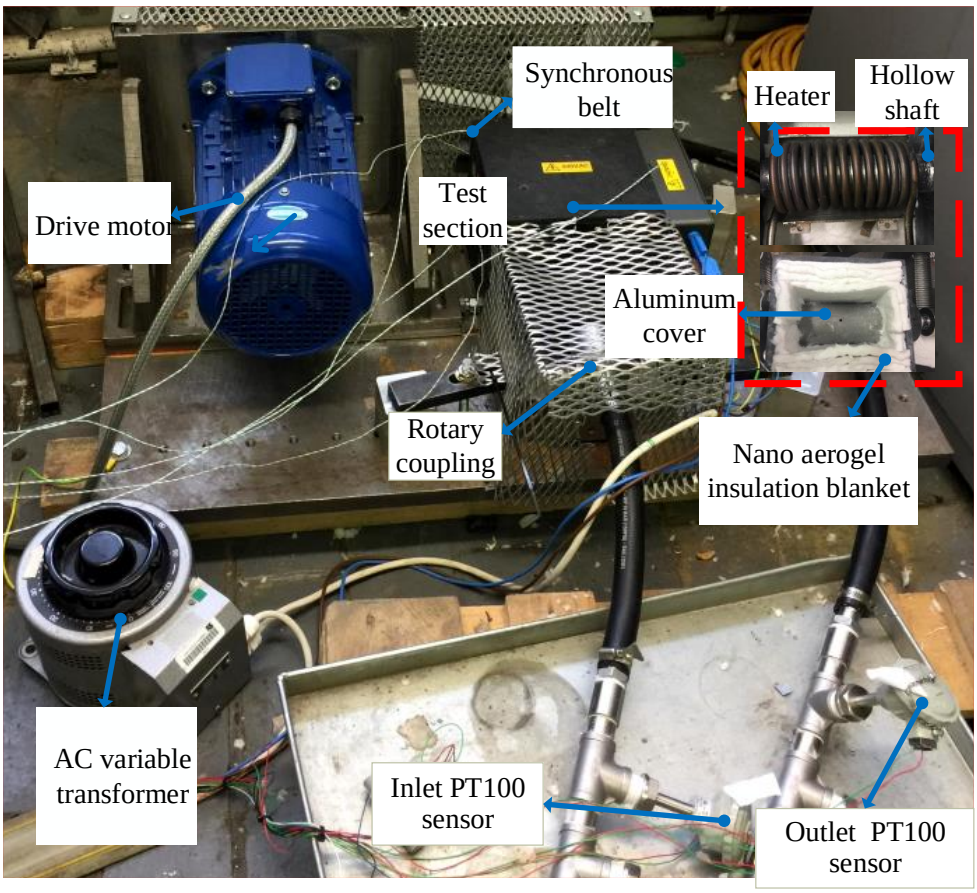

Fig. 4-2. Experiment setup.

For heat transfer analysis of hollow-shaft cooling, the ideal scenario is to create a constant temperature at the inner wall of the pipe to represent a perfect thermal boundary condition. However, it is difficult to keep the temperature of the rotating pipe wall constant during the test. In this test, a heater made using resistance wires is connected to the 220 V power supply to transmit the heat to the shaft by air convection, and is installed parallel to the axis. This can make sure the constant amount of the heat transferred to the shaft. Based on the initial testing trials, several measures were taken to minimize the diversion of the heat flow away from the shaft, ensuring most of the generated heat is transferred to the shaft body:

- A polished aluminium cover is wrapped around the heater to enhance the heat reflection back to the shaft;
- A Nano aerogel insulation blanket, with a thermal conductivity of 0.0287 W/mK at 350 ˚C, and with a maximum tolerance of up to 800 ˚C without bursting into flames or suffering any deformation, is packed around the outside of the aluminium cover;
- The shaft and the aforementioned reflective and insulating layers are further placed in a box made from an insulating synthetic stone carbon fibre material.

4.2 Measurement

4.2.1 Temperature Measurement

As Fig. 4-3 illustrated in two four-wire Omega Pt100 sensors (9, 10) with an accuracy of ± 0.05 ˚C are mounted using equal tees to measure the inlet and outlet coolant temperatures. The Pt100 sensor is a type of Resistance Temperature Detector (RTD) that converts the voltage drops of the thermocouples to digital values. RTDs possess the highest stability among temperature transducers and the output is also very linear, thus making RTDs a good choice when highly accurate and long-term measurements are required.

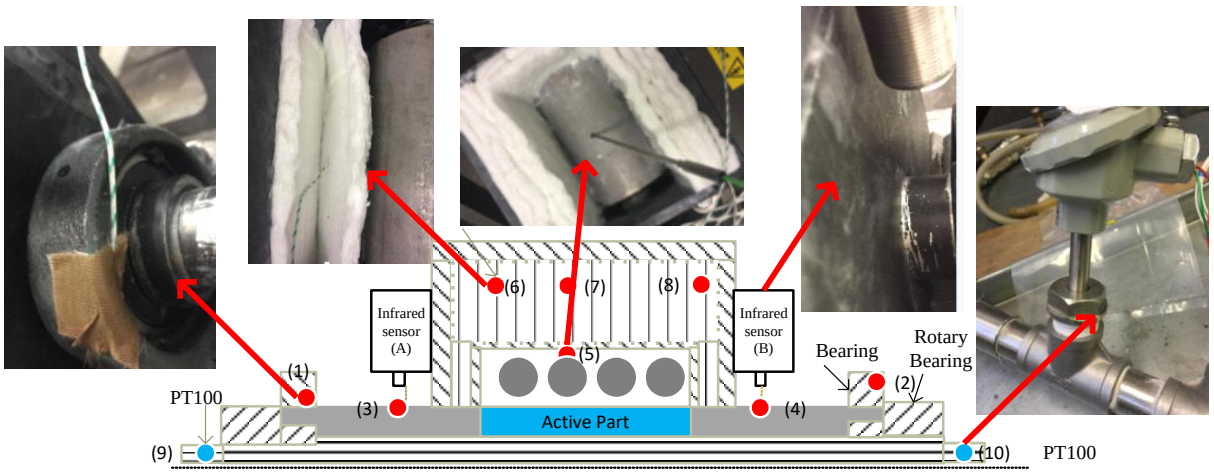

Fig. 4-3. Temperature sensor locations.

In order to provide an indicator for the thermal model estimation, shaft surface temperature has been measured. To avoid the complexity associated with rotary part measurements [134], a subminiature noncontact Omega infrared thermometer (A, B)

[135] is employed. In addition, a second calibration is taken in respect of the shaft at rest by a K type thermocouple (No. 3, 4).

Three K type thermocouples (No. 6, 7, and 8) are embedded in the Nano aerogel cover to avoid excessive temperature rise in this region. Another K type thermocouple (No. 5) stainless steel probe is attached to the heater to monitor its temperature. The bearing temperature, taken as an indicator to evaluate the thermal model is measured using a K type thermocouple (No. 1, 2).

The calibration of the K type thermocouple and infrared thermometer is described in Chapter 6. The location of the sensor described above ensures exposure to the local heat and temperature distribution in different regions of the testing set-up. This will be examined in the analytical calculations in the following chapters.

All the thermocouples are connected to the Agilent Technologies 34970A which combines data logging and data acquisition features. Through the built-in RS232 interface, the measured data can be sent to a connected computer. Measurements of the test variables are taken at each experimental condition for at least 30 minutes after equilibrium conditions have been established.

4.2.2 Control of Heater Unit

The heater was connected to a variable transformer for adjusting the power level. The Fluke True RMS Clamp meter was used to measure the RMS (root mean square) current (I_{rms}). The average power P_{ave} dissipated from the heater can be calculated from (4-1), where R_{heater} is the electric resistance of heater.

$$P_{ave} = {I_{rms}}^2 * R_{heater} \tag{4-1}$$

Fig. 4-4. The Fluke Ture RMS clamp meter.

4.3 LPTN Model

The merit of LPTN lies in the fact that the computational cost is less demanding as compared to using any numerical method (e.g. CFD). Once the model parameters are known, the resulting set of thermal algebraic and differential equations which completely describe the thermal performances of the machine at steady and transient states can be computed with ease. On the other hand, for complex fluid motion and convective heat transfer phenomena, the CFD method is used to provide inputs into the LPTN model. The coupled CFD and LPTN are processed as shown in Fig. 4-5.

The input boundary condition of LPTN model setup for the hollow shaft rotary cooling system is based on test rig. Firstly, the LPTN model setup is calibrated at a stationary case with the HTC from Gnielinski's correlation [109]. By comparing the results between the test and the LPTN models, it can be concluded that the developed LPTN model is able to represent the heat path taken in the test. After that the initial HTC under rotation conditions is investigated using CFD and thus this HTC is the input boundary condition.

The output of the LPTN model is the shaft external wall temperature. At this point, a decision is made to carry on or not depending on the outcome of a comparison with the test results. If external wall temperature of the shaft derived from the LPTN model are not the same as those obtained from the experiment, then a new iteration of the HTC is required until the difference of two results obtained between the LPTN model

and the experiment converge within a reasonable margin of error (±1 %). After the two sets of measurements more or less match, the next step can be taken in the flow chart, in which the active part of the shaft becomes the focus. A second decision is needed at this new stage involving a comparison of the HTC as between the active part of the shaft on the one hand and its initial estimation value on the other. If the two sets of the HTC results match, the initial estimation value is the final requirement. Otherwise the LPTN model should be modified by increasing the number of layers and thermal resistance. The flow chart has to restart until the satisfactory results. The proposed CFD and LPTN models respectively will be explained in detail in the following sections.

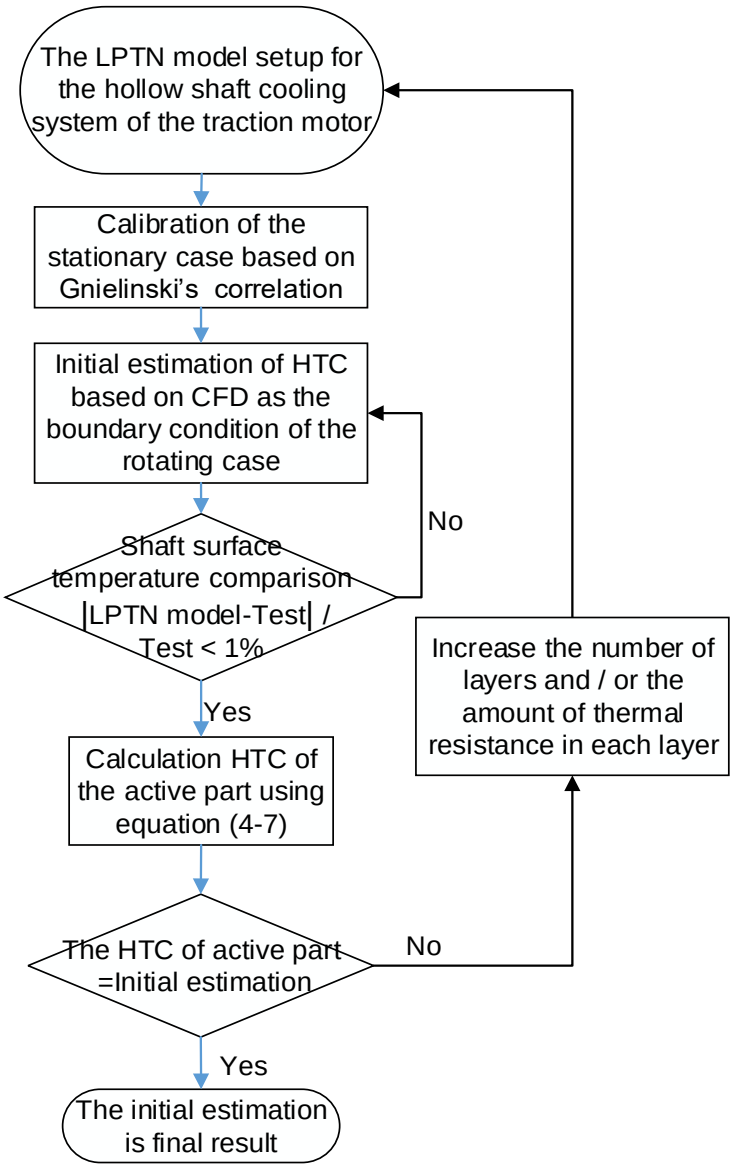

Fig. 4-5. Flow chart of coupled thermal analysis.

A LPTN model of the system is developed using PORTUNUS [20, 136]. To simplify the thermal model, the following assumptions are made:

- The outer surface of the shaft is modelled as an adiabatic boundary condition.
- The heat path goes through the shaft via conduction in the axial and radial directions, and via convection from the shaft walls to the coolant fluid. Unlike conduction and convection, radiation is not considered.
- The radial and axial heat flows are independent of each other.
- The heat is transferred to the shaft in a uniform manner and is thus evenly distributed in the body of the shaft.

4.3.1 The Equivalent Thermal Network

The number of model components used depends on a balance to be struck between the accuracy of the model on the one hand and its simplicity on the other. The shaft is divided into seven layers consisting of the following: three middle layers representing the active part; two side layers representing the bearings; and two remaining layers as the link function (see Fig. 4-6). The red and yellow arrows display the heat from the heater and the bearings, the light blue represents the solid conductivity, while the heat that transfers from the shaft to the coolant is indicated by purple arrows. The diagram of a one layer model is shown in Fig. 4-7, which consists of two major parts: the solid conductive circuit and the fluid convective circuit. The thermal resistances of the shaft are visualized as green blocks. R_{cd_a}, R_{cd_r} which are associated with the axial and radial heat flows respectively. The orange block (R_{cv}) represents the convective heat transfer from the shaft to the coolant. The heat flow in the coolant is modelled as a solid, with the conductive resistance R_{cd_w} displayed as the light blue block. The input temperature (T_{inlet}) of the flow is the output temperature of the previous layer and this output temperature is measured by the temperature meter (TM_c). The initial flow temperature can be derived from the temperature sensor (No. 9).

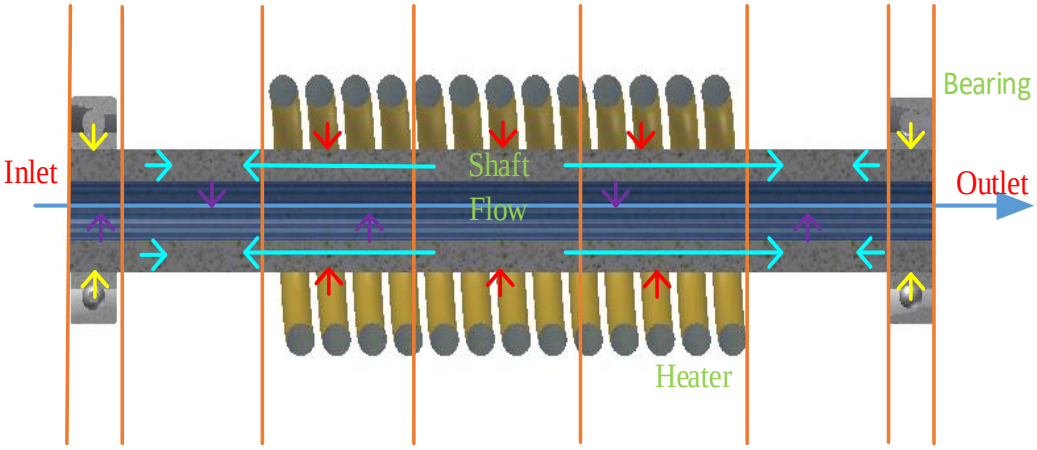

Fig. 4-6. Representation of the 7 nodal-network layers and heat transfer path.

In the heat-transfer network, a thermal resistance circuit describes the main paths for the heat flow, enabling the temperatures of the various components for a given heat source to be predicted. The thermal-conduction resistances and thermal-convection resistances, except that for the coolant, are defined as (4-2) to (4-4). The coolant thermal-conduction resistance is defined as (4-5). The linear formulations are used to replace the partial differential equations in order to express the thermal state and thus to minimize the computational time.

$$R_{cd\_a} = \frac{L}{\lambda A} \tag{4-2}$$

$$R_{cd\_r} = \frac{\ln\left(r_{outer}/r_{inner}\right)}{2\pi\lambda L} \tag{4-3}$$

$$R_{cv} = \frac{1}{hA} \tag{4-4}$$

$$R_{cd\_w} = \frac{1}{mc_p} \tag{4-5}$$

where L is the length of heat transfer path; A is the cross-sectional area perpendicular to the path; r_{inner} and r_{outer} are the inner and outer radius of the shaft; m is the fluid mass; c_p is the specific heat capacity of the fluid.

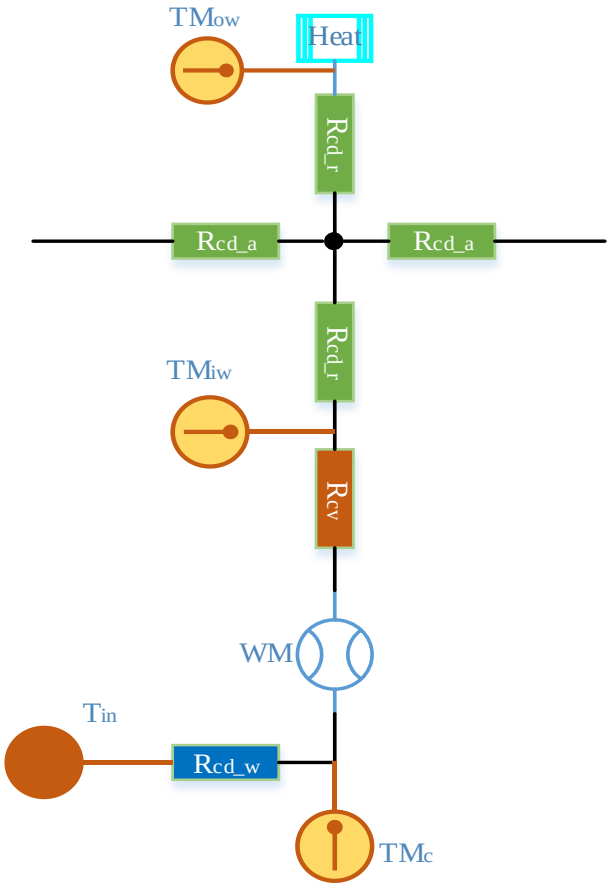

Fig. 4-7. One layer of developed LPTN model.

4.3.2 The Heat Sources

The total heat losses implemented in the model are equal to the heat that is taken away by the coolant. When passing through the shaft at a constant flow rate Q, the coolant is heated around the shaft's internal wall at a constant temperature, thus raising the temperature of the coolant from T_{inlet} to T_{outlet}. Based on the energy conservation equation, the rate of the heat transfer P_s from the shaft to the coolant is determined by the following equation:

$$P_s = \rho \cdot Q \cdot c_p(T_{outlet} - T_{inlet}) \tag{4-6}$$

4.3.3 The Heat Transfer within the Active Part

The Wattmeter (WM in Fig. 4-7) is placed between the shaft and the coolant and is used to measure the heat transferred from the shaft to the coolant in each layer. From the LPTN model, the active heat transfer P_a can be obtained from (4-7). The mean convection heat transfer coefficient h of the active part is calculated by (4-8):

$$P_a = W_1 + W_2 + W_3 \tag{4-7}$$

$$h = \frac{P_a}{A(T_{iw} - T_{ref})} \tag{4-8}$$

$$T_{ref} = \frac{T_{inlet\_a} + T_{outlet\_a}}{2} \tag{4-9}$$

where W_1, W_2, W_3 are the values of the Wattmeter in the three layers of the active part; T_{iw} is the average temperature of the shaft's internal wall, which is measured by TM_{iw}. T_{inlet_a} , T_{outlet_a} are the inlet and outlet flow temperatures in the active part, which can be obtained by temperature meter TM_c.

4.4 Results and Discussions

4.4.1 The Static Testing

In cases where the validation of the experimental method is carried out, the shaft is required to be at rest, so that the different effects due to the rotational speed can be better highlighted. The range of axial flow rate is from 2 L/min to 7 L/min, which is sufficient to trigger turbulence with Reynolds number ranging from 3521 to 10563. The convective coefficients from the various CFD models and the experiment are compared with the data from Gnielinski's correlations (4-10) [109], as is depicted in Fig. 4-8. Suited to the conditions of static testing, [28], Gnielinski's heat transfer correlation is applied to fully developed turbulent flows (i.e. 3000 < Re < 5*10^6). At the same time, the Darcy friction factor (f) from the Moody chart is taken into account for the smooth wall surface.

$$Nu = \frac{f}{8} \frac{(Re - 1000)Pr}{1 + 12.7\left(\frac{f}{8}\right)^{0.5}(Pr^{\frac{2}{3}} - 1)} \tag{4-10}$$

Where $f = (0.79\ln(Re) - 1.64)^{-2}$.

It is noted here that the three different turbulence models and the experimental data closely follow the trend of Gnielinski's correlation, with the RST and the k-ε models showing the smallest and the largest deviations respectively. These variations can be partly explained due to the rough shaft internal wall surface as compared to the perfectly smooth one assumed in the modeling. In addition, the heat is not evenly

radially distributed in the shaft, causing the external wall temperature of the shaft to rise higher than on the internal.

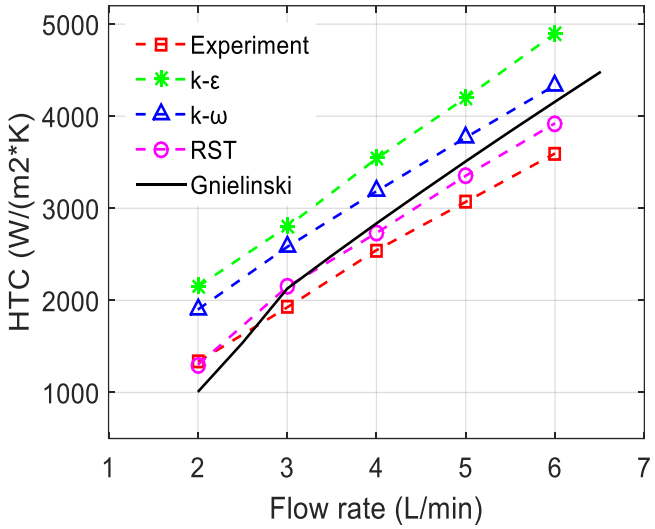

Fig. 4-8. Evolution of the HTC with different flow rates.

4.4.2 The Rotating Shaft with an Axial Flow

Two different steps were taken to calculate the input loss with the heater off and on, respectively, and from (4-6).

- Rotating the shaft with the heater off: P_1 is the bearing friction loss as a result of the shaft rotation. Through the experimental results, it is realized that the temperature of the end with the pulley drag is higher than that of the other end, suggesting that the drive end (DE) generates more friction loss than the non-drive end (NDE). From the test and the specification data of the bearing manufacturer [137], a DE to NDE bearing loss ratio of 1.2 is calculated and incorporated in the model.
- Rotating the shaft with the heater on: P_2 is the losses transferred to the shaft from the heater in addition to the bearing friction losses. Therefore, $(P_2 - P_1)$ is taken as the net loss that the shaft receives from the heater.

Table 4-1 lists the measured losses calculated from (4-6) and active heat transfer from (4-7) at the axial flow rate 2.5 L/min with various rotational speeds. Due to the short length of the shaft, the dynamic flow losses and windage loss are ignored. The resulting losses are assumed to be evenly transferred to the shaft as the heat source. It can be noticed that all the results obtained in Table 4-1 are proportional to the rotating speed.

This is because bearing friction losses rise at higher speeds. The input power of the heater is gradually raised by a transformer to highlight the variable performance when the rotating speed is increased. The amount of loss from heater is close to the heater power P_h that is measured by (4-1). As a result, the active heat transfer increases due to the improvement of heater power and HTC. The net loss between heater loss and active heat transfer is dissipated through other layers of shaft.

Table 4-1. The measured losses and active heater transfer.

Rotating Speed (rpm)	Bearing Loss P_1 (W)	Heater Loss (P_2-P_1) (W)	Active heat transfer P_a (W)
1000	58	205	115
2000	115	353	195
3000	175	492	266
4000	242	630	331

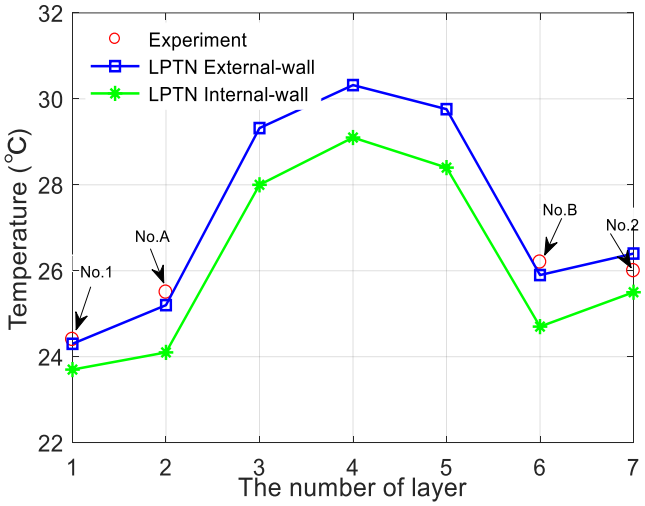

Fig. 4-9. Comparison of the results between experiment and LPTN model.

A comparison between, first, the measured results from sensors (1, A, B, 2) and, second, the developed LPTN model is presented in Fig. 4-9. The difference between the two sets of results is explained by the fact that the thermocouples (No. 1, 2) are mounted on the surface of the bearings. Due to the thermal resistance between the shaft and the bearings, the temperature of the bearings is lower than the shaft surface temperature. The results obtained from the infrared sensors (No. A, B) gave higher temperature values than the predictions derived from the LPTN model. The non-uniform distribution of the heat, which causes the surface heat density, is higher in the external part of the shaft than internally. However, these differences are all within a

reasonable margin of error. It can be concluded that the developed LPTN model is able to represent the heat path taken in the test shaft. The internal wall temperatures are calibrated from the LPTN model and then are used to calculate the HTC.

A comparison of the results obtained from the different turbulent models is presented in Fig. 4-10. It is noticed that the value of the HTC increases with the rotational speed in all the methods. To explain the boosting effects two phenomena can be addressed: Firstly, due to the heat source being on the shaft wall surface, the density of the fluid near the walls is less as compared to those close to the center regions. As a result, the centrifugal buoyancy which results from the density variation enhances the temperature exchange between the hot and the cold fluid particles. Secondly, due to the centrifugal and Coriolis effect caused by the shaft rotation, the cold and denser fluid in the center tends to move radially to the wall. This phenomenon changes the flow field in the shaft hole, resulting in a higher convective heat transfer coefficient.

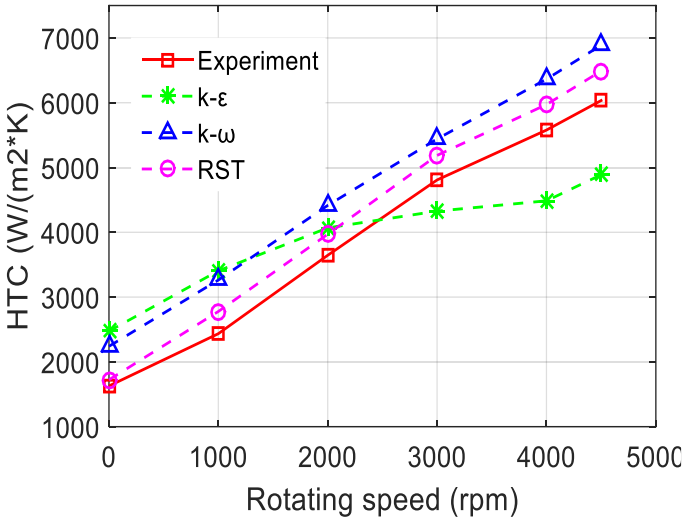

Fig. 4-10. Evolution of the HTC with different rotating speeds for the different models.

Table 4-2 presents the relative error ε between the three different CFD turbulence models and the experiment. The RST method has a smaller relative error than k-ε and SST k-ω models. The larger discrepancies can be explained by the fact that the k-ε model uses the Boussinesq assumption that the viscous stresses are proportional to the instantaneous rate of the deformation. This makes the Reynolds stresses proportional to the mean rate of deformation of the fluid element with turbulence viscosity assumed to be isotropic. In the case of the SST k-ω model, a non-linear formulation rather than a linear one is used to provide a better agreement with the

experimental data. This formulation accounts for the anisotropy by including the non-linear functions of the strain and vorticity-rate tensors, and has been shown to improve the turbulence predictions in relation to strong secondary flows. However, the simplistic eddy viscosity based on Boussinesq approximations for the Reynolds stresses does not represent the anisotropy of the flow field adequately.

To avoid this kind of deficiency of eddy viscosity models, a second order closure scheme RST model has been suggested to directly determine the components of the specific Reynolds stress tensors instead of specifying it by the Boussinesq approximation. Table 4-2 shows that the RST model predictions are in good agreement with the data. The RST model has the potential to predict complex flows more accurately than eddy viscosity models. It is because that transport equations of Reynolds stresses in RST models take account for the effects of turbulence anisotropy, swirl and streamline curvature. However, the RST model proves very expensive in terms of computational time as five additional equations require some time in order to be solved.

Table 4-2. Comparison the relative errors between CFD and testing results.

Rotating speed (rpm)	1000	2000	3000	4000	4500
ε_k-ε (%)	28	7	11	24	21
ε_k-ω (%)	34	18	13	14	16
ε_RST (%)	12	6	7	7	9

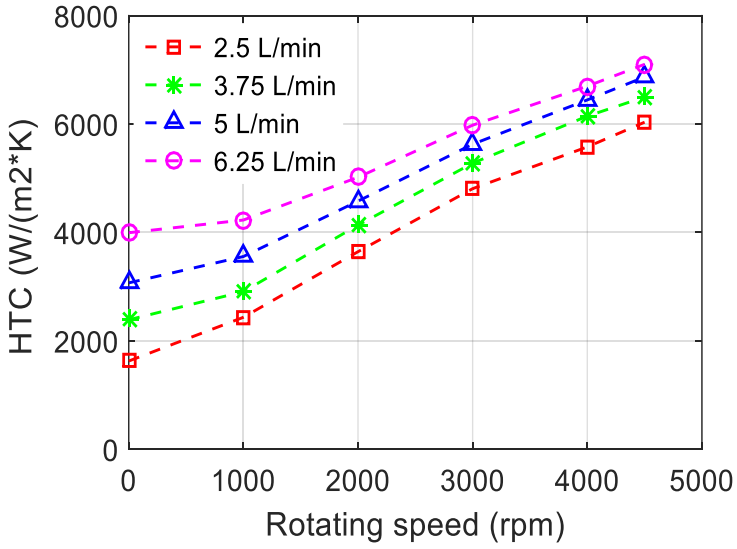

Fig. 4-11. Evolution of the experimental HTC with rotating speeds for various axial flow rates.

It is found that the RST and SST k-ω models tend to always over-predict the HTC as compared with the experimental measurements. The discrepancy can be explained by the non-uniform distribution of the heat in the shaft surface causing the surface temperature to increase further. Fig. 4-11 presents the experimental Nusselt values obtained for the various axial flow rates. The increase in the coolant flow rate enhances the heat transfer between the shaft and the coolant flow. In relation to the imposed flow rate, due to the rotation an increase in the convective heat transfer coefficient can additionally be observed.

4.4.3 Non-dimensionalise the HTC Results into an Equation

Based on the experimental results obtained, an equation (4-11) is proposed to describe the Nusselt number in a steady state based on both the axial and the rotational Reynolds numbers. This is because the convective exchanges on the internal wall of the shaft are determined by the axial and the rotation flow. The exponent of Prandtl number is 0.4 for the heating of the fluid.

$$Nu = ARe^{B}Pr^{0.4} + CRe_r^{D}Pr^{0.4} \quad (4\text{-}11)$$

From the least square method, with an average relative uncertainly of lower than 10%, and the range of 0 < Re_r< 16890 (0 to 4500 rpm) and 3521 < Re < 10563 (2 L/min to 7 L/min), the values for A, B, C, D are derived and listed in Table 4-3. This equation can be applied in a number of flow channel geometrical dimensions, as well as at various axial flow rates and rotating speeds. This allows thermal designers to use these parameters to gain an accurate understanding of the thermal model rather than opt for a test trial.

Table 4-3. Coefficient for correlation.

Coefficient	A	B	C	D
Value	7.438E-03	0.9082	1.3889E-04	1.289

4.5 A Case study

An induction motor based on an equivalent to Tesla S 60 traction motor design [96] is used to verity the benefits of water-cooled shaft cooling on machine's thermal

performance. It is because that the rotor cage of induction motor often suffers overheating due to high copper loss and poor heat dissipation. Fig. 4-12 and Table 4-4 show the radial view and parameters of this induction motor, respectively.

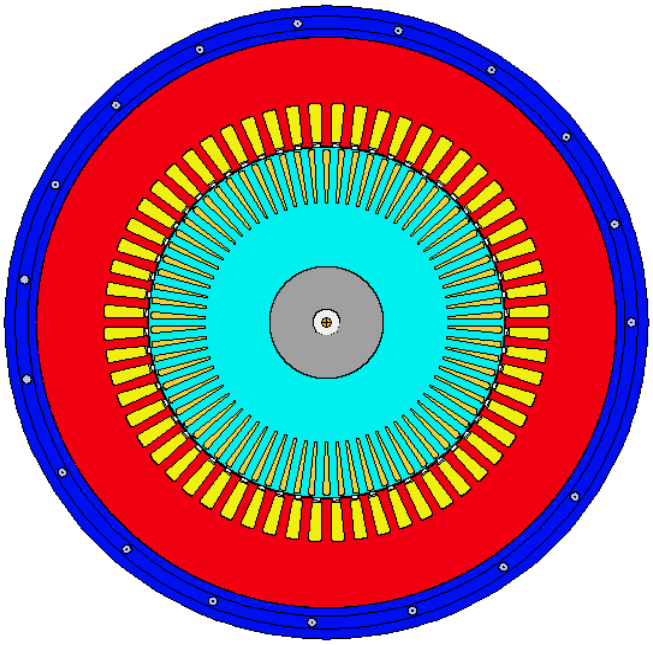

Fig. 4-12. Induction motor design for automotive traction motor.

Table 4-4. Induction motor details.

Parameter	Unit	Value
Stator OD	mm	254
Stator ID	mm	157
Airgap	mm	0.5
Slots	/	60
Poles	/	4
Electric steel	/	M250-35A
Rotor cage	/	Copper

In order to highlight the benefits of hollow-shaft rotor cooling and its dynamic effects resulting from rotation, three different models were used to calculate the temperature distribution with and without hollow-shaft cooling, respectively.

- Housing water jacket cooling;
- Housing water jacket + hollow-shaft cooling without considering rotational effects;

- Housing water jacket + hollow-shaft cooling with considering rotational effects.

Fig. 4-13 (A) shows the axial review of induction motor with housing water jacket cooling with the 6.5 L/min volume flow rate at 65 °C inlet temperature. In addition, the combined housing water jacket and hollow-shaft cooling system are illustrated in Fig. 4-13 (B), where the water with the 5 L/min flow rate is forced to pass through the hole of the shaft to cool down the copper rotor cage. The dimensionless correlation from (4-11) was used to calculate the convective HTC of hollow-shaft cooling when the rotational effects were taken into account. On another hand, in order to highlight the rotating effects, the HTC from static test was also used for hollow-shaft cooling when rotational effects were not considered. The coupled electromagnetic and thermal analysis is processed by Motor-CAD [135] to find out the improvement of temperature distribution after optimizing the thermal management.

The average temperature of rotor cage and stator windings are compared in Fig. 4-14 and Fig. 4-15. It can be noted that the water-cooled hollow-shaft cooling system can cause a significant decrease in the rotor temperature and a slight drop of winding. The rotor temperature continues to drop across the operating speeds when the rotational effects are taken place as compared to using the HTC from static test.

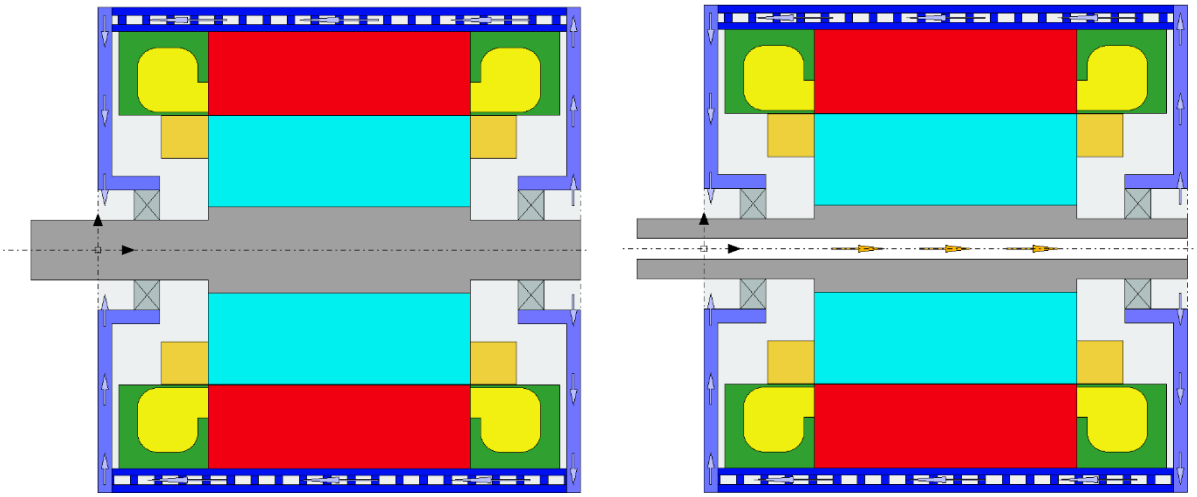

(A) (B)

Fig. 4-13. (A) Housing water jacket cooling, (B) Housing water jacket + hollow-shaft cooling.

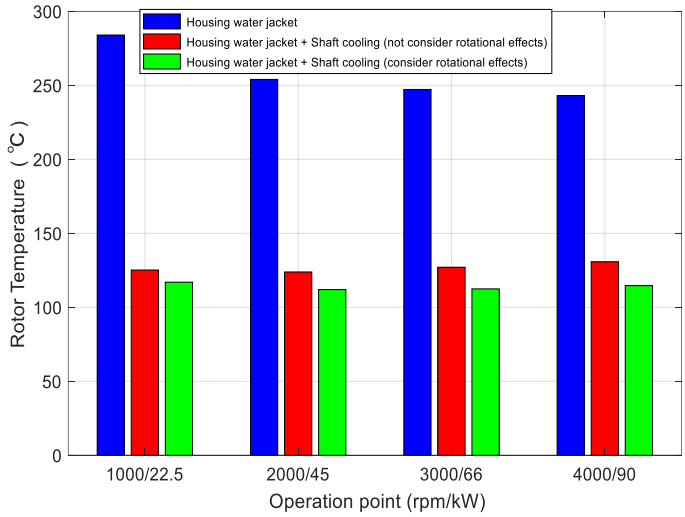

Fig. 4-14. Rotor temperature for various operating points

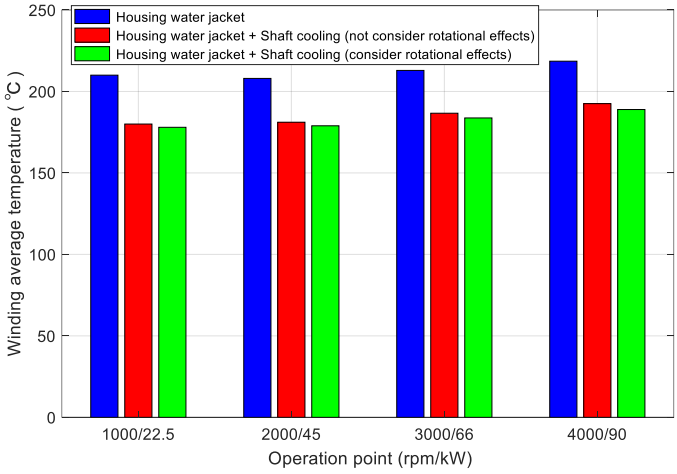

Fig. 4-15. Winding temperature for various operating points.

4.6 Summary

In this chapter, the HTC of the hollow-shaft rotor cooling for a traction motor is addressed and is applicable in relation to an axial Reynolds number ranging from 3521 to 10563 (2 L/min to 7 L/min) and a rotational Reynolds number varying between 0 and 16890 (0 to 4500 rpm). The Prandtl number of water is 7 at inlet temperature of 20 °C. Several turbulent flow models are developed in order to give a better understanding of the rotating effect on the flow and to evaluate the convective coefficient. It is concluded that the RST model provides a smaller relative error than the Realizable k-ε and SST k-ω models. The eddy viscosity model based on Boussinesq approximations is less accurate than directly calculating the parameters of the specific Reynolds stress

tensors. However, the computational cost of eddy viscosity models is less demanding than a second order closure scheme. The LPTN model is posited to help obtain a number of experimental values that are hard to measure. Through a series of CFD calculations and experiments, it is concluded that the rotational speed of the shaft can significantly enhance the convective HTC of a hollow-shaft cooling system. At the axial flow rate 2.5 L/min, the HTC for the rotational speed 4500 rpm is about 3.8 times the HTC as compared with the stationary case. This is explained that a destabilizing effect is generated by wall rotation due to the increase in the shear stresses. As a result, heat exchanges are thus promoted.

5 Thermal Analysis of a High Speed Oil-Cooled Hollow-Shaft Rotor Cooling System

The flow reference in the first test is water, and since the axial Reynolds number is greater than 4000, such axial flow is considered turbulent. However, the results may not be valid for a laminar flow where the axial Reynolds number is less than 3000. Moreover, the hollow shaft prototype used in Chapter 4 is a simple pipe, which is mainly used for research purposes to discover the effect of rotation on the flow pattern. Such simplified pipe is difficult to be employed in real traction motors. More importantly, the rotating speeds investigated in Chapter 4 are very low. These low speeds can also produce results that provide high rotational Reynolds numbers, but given that high speed applications are important here, it is difficult to apply the results of low-speed cases to high-speed cases without further experiments. As a result, the effects of high rotational speeds on HTC remain unclear. On this basis, in order to evaluate the effect of high rotational speeds on heat exchange, a new test rig was established, which uses suitable shaft geometry and can spin up to 30,000 rpm. As a result, the coolant in this case is hydraulic oil that is widely using in electric vehicles, and axial flow is regarded as laminar flow.

5.1 Structure Design

A schematic section view of the rig is shown in Fig. 5-1. The shaft is supported by two spindle ball bearings, where the bearings are adapted to the housing to cancel the high speed vibration. Then a uniform magnetic field perpendicular to the shaft axis is created by supplying the Direct Current (DC) in the coils. As a consequence, the iron loss, which is the main heat source, is generated in the magnetic shaft when the shaft is driven to rotate by a motor. At the same time, the shaft is cooled by the direct oil passing through the hole. In order to prevent the oil leakages, the low friction rotary shaft seals are installed at the ends of the shaft.

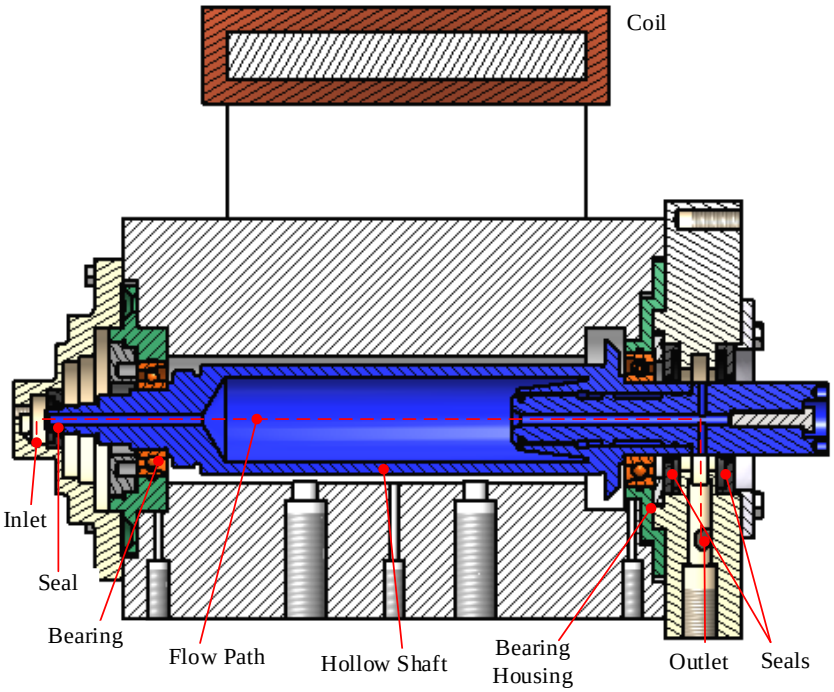

Fig. 5-1. A section view of the test rig.

In relation to this test rig, three particular advantages can be duly noted: First, the amount of the iron loss generated in the shaft is easy to control and measure at the test stage. Secondly, any high temperature that commonly arises from there being a stator does not occur here. The reason for this is because the pole temperature is only just over room temperature, which itself is due to the thermal insulation paper underneath the coil stopping the heat transfer. Finally, using this rig the shaft surface temperature can be recorded directly and more accurately, which obviates the need for having to resort to measuring each end of the rotor and in the process providing less precise readings.

5.2 Power Losses Calculation

An accurate evaluation of the amount of heat loss and its distribution is a prerequisite of a proper thermal analysis. The major losses in the rig can be divided into the following: electrical, friction and flow dynamic types. The electrical losses are calculated by the time-stepping two-dimensional Finite Element Analysis (FEA) using JMAG, but windage and bearing friction losses are calculated by using the analytical methods. The friction losses caused by the flow and the seals do not act as an internal heat source but are dissipated into the flow directly. These losses from the flow and

the seals constitute the majority of overall friction losses and will be identified at the test stage.

5.2.1 Electrical Losses

The iron loss is the majority of losses generated in the shaft and depends on the strength of the magnetic field as well as the rotating speeds. The iron loss P_{iron} in this solid shaft structure is calculated by integrating the current loss density over the volume of the region using following equation:

$$P_{iron} = \int_V J \cdot E \tag{5-1}$$

Where J is the current density, and E is the electrical field.

The iron loss density mainly comes from the distortion of the flux line on the shaft surface. Hence the calculation accuracy can be increased by taking into account the skin effect. In addition, the calculation time must be small enough to capture the frequency of the eddy current development. As a result, the size of the shaft mesh is set at 1 mm with a 1.5 mm skin depth across all 5 divisions. As an example, the eddy current loss distribution at 5,000 rpm is shown in Fig. 5-2.

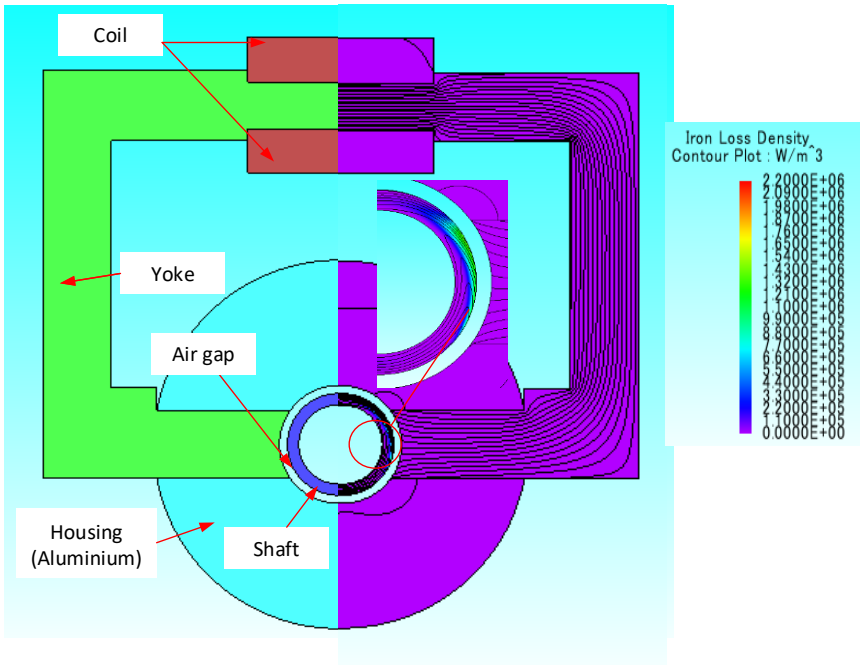

Fig. 5-2. Iron loss distribution in the shaft at t = 50ms.

While the shaft operates at various rotational speeds and input currents, the FEA-predicted variations of iron loss are shown in Fig. 5-3. The plots on the graph below

show that the value of the loss increases with the rise in the rotational speed and in the input current. To explain the boosting effects two phenomena can be addressed: Firstly, the increase in the speed enhances the distortion frequency of the magnetic field in and around the shaft (see Fig. 5-4). Secondly, the rise of the input current boosts the uniform magnetic flux density. As a consequence, the current density in the shaft rises due to these effects. In addition, the effect of shaft temperature on the loss calculation is considered based on the resistivity variation. The resistivity of shaft increases with the shaft temperature rise. This causes lower iron loss in the shaft at higher temperatures than at lower temperatures. It must be noted that, when using this method, the amount of the iron loss in the shaft is easy to control and measure at the test stage.

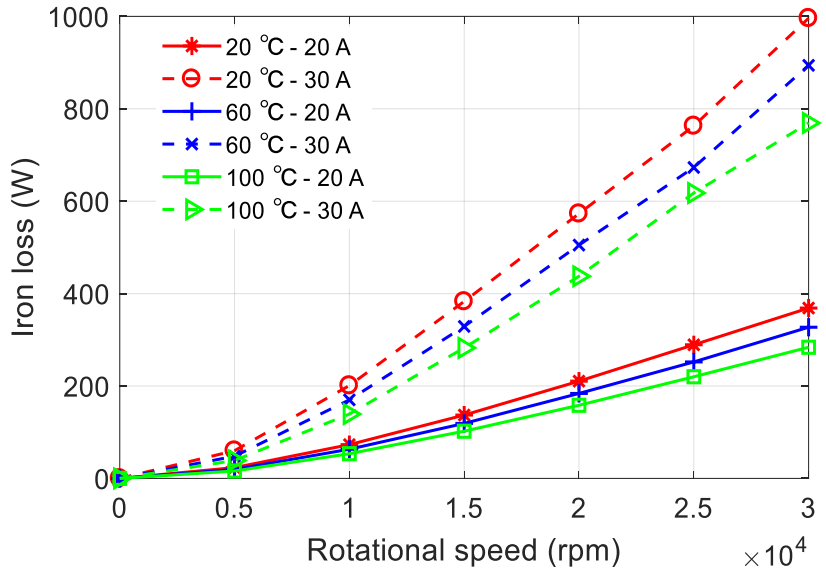

Fig. 5-3. Iron loss curves versus the rotational speed and the input current.

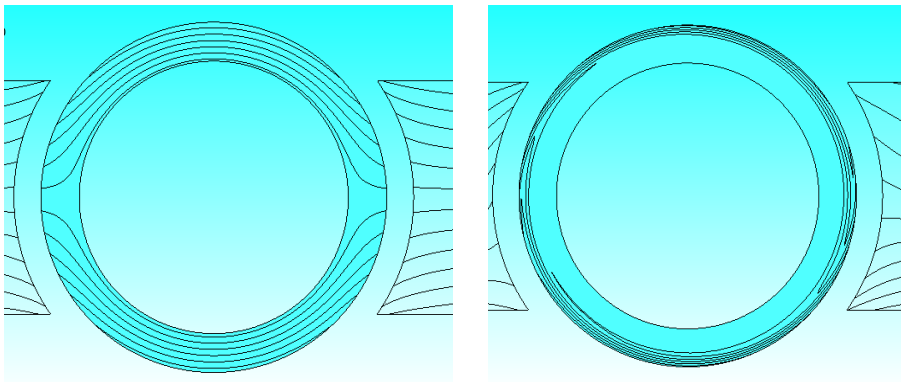

(a) 0 rpm (b) 30,000 rpm

Fig. 5-4. Magnetic flux density.

5.2.2 Air Friction Loss

The air friction losses can be generated by the tangential velocity from a rotational cylinder in the air gap. The value of this loss is dependent on the rotational speed of the shaft and this should not be negligible at high rotating speeds. The following equation [138] is used to calculate the friction loss.

$$P = \varphi C_f \pi \rho \omega^3 {r_{outer}}^4 l \tag{5-2}$$

where ρ is the air density; ω, l and r_{outer} are the angular speed, length and radius of the shaft respectively; φ is the roughness coefficient; C_f is the air friction coefficient, which depends upon the air gap structure and surface condition of the shaft – and this air friction coefficient can be expressed as (5-3) and (5-4). In order to better understand C_f, the Couette–Reynolds number Re_δ [139] is introduced to describe the nature of tangential gas flow inside the air gap. The definition of Re_δ is described as (5-5), which takes into account the effect of the enclosure by including the radial air-gap length.

$$C_f = 0.515 \frac{(\delta / r_{outer})^{0.3}}{Re_\delta^{0.5}}, 500 < Re_\delta < 10^4 \tag{5-3}$$

$$C_f = 0.0325 \frac{(\delta / r)^{0.3}}{Re_\delta^{0.2}}, Re_\delta > 10^4 \tag{5-4}$$

$$Re_\delta = \rho \omega r \delta / \mu \tag{5-5}$$

where μ is the air dynamic viscosity; δ is the radial air-gap length.

The friction losses of the shaft surface at different speeds and air temperature are shown in Fig. 5-5. The roughness coefficient is taken as 1.0 for smooth surfaces. It can be concluded that the air friction losses increases with the rotating speed. But the rise in air temperature has the effect of slightly decreasing the friction loss.

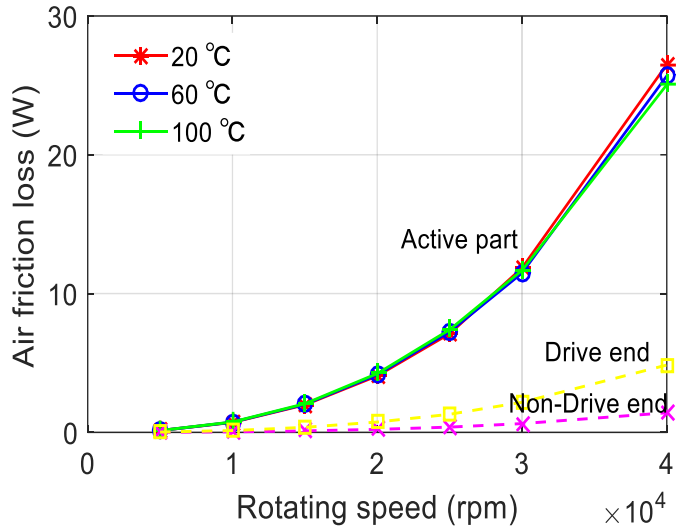

Fig. 5-5. Air-friction losses on the rotor surface and end face.

5.2.3 Bearing Losses

The resistance to rotation of a rolling bearing is composed of three kinds of friction: rolling, sliding and lubricant types. The specification data of the bearing manufacturer (*FAG*) are used to calculate the friction torque of various rotational speeds to estimate the bearing losses. According to the detailed model provided by the Schaeffler Bearinx®-online “Easy Friction” software [140], the friction values are set out in Fig. 5-6. This procedure takes account of the effects of the internal load distribution on the contact pressures generated by the raceways and ribs.

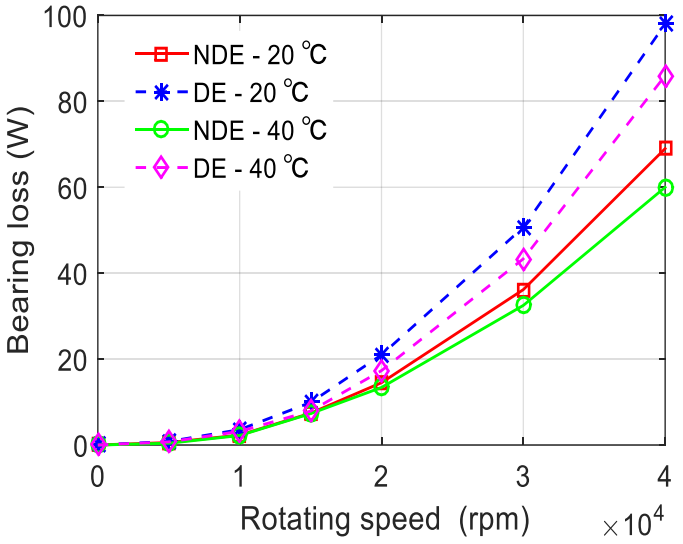

Fig. 5-6. Bearing losses at various working temperatures.

The resistance of a rolling bearing is proportional to the rotating speed. It should be observed that the drive end (DE) generates more friction loss than the non-drive end (NDE). This is due to the external loads that are created in the DE. However, the friction losses fall when the working temperature is increased. This is because an increased temperature in the lubricant leads to a decrease in the viscosity of the latter. This viscosity drop leads to the decrease in the cohesive forces of the molecules and causes a lower shear stress during the rotation of the shaft.

5.3 Thermal Modelling of Test Rig

In this simulation analysis, various losses that are explained in Section 5.2 are regarded as the heat source and these are eventually converted into a rise in temperature. The heat source and boundary conditions of this thermal model are displayed in Fig. 5-7. In the diagram, the air friction loss causes the heat flow on the shaft surface. Moreover, the iron and bearing losses take place in the shaft and bearing respectively. In order to simplify the computation process while still achieving a high degree of accuracy, the following assumptions are made in the modelling of the rig.

- The heat dissipated from the shaft is mainly through convection to the oil and air, with the other main cooling path being through conduction to the housing.
- The bearing is modelled as a unit. The only heat transfer is through the conduction to the housing.
- The housing outer surface temperature is set at room temperature.
- The initial temperature of the shaft is set at the same level as inlet oil temperature.
- A steady state analysis is used to obtain the temperature distribution in a steady state in addition to the elevated temperature process.

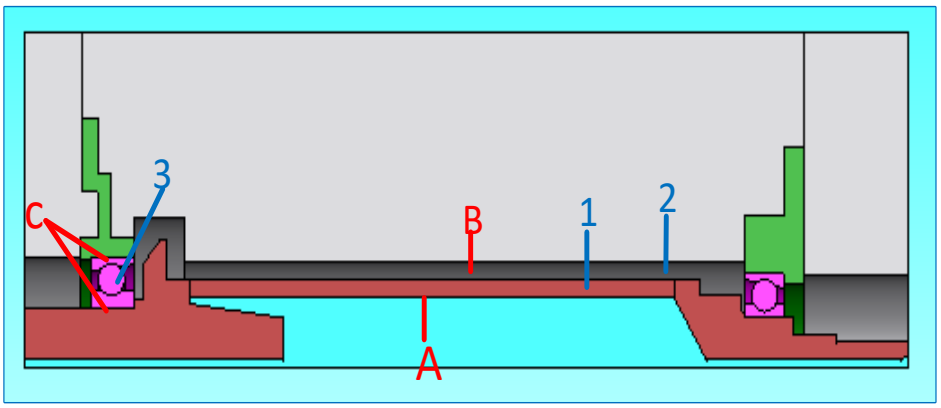

Fig. 5-7. The FEA thermal model has the following thermal loads: 1) Iron loss; 2) Air friction loss; 3) Bearing friction loss. And boundary conditions: A) Forced oil convection; B) Air convection; C) Contact thermal resistance.

5.3.1 Predicting the HTC by means of CFD

A three dimensional (3-D) CFD model was developed to predict the HTC of the hollow-shaft inner wall surface, as shown in Fig. 5-8. The grey areas in this diagram stand for the solid region of the hollow-shaft, for which only the heat equation needs to be calculated. Whereas for the fluid regions (as represented by the green domain) also the mass transport equation needs to be considered. As for the properties of the coolant and the shaft in the CFD model, Hydraulic oil (Shell Tellus S2 M22) and EN43 steel are used to represent them respectively. Table 5-1 and Table 5-2 show the variations in the nature of the fluid and the solid properties respectively depending on the temperatures involved.

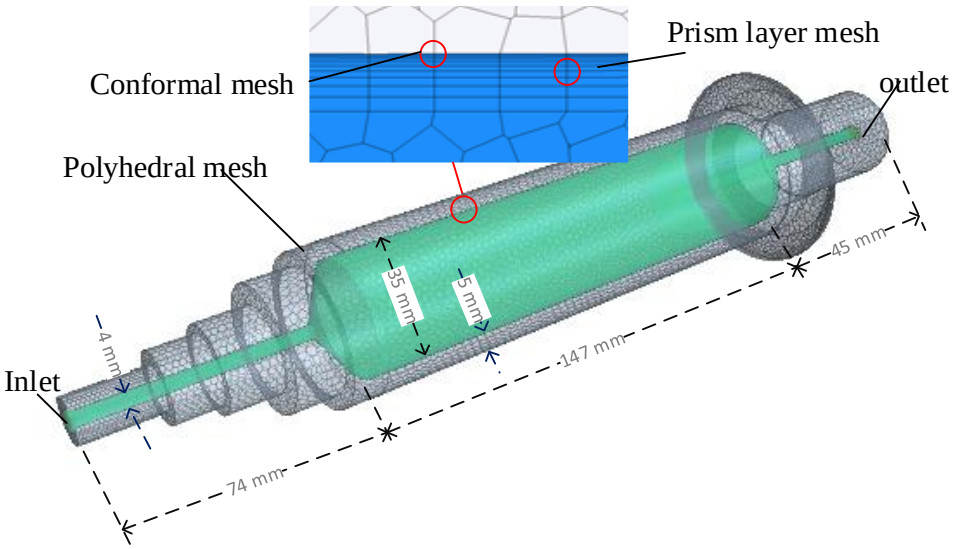

Fig. 5-8. Mesh of the hollow-shaft in 3-D CFD.

Table 5-1. Variation of coolant properties as per temperature T.

Density, ρ $(\mathrm{kg/m^3})$	$\rho = 1e^{-7}T^2 - 0.0006T + 0.8755$
Dynamic viscosity, μ (Pa.s)	$\mu = 141.58e^{-0.037T}$
Specific heat capacity, c_p (kJ/(kg·K))	$c = 2e^{-15}\,T^2 + 4.3533T + 757.4$
Thermal conductivity λ, (W/(m·K))	$\lambda = 3e^{-9}\,T^2 - 2e^{-5}\;T + 0.1256$

Table 5-2. Variation of the shaft properties as per temperature T.

Specific heat capacity, c_p (kJ/(kg·K))	$\mathrm{c} = 2.2\mathrm{e}^{-6}\,\mathrm{T}^3 - 1.7\mathrm{e}^{-3}\,\mathrm{T}^2 + 7.7\mathrm{e}^{-1}\,\mathrm{T} + 470$
Thermal conductivity λ, (W/(m·K))	$\lambda = -3.33\mathrm{e}^{-2}\,\mathrm{T} + 52$

The 3-D mesh was put together using many polyhedral elements with a mesh size set at 2 mm. In addition, the conformal mesh was employed to make sure that the perimeter of cell faces on the surface of one part, match up exactly with the coincident cell faces on a part in contact with it. Furthermore, the boundary prism layer mesh was used to add the prismatic cell layers next to wall boundaries to capture velocity and thermal boundary layers at the wall. The mesh is effective in heat transfer and swirling flow situations and this results in greater simulation accuracy. A grid sensitivity analysis was performed using the final mesh resulting in a total of 0.5 million elements.

The turbulent models, boundary condition, wall treatment and moving reference frame setup used in Chapter 3 were also employed for the present study.

5.3.2 Air Gap Heat Transfer Coefficient

The flow in a smooth annular gap subjected to inner cylinder rotation alone is known as Taylor-Couette flow. A modified Taylor number Ta [141] is defined as (5-6) by introducing the geometrical factor F_g, which takes into account the corresponding air-gap length and shaft radius.

$$Ta = \frac{\omega^2 \delta^3 r_{outer}}{\upsilon^2} \cdot \frac{1}{F_g} \tag{5-6}$$

where F_g is

$$F_g = \frac{\pi^4 (2r_{outer} + \delta)}{3394 r_{outer} (0.0571\left(1 - 0.652\frac{\delta}{r_{outer}}\right) + 0.00056\left(1 - 0.652\frac{\delta}{r_{outer}}\right)^{-1})} \tag{5-7}$$

The Nusselt number for the air gap is expressed as (5-8) based on the Taylor number [141].

$$Nu = \begin{pmatrix} 2, Ta < 1700 \\ 0.128\, Ta^{0.367}, 1700 < Ta < 10^4, \\ 0.409\, Ta^{0.241}, 10^4 < Ta < 10^7 \end{pmatrix} \tag{5-8}$$

The air gap convection HTC is evaluated by applying (2-1).

Then the variation of the convective HTC of the designed shaft as a function of speed and temperature is plotted in Fig. 5-9. Similar to the air friction loss, the tangential speed boosts the value of HTC. However, the temperature has a slightly decreasing effect on HTC.

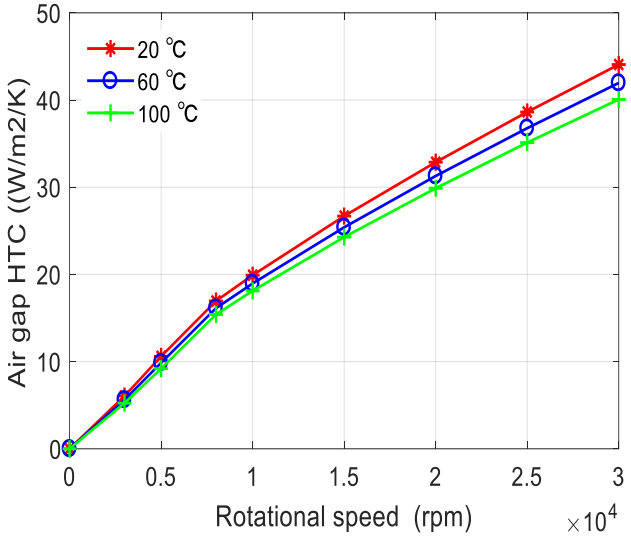

Fig. 5-9. Air gap convective heat transfer coefficient.

5.3.3 Contact Resistance

Although an interface fit is implemented for the bearing assembly, the interface gaps still exist between components due to the imperfections in the surfaces that touch each other as well as in the material hardness. The average air gap δ_f between fitted bodies, defined as (5-9), depends on temperatures of the components and also on initial interface clearance δ_i [142].

$$\delta_f = \delta_i - \left|T_{ring} - T_{shaft/housing}\right| * \beta r_{outer} \tag{5-9}$$

Where β is the linear thermal expansion coefficient, r_{outer} is the radius of shaft / housing, T_{ring} and $T_{shaft/housing}$ are the temperature of bearing and shaft / housing,

respectively. The thermal contact resistances between the bearing rings and the housing / shaft based on an average interference air gap are calculated by (5-10) [142].

$$R = \frac{\delta_f \lambda_{ring} + L_{ring}\lambda_{air}}{A\lambda_{ring}\lambda_{air}} \tag{5-10}$$

where A is the contact surface area; λ_{air} and λ_{ring} are the conductivity of air and the bearing rings, respectively; and L_{ring} is the ring thickness.

Fig. 5-10 and Fig. 5-11 show the thermal contact resistances for the test rig as a function of the radial clearance and temperature difference, respectively. It should be noted that the resistance increases as the radial clearance rises from zero. When the bearing and the shaft or housing have the same temperature, there is maximum thermal contact resistance through the air gap based on the initial clearance. However, while the bearing ring becomes warmer relative to the housing or shaft, the temperature difference causes a reduction of the radial air gap and a drop in the level of resistance.

In this thermal model, the temperatures of the shaft, housing and bearings are selected based on the test results. In addition, an initial clearance of 12 μm is chosen [143].

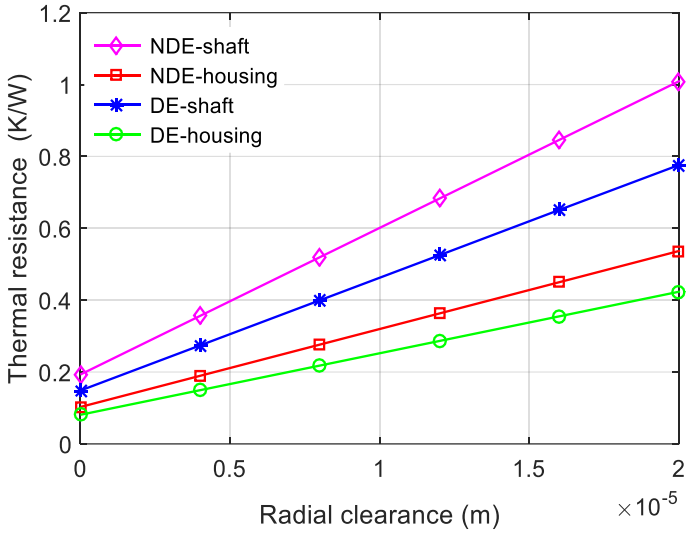

Fig. 5-10. Thermal resistance between the bearing rings and the shaft/housing as a function of the radial clearance.

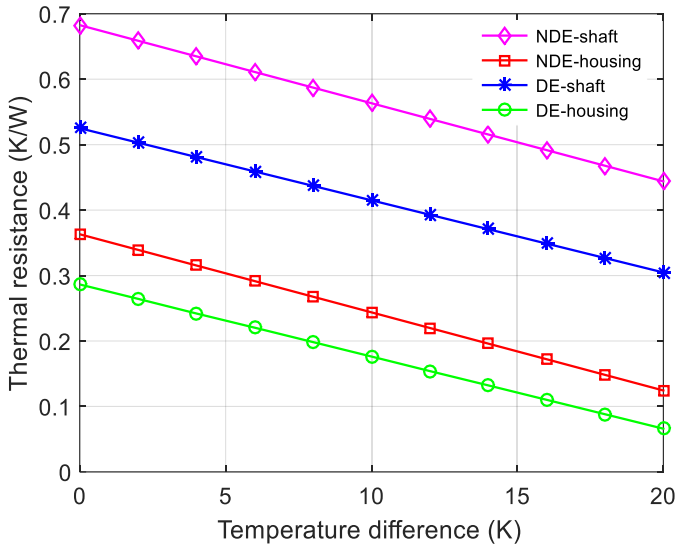

Fig. 5-11. Thermal resistance between the bearing rings and the shaft/housing as a function of the temperature difference at an initial clearance of 12 μm.

5.4 Summary

In this chapter, various losses, which consist of iron, air friction and bearing losses are identified across a range of operation speeds. Then, a simplified numerical model based on computational fluid dynamics methods is developed to provide a qualitative understanding of the mechanism of oil convective heat transfer. In addition, the air gap HTC and contact resistance between fitted bodies are calculated using the analytical methods. On these basis, a finite element model is constructed to estimate the heat path by considering the heat dissipations of conduction and convection.

6 Experimental Investigation of a High Speed Oil-Cooled Hollow-Shaft Rotor Cooling System

In order to validate the simulation analysis in Chapter 5, this chapter implements experimental tests accordingly. A detailed description of the experimental mechanisms, measurement techniques and calibrations using uncertainty analysis are provided. Then a discussion of the impact parameters on the thermal performance of this cooling method is offered.

6.1 Setup

Fig. 6-1 shows a schematic diagram of the experimental setup. It consists of a closed loop of the oil traveling along a pipe, where the oil is pumped and recirculated from a container into the test rig by passing through a heat exchanger. The function of the heat exchange is to keep the oil temperature constant by absorbing or dissipating heat from the water. The water temperature is set at a constant value by a water heater that consists of a heater function, a refrigerator and a temperature controller. The oil that flows through the shaft is regulated using a globe valve and measured using a flow meter.

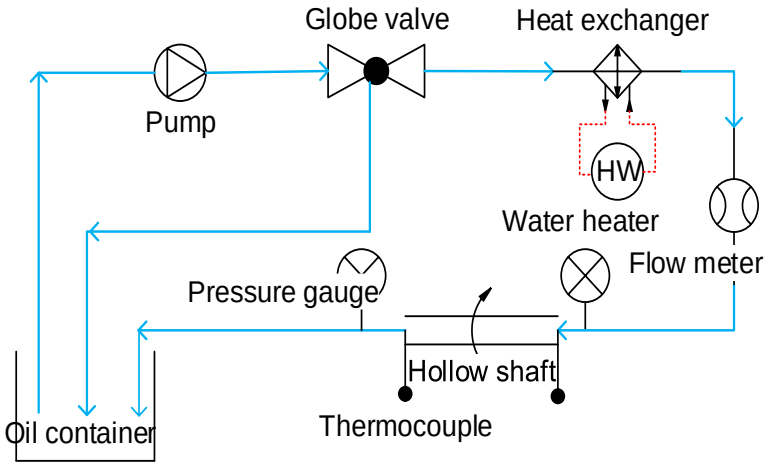

Fig. 6-1. Test setup.

Fig. 6-2 presents the experimental test rig, where the hollow-shaft is rotated by an electric motor using a pulley to accelerate the shaft up to 30,000 rpm. A torque transducer is placed between the motor and shaft with the aim of capturing the torque.

Two high-speed flexible couplings are used to connect the torque transducer together with ends of the shaft and motor. The experiments were repeated for various coolant flow rates, inlet temperatures, shaft rotating speeds and input heat losses, as shown in Table 6-1. Each experiment was run until the equilibrium conditions were established.

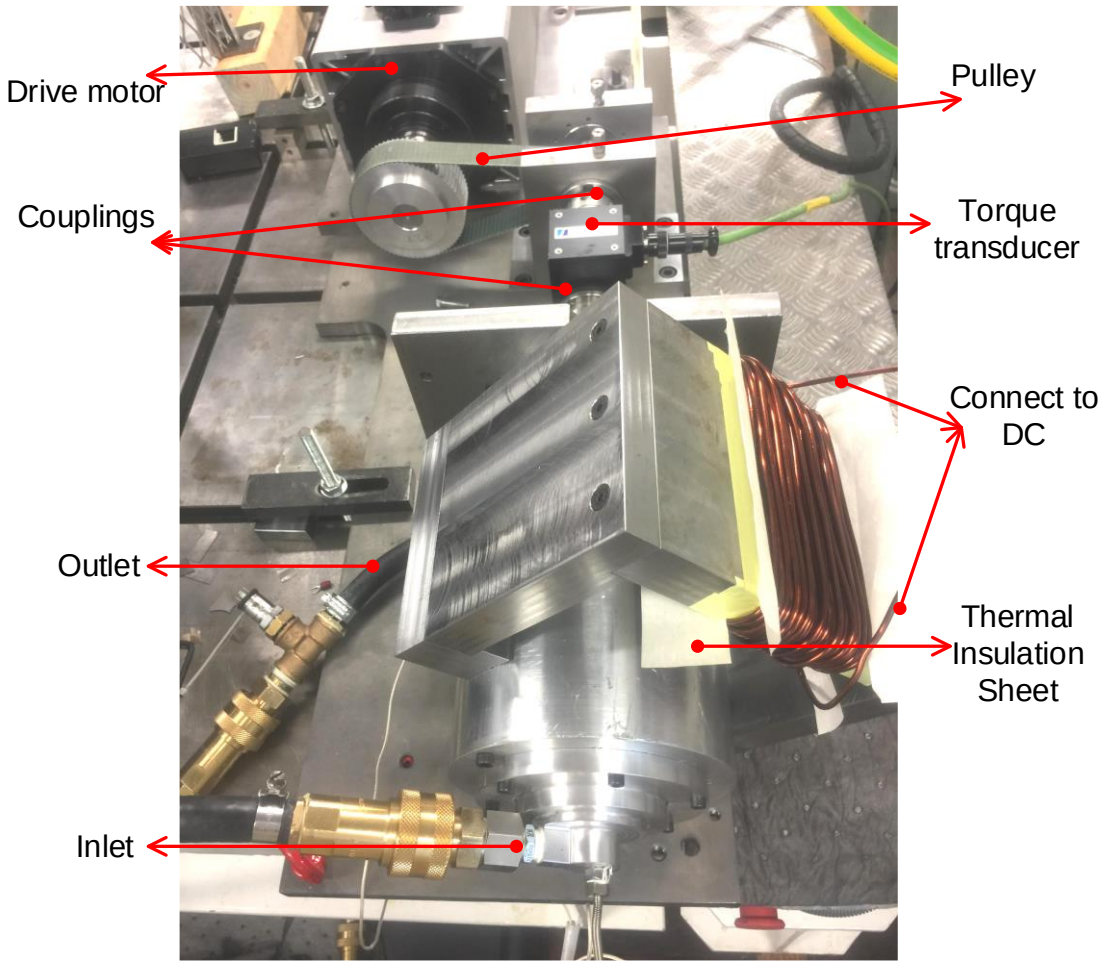

Fig. 6-2. Experimental test rig.

Table 6-1. Experiment details.

Coolant inlet temperature (℃)	Flow rates (L/min)	Shaft rotating speed (rpm)	Heat input (W)
22, 42, 60	3-7	5000, 10,000, 15,000, 20,000, 25,000, 30,000	245, 400, 611, 800, 1030

6.2 Measurement

6.2.1 Temperature Measurement

Two four-wire Pt100 sensors with an accuracy of ± 0.05 ˚C are mounted in the housings to measure the inlet and outlet coolant temperatures. The shaft surface temperature is measured by a subminiature noncontact infrared thermometer. In practice, due to the partial transmission through the surrounding air, the signal received by the sensor can be attenuated. Moreover, the infrared signal might capture the radiation in the environment which is reflected onto the shaft. On this basis, and to improve the radiative heat flux emitted purely by the cylinder, the latter is painted black to achieve a maximal emissivity of 0.94 ± 0.01, as determined by calibration (Shown in Fig. 6-3). In addition, the temperature of the bearing, the air gap, the pole and the coil taken as indicators, are measured using the K type thermocouples. The locations of these thermocouples are summarized in Fig. 6-4.

Fig. 6-3. Painted shaft.

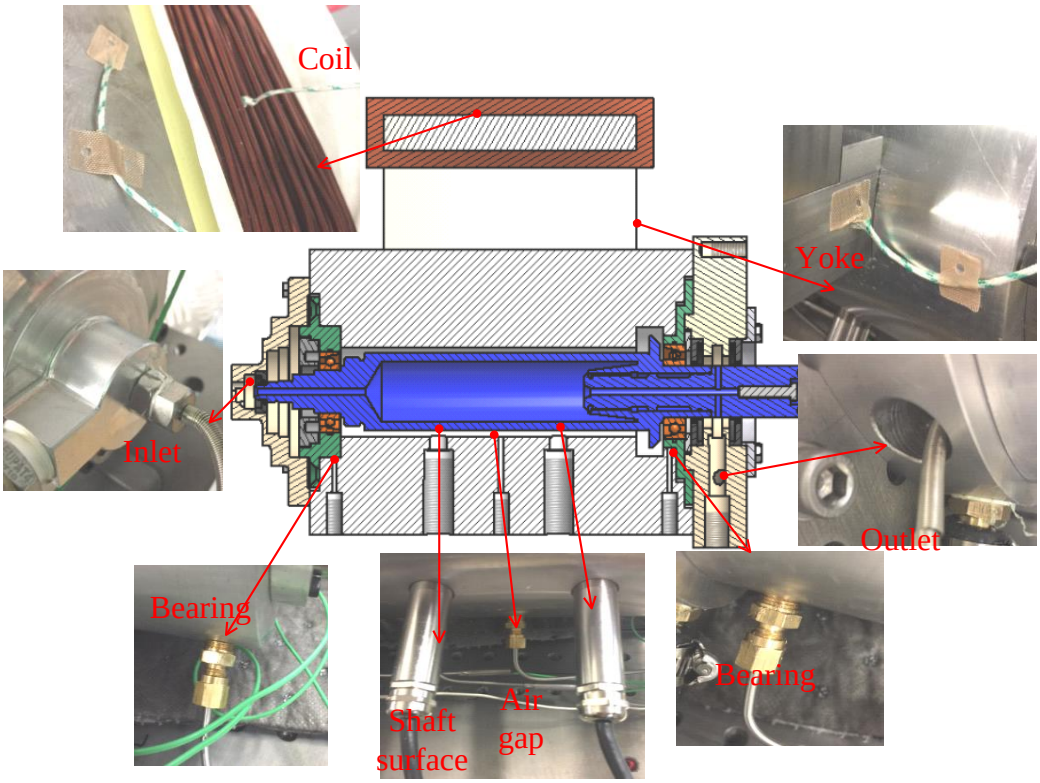

Fig. 6-4. Temperature sensor locations.

6.2.2 Losses Measurement

A torque transducer is placed between the motor and shaft for measuring the torque of the shaft. For the rotating motion, the power P_{Mech} is the product of the torque τ and the angular velocity ω, as defined in (6-1).

$$P_{Mech} = \omega * \tau \tag{6-1}$$

The relationship between the mechanical power and the heat loss caused by the shaft rotating in the magnetic field can be expressed as follows:

$$P_{Mech} = P_M + P_E \tag{6-2}$$

$$P_M = P_{F\_B} + P_{F\_A} + P_{F\_S} + P_{F\_D} \tag{6-3}$$

$$P_E = P_{E\_P} + P_{E\_S} \tag{6-4}$$

where P_M is the mechanical losses, which include the bearing friction loss P_{F_B}, the air friction loss P_{F_A}, the seal friction loss P_{F_S} and the fluid dynamic loss P_{F_D}. P_E is the electrical losses, which consist of two main parts, the pole iron loss P_{E_P} and the shaft

iron loss P_{E_S}. Due to the small amount of current and the stationary of stator pole, the pole loss is not taken into account.

Two different steps were taken to calculate the loss by recording the data from the torque meter with the DC off and on, respectively, and from (6-1).

- Rotating the shaft with the DC off: P_1 is the mechanical losses (P_M) which consist of air friction, bearing friction, seal friction and flow dynamic losses.
- Rotating the shaft with the DC on: P_2 is the mechanical losses in addition to the shaft iron loss. Therefore, $(P_2 - P_1)$ is taken as the shaft iron loss (P_{E_S}) generated in the shaft.

6.3 Calibration

6.3.1 Calibration of the Temperature Sensors

The calibration of subminiature noncontact infrared thermometer and K-type thermocouples were measured against a reference OMEGA Surface Mount 4 wire Pt100 element temperature sensor with an accuracy of ± 0.07 ˚C. The test setup was mounted with thermocouples and inserted into a Carbolite oven at a range of 20 to 100 ˚C with 0.5 ˚C hysteresis. After measurement, the infrared thermometer and the thermocouple offset were at 0.71 ˚C and 0.65 ˚C, respectively.

6.3.2 Calibration of the Flow Meter

A RS pro liquid sensor was selected as being suitable for oils with a range from 1.5 L/min to 30 L/min. This sensor provides a pulsed output proportional to the flow rate. The relation of frequency f (pulses per second) vs flow rates Q (liters per minute) is provided in (6-5), where k is the conversion ratio, which may be different for various coolant viscosities and densities. A recalibration process to account for the density and viscosity of the cooling oil is required. The calibration by weight method [144] was employed by using the setup shown in Fig. 6-5.

$$Q = f/k \tag{6-5}$$

The flow meter calibration data are plotted in terms of k versus f/υ as shown in Fig. 6-6. This single curve can then be used to predict the performance of the flow meter with a high degree of accuracy under all conditions within the calibration viscosity range.

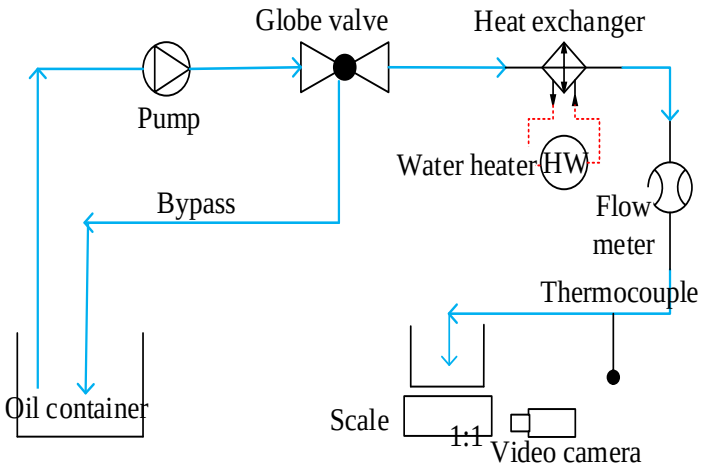

Fig. 6-5. Schematic outline showing the flow meter calibration by mass.

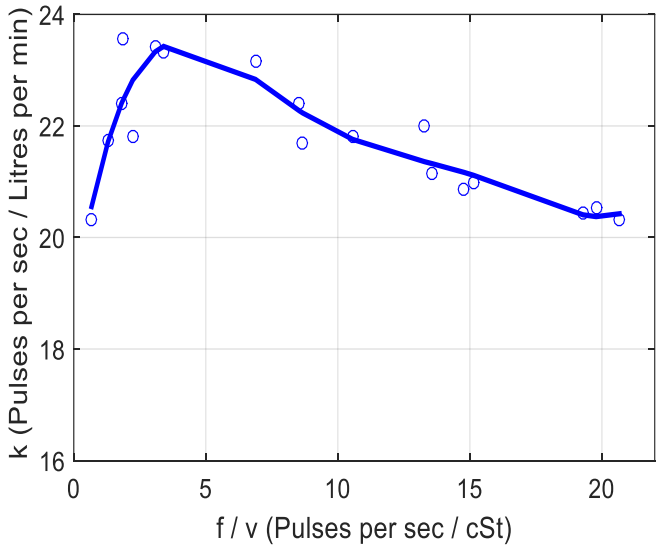

Fig. 6-6. The flow meter calibration curve.

6.3.3 Calibration of the Torque Transducer

Magtrol's In-Line torque transducer with a 2 Nm range was selected for measuring the torque of the shaft. The method of calibrating the torque transducer was to drive the shaft to spin in clockwise and anti-clockwise directions in the same manner. The results of these two directions can be called τ_c and τ_a, respectively. The offset can be obtained by using (6-6). Finally, the average offset of the torque transducer was 0.0073 Nm at low rotating speeds (below 10,000 rpm) and 0.0046 Nm at high rotating speeds.

$$\tau_o = (\tau_c + \tau_a)/2 \tag{6-6}$$

6.3.4 Uncertainty Analysis

The temperature sensor uncertainty $u(T)$ is calculated using the following equation:

$$u(T) = \sqrt{[u(T_r)]^2 + [u(T_o)]^2 + [u(T_h)]^2} \quad (6\text{-}7)$$

Where $u(T_r)$ is the reference temperature accuracy; $u(T_o)$ is the thermocouple offset; and $u(T_h)$ is the oven hysteresis. The temperature uncertainty for the infrared thermometer and the thermocouple were at 0.89 ˚C and 0.91 ˚C respectively.

The timer has an uncertainty $u(Q_t)$ of 0.2 % ($\pm$ 0.5 s) for the range from 120 s to 360 s. The weigh scale resolution of 0.02 kg leads to an uncertainty $u(Q_s)$ of 0.1 % for a fully filled tank (20 kg). The uncertainty in the flow meter $u(Q_m)$ is 1.5 %. Finally, the uncertainty in the flow rate measurement $u(Q)$ is calculated using (6-8). The uncertainty of the measured flow rate is 1.516 %.

$$u(Q) = \sqrt{[u(Q_t)]^2 + [u(Q_s)]^2 + [u(Q_m)]^2} \quad (6\text{-}8)$$

The uncertainty of the torque measurement $u(P)$ can be re`presented in equation form as follows:

$$u(\tau) = \sqrt{[u(\tau_t)]^2 + [u(\tau_o)]^2} \quad (6\text{-}9)$$

where the uncertainty in the torque transducers $u(\tau_t)$ is less than 0.002 Nm, the $u(\tau_o)$ is the torque transducer offset. Finally, the uncertainty of the measured torque is 0.00757 Nm at low speeds and 0.00502 Nm at high speeds.

6.4 Derive the HTC

6.4.1 Coupled Thermal Analysis

The coupled CFD and FEA are processed as shown in Fig. 6-7. The proposed CFD and FEA models have been explained in detail in the chapter 5. The developed FEA model is used to represent the heat path taken in the test. After that the initial HTC under rotation conditions is investigated using CFD and thus this HTC is the input boundary condition. The output of the FEA model is the shaft external wall temperature. At this point, a decision is made to carry on or not depending on the outcome of a comparison with the test results. If external wall temperature of the shaft derived from the FEA model are not the same as those obtained from the experiment, then a new

iteration of the HTC is required until the difference of two results obtained between the FEA model and the experiment converge within a reasonable margin of error (±1 %). After the two sets of measurements results match, the initial estimation value is the final requirement.

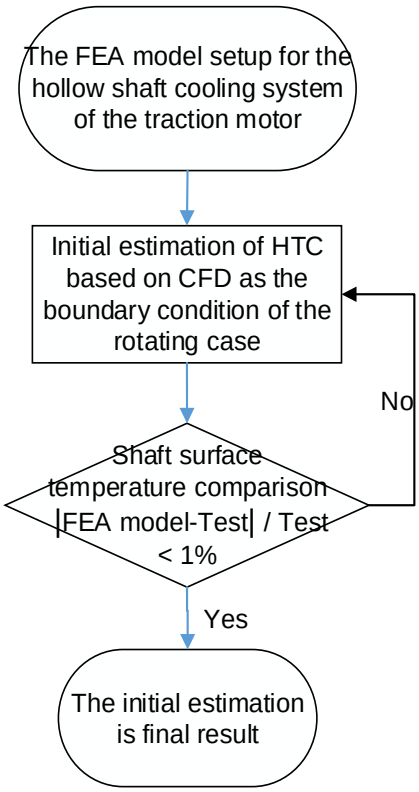

Fig. 6-7. Flow chart of the coupled thermal analysis.

6.4.2 Measurement Based on Formula

The general formula that defines the heat transfer coefficient associated with a solid wall surrounded by a fluid is defined as (3-27). Only the shaft iron losses and air fiction losses regarded as the heat source and these are eventually converted into a rise in temperature cause the shaft temperature rise. The friction losses caused by the flow and the seals do not act as an internal heat source but are dissipated into the flow directly.

The heat dissipated from the shaft is mainly through convection to the oil. But still some heat is dissipated with the other path being through conduction to the housing and through natural convection to the air. These latter two paths are difficult to measure and distinguish. In this test, the heat removed from the wall to the oil is measured from

the coolant temperature rise ΔT from T_{inlet} to T_{outlet}. Based on the energy conservation equation (4-6), the heat flux q'' from the shaft to the coolant is determined.

Two different steps were taken to calculate the mount of the iron loss dissipated by the oil with the DC off and on, respectively:

- Rotating the shaft with the DC off: the ΔT_1 is the coolant temperature rise due to the mechanical losses, mainly from the flow and the seals.
- Rotating the shaft with the DC on: the coolant temperature rise ΔT_2 is from not only the mechanical losses but also the shaft iron losses. Therefore, the net temperature rise $(\Delta T_2 - \Delta T_1)$ is caused by the iron losses removed from the shaft.

Due to high thermal conductivity and the thin of the shaft, the inner wall temperatures T_{wall} is the equal the outer wall temperature, where have been measured by infrared sensor (See Fig. 6-4). However, T_{fluid} is difficult to measure during the test and is often replaced by an alternative fluid temperature. In this study, the fluid temperature can be defined as in (3-28).

6.5 Results and Discussions

6.5.1 Power Losses

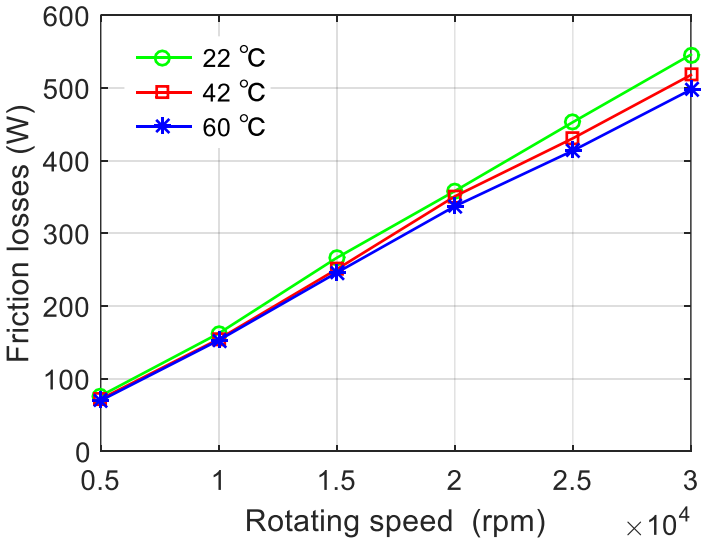

Fig. 6-8. The overall friction losses at various speeds and inlet coolant temperatures.

When the inlet flow rate is 4.2 L/min, the overall friction losses at various inlet coolant temperatures are shown in Fig. 6-8. The plots on the graph show that the rise in coolant temperature has the effect of slightly decreasing the overall friction losses. This is because an increased temperature in the air and oil leads to a decrease in the viscosity of the mediums. This viscosity drop leads to a decrease in the cohesive forces of the molecules and causes a lower shear stress during the rotation of the shaft.

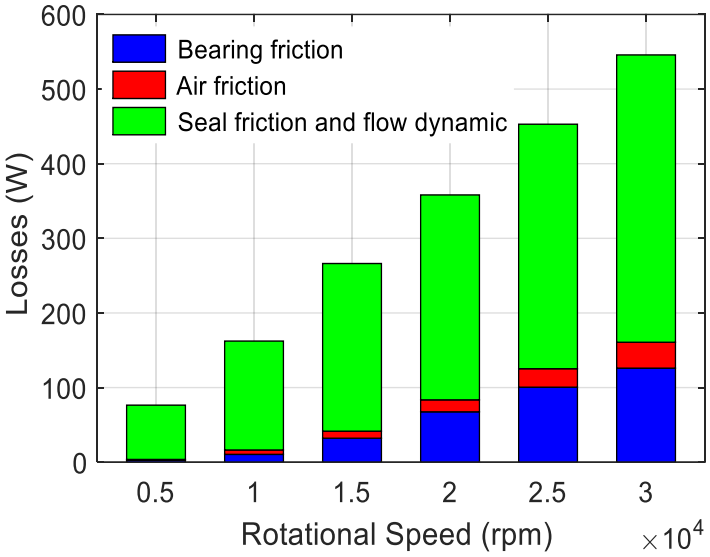

Fig. 6-9. The distributions of the friction losses.

Fig. 6-9 provides a detailed distribution of the mechanical friction losses at various rotational speeds with the temperature of the coolant at 22 ˚C and the inlet flow rate at 4.2 L/min. The air and bearing mechanical losses are calculated using the analytical methods (discussed in Chapter 5), where the shaft surface roughness coefficient is taken as 1.0 for smooth surfaces. In addition, the temperatures of the air and the bearings are selected based on the test results. Finally, the seal and flow dynamic mechanical losses can be obtained based on (6-3). It can be concluded that all the friction losses are directly proportional to the rotation speeds. These losses will rapidly rise in proportion as the speed increases. The mechanical losses caused by the seals and the flows come to more than 70 % of the total mechanical friction losses.

While the DC is on, the shaft operates at various rotational speeds and input currents. A comparison of the results obtained between the experiments and the FEA-predicted variations of iron loss is shown in Fig. 6-10. For the FEA results, the effect of temperature on the shaft resistance is taken into account. The plots on the graph show

that the value of the loss increases with the rise in the rotational speed and in the input current. To explain this two phenomena can be explained: Firstly, the increase in the speed enhances the distortion frequency of the magnetic field in and around the shaft. Secondly, the rise of the input current boosts the uniform magnetic flux density. As a consequence, the current density in the shaft rises due to these effects. The 2-D FEA simulation underestimates the iron loss. It is because that the solid soft magnetic structure steel was applied. This leads to generate extra losses in the ends of the shaft. Moreover, the effect of manufacturing on constructed shaft is not taken into account.

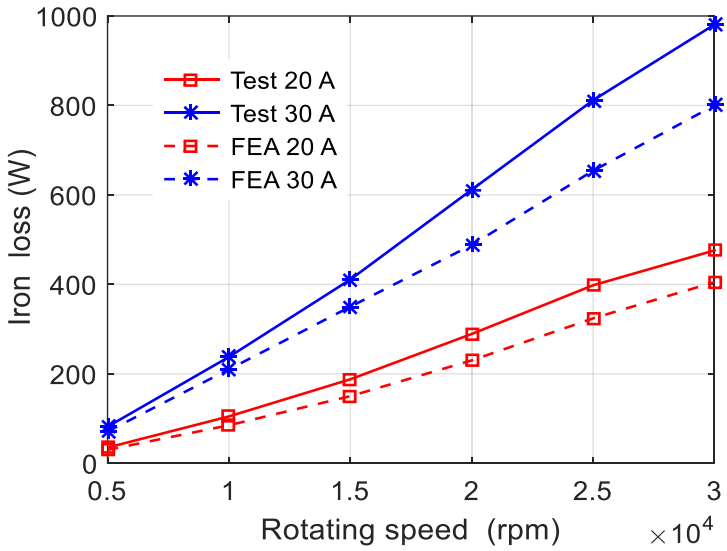

Fig. 6-10. Iron loss curves versus the rotational speed and the input current.

6.5.2 Shaft Temperature Rise and Dissipated Losses

When the inlet flow rate is 4.2 L/ min, Table 6-2 and Table 6-3 list the measured losses from (6-1), the dissipated losses from (4-6) and the shaft temperature rise from the infrared temperature sensor with DC off and on, respectively. It can be noticed that the friction losses obtained in Table 6-2 are proportional to the rotation speeds. More than 70 % of the friction losses are taken away by the oil directly. The remaining friction losses are mainly from the bearing and air. These losses are dissipated to the housing by conduction or to the air by nature convection. More important, the friction losses have less impact on the shaft temperature rise. The maximum temperature rise is only around 2 ˚C at 30,000 rpm.

Table 6-2. The oil dissipated mechanical losses and shaft temperature rise with DC off.

Rotating speed (rpm)	Friction losses P_F (W)	Oil dissipated (W)	Shaft temperature rise (℃)
5,000	76.4	69.1	0.25
10,000	162.3	138.6	1.09
15,000	266.3	213.4	1.35
20,000	358.1	270.4	1.53
30,000	545.8	365.8	2.14

Table 6-3. The oil dissipated shaft iron losses and shaft temperature rise with DC on.

Rotating speed (rpm)	Iron loss P_e (W)	Oil dissipated (W)	Shaft temperature rise (℃)
5,000	81.7	73.6	17.5
10,000	237.7	202.4	27.4
15,000	410.8	341.0	35.9
20,000	611.6	513.6	45.4
25,000	810.5	673.5	52.2
30,000	1029.8	854.6	60.8

Table 6-3 shows that the value of the iron loss increases with the rise in the rotational speeds. It can be explained that the increase in the speed enhances the distortion frequency of the magnetic field in and around the shaft. Furthermore, more than 80 % of the iron losses are taken away by the oil from the shaft wall. It shows that oil cooling is dominated compared to the nature convection and conduction in this test rig. As was anticipated, the temperatures of the shaft increase as the iron loss also rises.

6.5.3 Influence of the Rotational Speed

Fig. 6-11 shows the relative velocity of the flow that passes through the hollow-shaft using different CFD models. As illustrated, when the shaft is at rest, several recirculation zones form at the corners of the shaft hole. Further downstream, the reverse flows are created after being deflected by the wall. Consequently, a complex

flow structure consisting of a vortex is formed. However, when the shaft is driven at 5000 rpm, all turbulence models identity that the flow tends to move radially towards the wall due to the centrifugal and Coriolis effects. More specifically, the two eddy viscosity models (Realizable k-ε and SST k-ω) produce an almost linear profile of the swirl velocity, which describes a solid body rotation. However, the RST model has the ability to simulate the effects of mean rotation and curvature for strong swirling flows. All flows are discharged axially out of the shaft end.

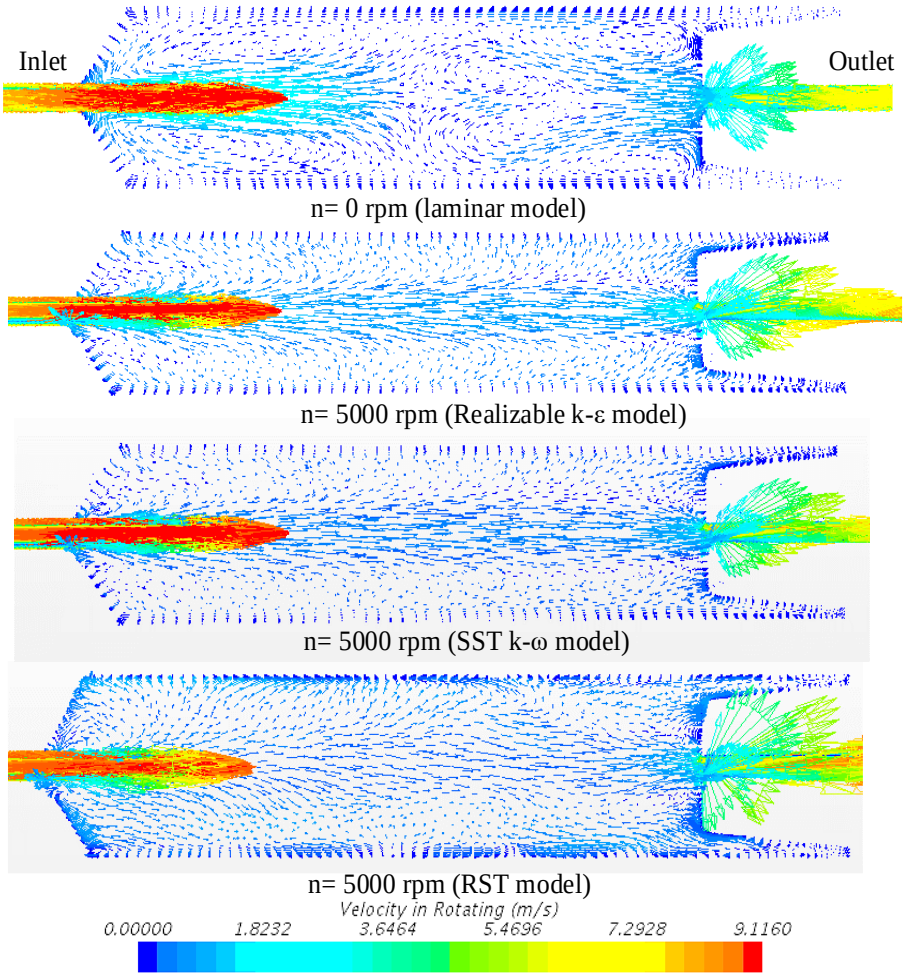

Fig. 6-11. Flow field inside shaft hole at different CFD models.

A comparison of the results obtained from the different turbulent models and experiments at various speeds is displayed in Fig. 6-12. In order to highlight the dynamic effects resulting from the various kinds of rotational speed, the shaft is required to be at rest. The convective coefficients from the existing correlation defined as (6-10) [36] is suitable to the heat exchange between the shaft and the coolant in

relation to such static conditions. This correlation is applied to the laminar flow with a Prandtl number of more than 5.

$$Nu = 3.66 + \frac{0.065 \times \mathrm{D}/L \times Re_a Pr)}{1 + 0.04 \times (\mathrm{D}/L \times Re_a Pr)^{2/3}} \tag{6-10}$$

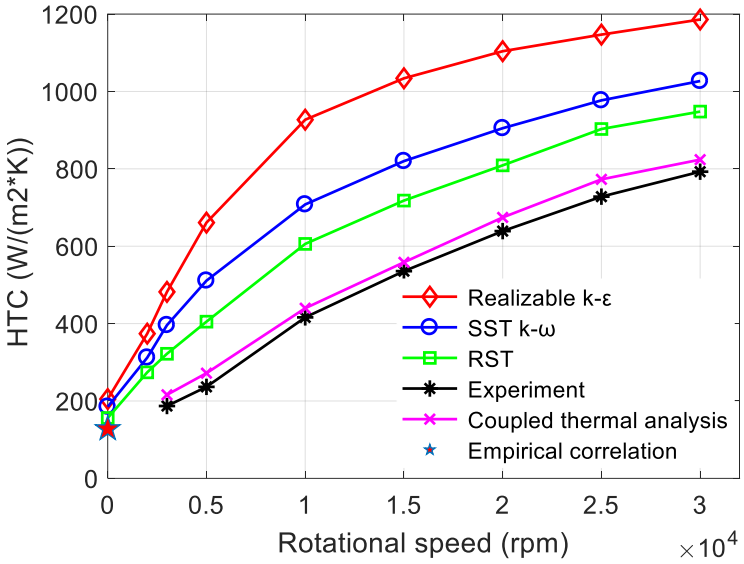

Fig. 6-12. Evolution of the HTC with rotating speed.

It is noticed that the value of the HTC increases with the rotational Reynolds numbers in three methods. Especially, the HTC significantly increases at the low rotational Reynolds number above the station level. This is explained by the rotation which generates a destabilizing effect on the laminar flow and a turbulent flow region that has become separated off is formed near the shaft wall. As a result, the temperature exchange between the shaft and the fluid particles is enhanced. Moreover, the cold and denser fluid in the center tends to move radially to the wall due to the centrifugal and Coriolis effect. This phenomenon changes the flow field in the shaft hole, resulting in a higher convective heat transfer. However, when the rotational speed increases, the value of Nusselt number increases slightly at high rotational Reynolds numbers. It seems that the effect of rotation on the heat transfer is weaken at high speeds. The flow in the hollow-shaft is becoming stable and the destabilizing effect on the laminar flow is saturated.

The relative error ε between the turbulence models and the experiment is shown in Table 6-4. It is noticed that the Realizable k-ε model has the greatest discrepancy. This is due to the fact that the Reynolds stresses in realizable k-ε model have the linear

relation with the mean strain rate of the fluid element. Moreover, the turbulence viscosity is assumed to be isotropic by using the Boussinesq approximation. These assumptions tend to strongly underestimate the anisotropy of turbulence in strong swirl flow. In the case of the SST k-ω model, a cubic constitutive formulation accounting for anisotropy of turbulence is employed. This modification has been shown to improve the turbulence predictions in relation to strong secondary flows and offer a better agreement with the testing data. However, the simplistic eddy viscosity based on Boussinesq assumption for the Reynolds stresses still does not represent the anisotropy of the flow field adequately.

Table 6-4. Comparison the relative errors between CFD and testing results.

Rotational Speed (rpm)	2,000	5,000	10,000	20,000	30,000
ε_k-ε (%)	58	59	52	42	34
ε_k-ω (%)	50	47	38	30	24
ε_RST (%)	37	33	27	21	17

The RST model as a second order closure scheme predictions has a smallest relative error with the experimental measurements. This is because that the Reynolds stress tensors are solved directly using governing transport equations rather than specifying it based on the Boussinesq approximation. Furthermore, the effects of the anisotropy of turbulence in strong swirl flow are naturally taken account in the governing equations. Consequently, the RST model has the potential to predict the strong swirling flows more accurately than eddy viscosity models. However, the computations of RST models are highly time-consuming.

It is noted here that the three different turbulence models follow the trend of the experimental data. It is found that CFD models tend to always over-predict the HTC as compared with the experimental measurements. These variations can be partly explained due to the turbulent models are uses the Boussinesq assumption that the viscous stresses are proportional to the instantaneous rate of the deformation. This makes the Reynolds stresses proportional to the mean rate of deformation of the fluid element with turbulence viscosity assumed to be isotropic. Moreover, the limitation of the numerical models, might not be able to capture the effects of turbulence anisotropy, streamline curvature, swirl rotation and high strain rates. It is acknowledged that the accuracy of the convective heat transfer prediction on the hollow-shaft inner wall

surface can be improved by using finer modelling techniques, such as URANS (Unsteady RANS) or Large Eddy Simulation turbulence model [122]. However, these approaches are very expensive in terms of computational time.

6.5.4 Influence of the Flow Rate

Several flow rates between 3 L/min and 7 L/min have been tested in order to find out the effects of axial flow on the HTC. As shown in Fig. 6-13, the HTC of the shaft increases slightly with the flow rate based on the correlation defined as (6-10) when the shaft is at rest. However, it is noted that under conditions where the shaft rotational speeds remain at the same level the following results can be observed: the value of the HTC is almost constant. It can be explained that the axial flow is less influenced for the high rotational speed and the convective heat transfer is governed by the rotation.

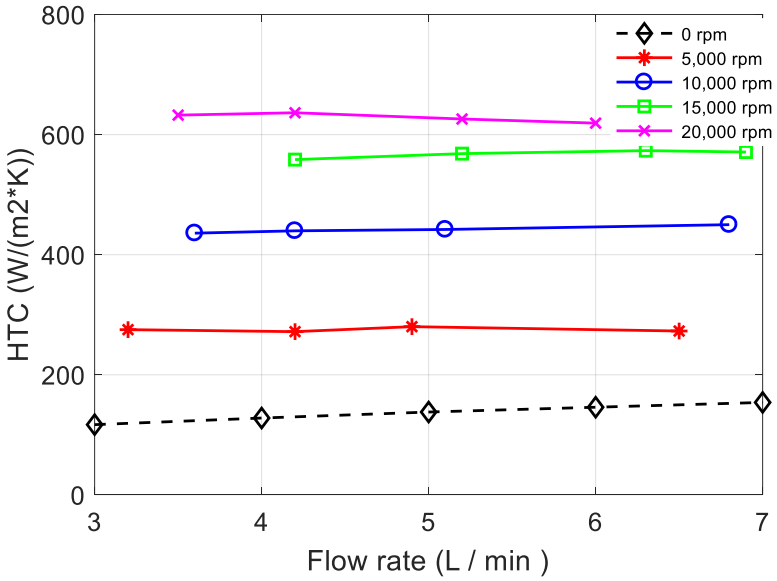

Fig. 6-13. Evolution of the HTC with inlet flow rate for different rotational speeds.

6.5.5 Influence of the Coolant Temperature

In addition to the axial and tangential speed effects, another factor that significantly influences the HTC is the fluid properties. The coolant used in this test is a Newtonian fluid, whose viscosity only depends on the temperature. In the CFD simulations presented so far, the fluid properties vary depending on the operating conditions of the machine. On this basis, the three different temperatures of the coolant were used to test the fluid properties on the heat transfer due to rotation. The comparison of the CHTC at various coolant temperature are shown in in Fig. 6-14. The resulting HTC do

not vary more than 20 when all other cooling configurations are the same. It shows that at high rotational speeds, the viscosity effect on heat transfer is inappreciable. Compared to the centrifugal and Coriolis effects at high speeds, the force on the flow due to viscosity is almost non-existent.

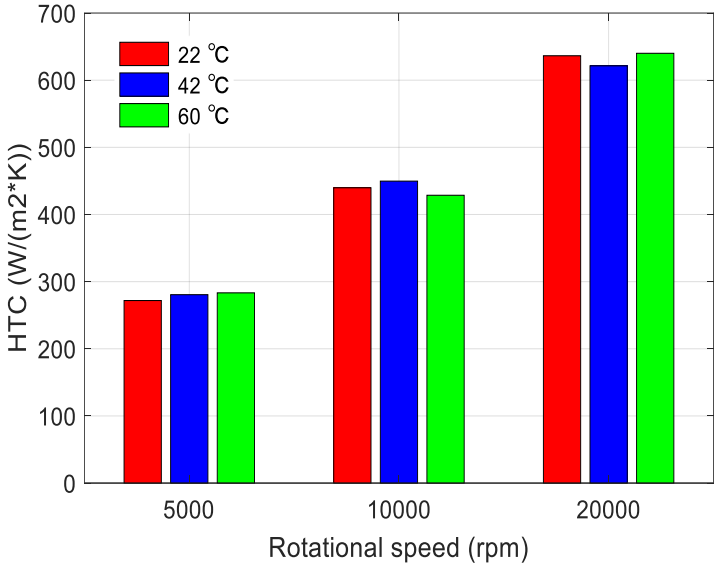

Fig. 6-14. Evolution of the HTC at various inlet coolant temperatures.

6.5.6 Non-dimensionalise the HTC Results into an Equation

Based on results obtained from the experiments, the heat exchanges between the shaft's internal surface and the coolant are mainly determined by the rotational flow rate. It is almost independent of the inlet flow rate and the viscosity of coolant. For a laminar low ($Re < 180$), an equation (6-11) is proposed to describe the Nu in a steady state based on the Re_r and Pr.

$$Nu = A(\frac{1}{Re_r * Pr})^B \tag{6-11}$$

This simple equation is obtained by using the least square method in relation to a flow with Re_r ranging from 2,375 to 1.75e+5, Pr varying between 145 and 712 and $Re_r * Pr$ ranging from 1.69e+6 to 2.54e+7. The values for A and B are derived and listed in Table 6-5. This equation can be applied in a number of flow channel geometrical dimensions, as well as at various axial flow rates and rotating speeds. This allows thermal designers to use these parameters to identify the heat transfer coefficients of

rotor cooling system with an internal axial flow. As a result, thermal designers can gain an accurate understanding of the thermal model rather than opt for a test trial.

Table 6-5. Coefficient for correlation.

Coefficient	A	B
Value	3.811E-3	-0.641

6.6 A case study

An interior permanent magnet traction motor based on a scaled-up equivalent topology to Nissan Leaf traction motor [96], is used to verify the benefits of shaft cooling on thermal management of traction motors. High operation temperature of rotor can cause partial or full demagnetization of rare earth magnets, which can lead to a significant decrease in output torque. The cross-sectional view and key parameters of this traction motor are shown in Fig. 6-15 and Table 6-6, respectively.

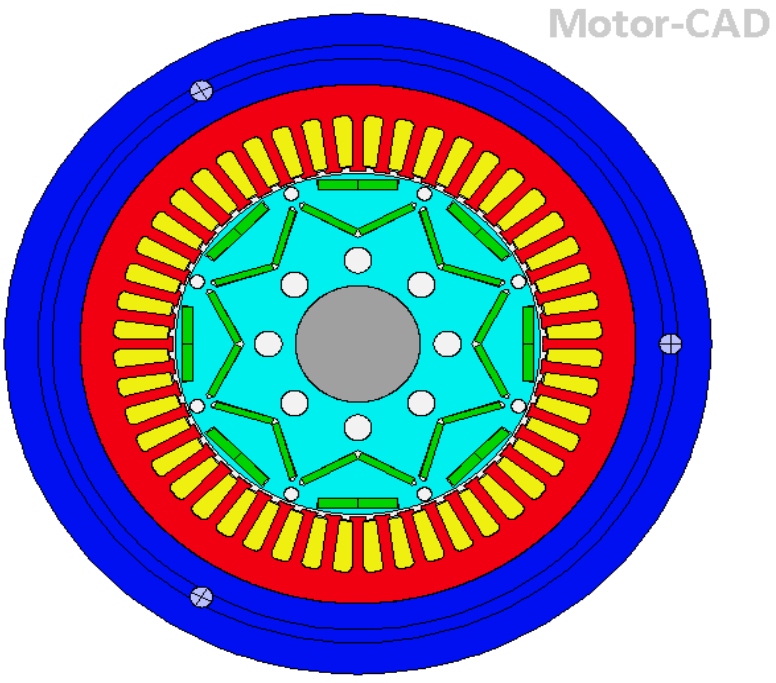

Fig. 6-15. Schematic of the interior permanent magnet traction motor.

The original cooling system shown in Fig. 6-16 (A) is the housing water jacket with the 6.5 L/min volume flow rate at 65 °C inlet temperature. The improved cooling system is illustrated Fig. 6-16 (B), the oil with the 5 L/min flow rate is forced to pass through the hole of the shaft to cool down the magnet. The dimensionless correlation from (6-11) was used to calculate the convective HTC of the hollow-shaft cooling when the

rotational effects are considered. If the rotational effects are not taken into account, such convection HTC is based on static state results from (6-10). The coupled electromagnetic and thermal analysis is processed by Motor-CAD [145] in order to find out the improvement of thermal performance after optimizing the cooling system.

Table 6-6. Specification of the interior permanent magnet traction motor.

Parameter	Value
Number of poles	8
Number of slots	48
Length of air gap	1 mm
Outer diameter of stator	220 mm
Inner diameter of stator	146.67 mm
Electric steel	30 DH
Magnet	N35UH

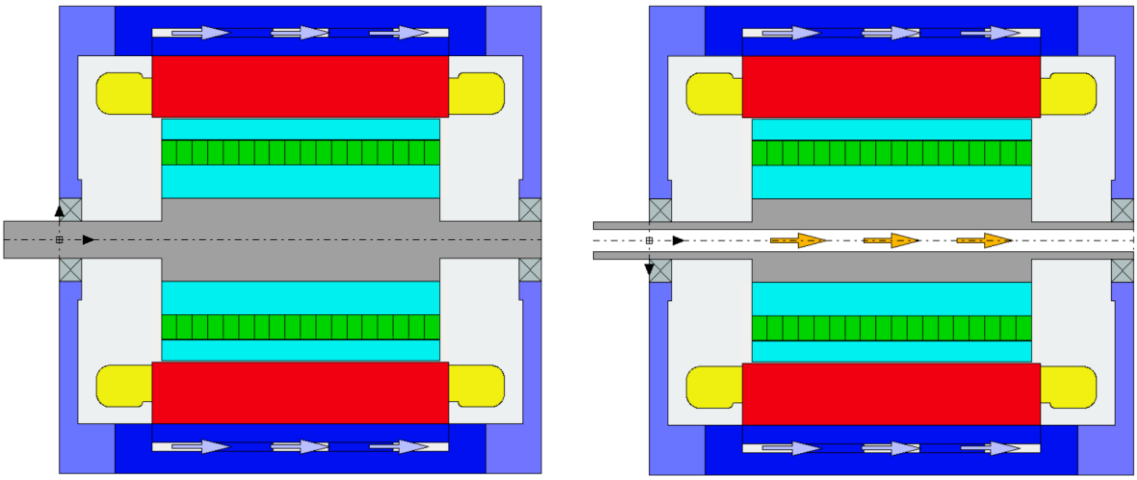

(A) (B)

Fig. 6-16. The original cooling system A (Water jacket cooling), the improved cooling system B (Water jacket + shaft cooling).

The average temperature of rotor and windings are compared in Fig. 6-17 and Fig. 6-18. It can be noted that the hollow-shaft cooling system can cause a larger decrease in the rotor temperature and a slight drop of winding. The average of rotor temperature has a 20 ℃ drop cross the range of operation speeds if the rotational effects on the convective HTC are considered.

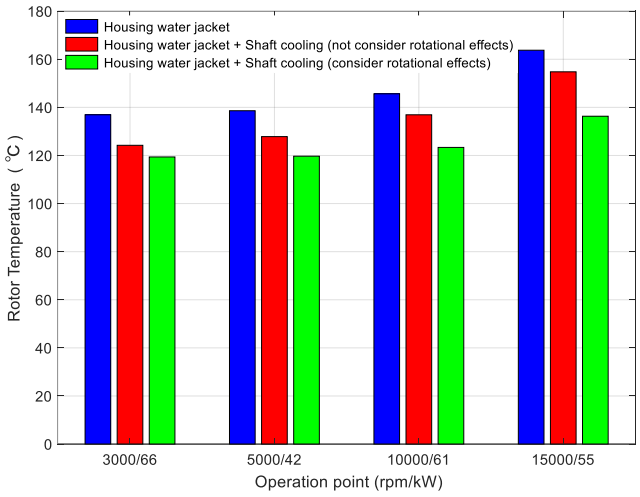

Fig. 6-17. Rotor temperature for various operating points.

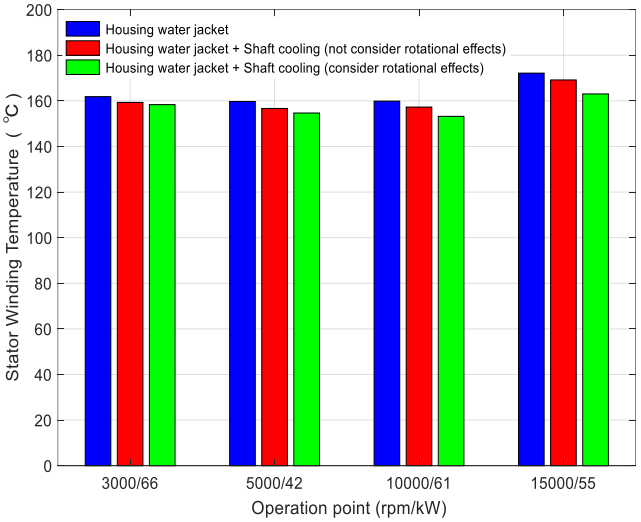

Fig. 6-18. Winding temperature for various operating points.

6.7 Summary

This chapter deals with an oil-based hollow-shaft rotor cooling system as applied to a high speed automobile traction motor. Several experimental tests have been carried out to evaluate the thermal performance of this cooling method. Due to the centrifugal and Coriolis effects, heat exchanges are thus promoted by the rotation. The HTC increases sharply as compared with the stationary case. This is explained that a destabilizing effect is generated by the shaft rotation due to the increase in the shear stresses. However, when the rotational speed increases, the flow seems to be saturated. And the effects of rotation on the heat transfer are weaken when the rotation speed reaches 30,000 rpm. Furthermore, and first of all, the heat transfer rate is mainly

governed by rotation and, secondly, it is almost independent of the inlet flow rate and of the viscosity of coolant. These latter two parameters show a very limited influence on the heat transfer of the cooling method under consideration.

7 Study of Pressure Loss in a Hollow-Shaft Cooling System

The axial flow rate of the coolant through such a hollow-shaft is commonly decided and limited by the pump performance and the system flow resistance. The intersection of the pump curve with the system curve defines the operating flow rate. This flow rate not only impacts the pump efficiency but also is an important parameter in the cooling system that links to the convective heat transfer. However, the flow rate is inversely proportional to the system flow resistance. As a result, a better understanding of the flow distribution in the cooling paths and their pressure losses will significantly benefit the thermal management of automotive traction motors [144].

7.1 Introduction

When the coolant enters an axially rotating hollow-shaft, the tangential force causes the coolant to rotate with the shaft due to the fluid viscosity. Consequently, a secondary flow is induced by the centrifugal force and the Coriolis force from a rotating reference frame. However, the rotating flow is rather different from that observed in a nonrotating hollow-shaft. The rotating effects on the flow resistance have been reported by many authors. The stabilization effect in the axially rotating pipe flow has been convincingly demonstrated by [146] for a fully turbulent flow. The flow resistance is considerably reduced by up to 40% at the high rotation speeds corresponding to the situation in a stationary pipe. The experiments carried out by [103] show the same phenomenon, in addition to which it is revealed that the axial velocity distribution tends to shift from a turbulent into laminar pattern. However, in relation to the fully laminar flows, based on the experimental and analytical demonstrations provided here these cannot be maintained in a rotating pipe [147]. A destabilizing effect is revealed in [148] using a modified mixing length theory. This destabilizing effect causes a significant rise in the pressure loss due to the increase of the friction coefficient between the flow and the wall. However, these studies are only pertinent in cases where the high values of the length to diameter ratio are in place. It is not valid for the hollow-shaft cooling of traction motors with a low length to diameter ratio. Moreover, in cases of low values of the length to diameter ratio there is still limited knowledge of the pressure loss trends in

relation to the fully developed turbulent flows. More importantly, the rotating speeds investigated within the current literature are very low. The effects of high rotational speeds on the pressure loss are still unclear.

A numerical simulation method may provide the reliable estimations regarding the pressure losses of complicated rotary systems. The pressure loss of the stator-rotor gap is investigated in [149] by using the SST k-ω turbulence model. It demonstrates that the flow resistance caused by rotation can be significant. Moreover, the effects of the pipe rotation on pumping fluid through the tool joint are measured by CFD as in [150], where it is pointed out that the pipe rotation has two counter effects on the pressure drop depending strongly on the flow velocity.

This chapter analyses the effects of rotation on the friction factor for the turbulent and laminar flows. The CFD is used to calculate the pressure losses by taking the rotational effect into account. On this basis, the coolant streamline gives a visualization of the flow patterns under the effects of rotation. Then the trend of the pressure losses along the shaft at various rotation rates is explained in detail. Moreover, the experiments are carried out to validate the simulation results.

7.2 Stationary Pressure Loss in a Hollow-Shaft Cooling System

When the coolant is flowing through the stationary hollow-shaft, the coolant experiences the energy losses due to some resistance. The major energy loss is from the friction caused by shear stresses in the fluid as a result of viscosity. In addition, separation losses arise from flow disturbance due to change the coolant velocity in magnitude or direction such as a valve, flow measurement device, junction and etc. As a result, the flow passes through these disturbances resulting pressure loss.

7.2.1 Friction loss

The Darcy-Weisbach equation is phenomenological formula, which relates the pressure loss due to friction in a static pipe [80].

$$\Delta p = f\frac{L}{D}\times\frac{1}{2}\rho V^2 \tag{7-1}$$

where f is the Darcy friction factor.

For the laminar flow, f is given by the following formula:

$$f = \frac{64}{Re} \tag{7-2}$$

For the fully developed turbulent flow, the friction factor f of the smooth wall can be approximated using the empirical relation proposed by Blasius [151]

$$f = \frac{0.316}{Re^{0.25}} \tag{7-3}$$

7.2.2 Sudden Expansion and Contraction Losses

A sudden expansion or contraction occurs when there is a sudden change of the cross section area along the length of the shaft cooling system. At the expansion point, the flow is separated and turbulence eddies is generate at following flow. The counter flow grows at the separation junction, followed by strong mixing and recirculates to the mainstream. For sudden contraction flow, the separation occurs in the downstream pipe and forms a vena contract. The main stream contracts to a minimum diameter before it recovers to occupy the pipe cross section area. The mechanical energy losses is associated with flow passing through to downstream in this two situations. The pressure loss of a sudden expansion and contraction flow is based on the mean velocity V in the pipe of smaller cross section area (i.e. inlet for before expansion, outlet for contraction).

$$\Delta p = k_s \times \frac{1}{2}\rho V^2 \tag{7-4}$$

$$k_s = (1 - \frac{A_i}{A_o})^2 \tag{7-5}$$

where A_i and A_o are inlet and outlet cross section areas respectively.

7.3 Rotational Pressure Loss in a Low-Speed Water-Cooled Hollow-Shaft

The resulting rotational pressure loss is assumed to be due to the effect of rotation. When a flow enters an axially rotating shaft, tangential forces acting between the

rotating pipe and the fluid cause the fluid to rotate with the pipe, resulting in a second flow pattern which is perpendicular to the direction of the main flow and rather different from that observed in a nonrotating pipe. As the fluid friction is associated with shear stresses developed between layers within the fluid that are moving relative to each other, the formulas of friction factor for stationary case cannot be applied for rotating case. The additional forms of friction loss is generated which results the extra pressure loss.

7.3.1 Experimental Setup

Fig. 7-1 shows a schematic diagram of the experimental setup, where the water is pumped and re-circulated from a container into the test rig. The function of the chiller is set at a constant temperature value. The volume of water that flows through the shaft is regulated using a globe valve and measured using a flow meter. Fig. 7-2 presents the experimental test rig, where the hollow shaft is rotated by an electric motor with a variable drive operating at speeds up to 5000 rpm. The testing shaft consists of the following three parts: first, the middle rotation region with a length to diameter ratio (L_r/D) of 30; and second and third, there are the two sides of the shaft. These latter two are in the stationary region with a L_s/D ratio of 10. The experiment was repeated for various coolant flow rates and at a number of shaft rotating speeds, as shown in Table 7-1. Each experiment was run at least 30 minutes after equilibrium conditions were established.

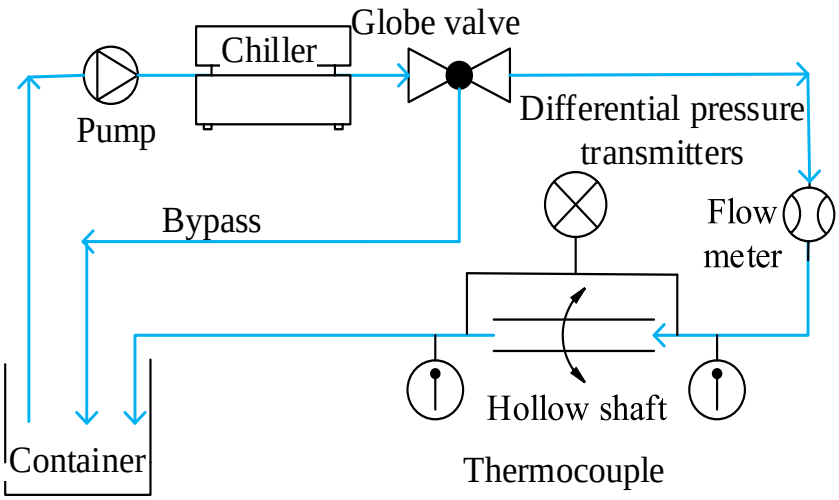

Fig. 7-1. Test set-up.

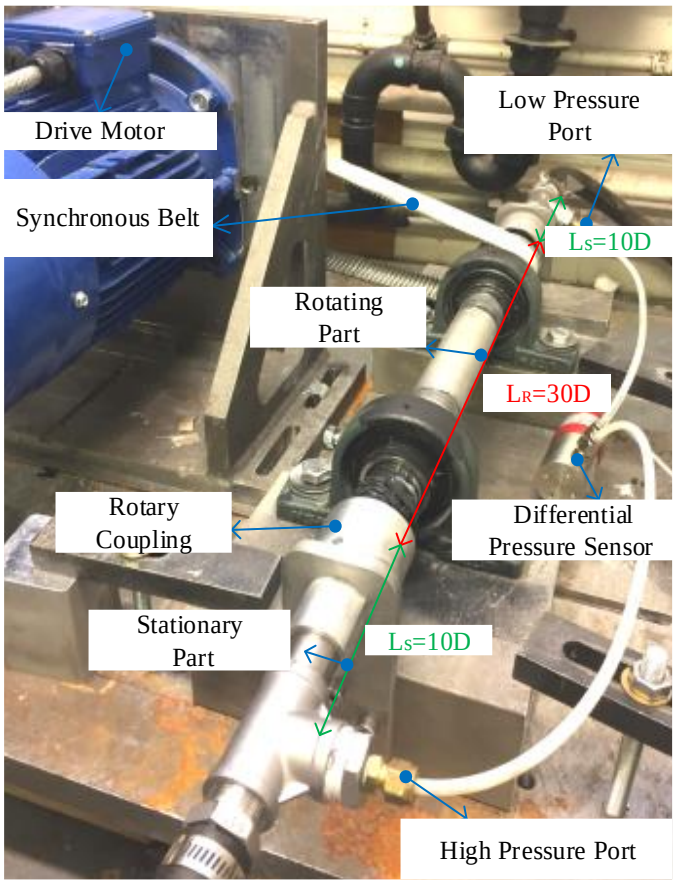

Fig. 7-2. Experimental test rig.

Table 7-1. Experiment details.

Coolant inlet temperature (°C)	Flow rates (Litre/min)	Shaft rotating speed (rpm)
20	8, 12, 16, 20	1000, 2000, 3000, 4000,4500

7.3.2 Pressure Measurement

The pressure measurements are conducted using a Sontay PL-692 range of differential transmitters. This pressure transducer has a measurement range from 0 to 100mbar with an accuracy of $\pm$ 0.5% and provides a DC voltage output proportional to the pressure drop. The pressure sensor is also connected to the Agilent Technologies 34970A for recording the output voltage. A linear relation is provided in (7-6) between output voltage V vs pressure drop Δp (mbar).

$$\Delta p = 10 * V \tag{7-6}$$

7.3.3 Results and Discussion

The rate of the shaft rotation is defined by the ratio of the circumferential velocity of the shaft's inner wall to the mean axial flow velocity as

$$N = \frac{Re_r}{Re} = \frac{V_r}{V} \tag{7-7}$$

In cases where a validation of the experimental method is carried out, the shaft is required to be at rest, so that the dynamic effects due to the rotational speed can be better highlighted. The results of the pressure losses from, firstly, the CFD model (Presented in Chapter 3) and, secondly, the experiment – are compared with the data from Blaisus's correlations in (7-3) [151] is shown Fig. 7-3.

For the stationary condition, the increase in the axial coolant flow rate enhances the pressure losses between the shaft and the coolant flow. It is noted here that the numerical and experimental data closely follow the trend of Blaisus's correlation, with the experimental results showing higher values than the simulation results. These variations can be partly explained due to the rough surface of the shaft's internal wall as compared to the perfectly smooth one assumed in the modeling. In addition, sectional changes of the flow disturbances in the fittings also generate the extra pressure losses.

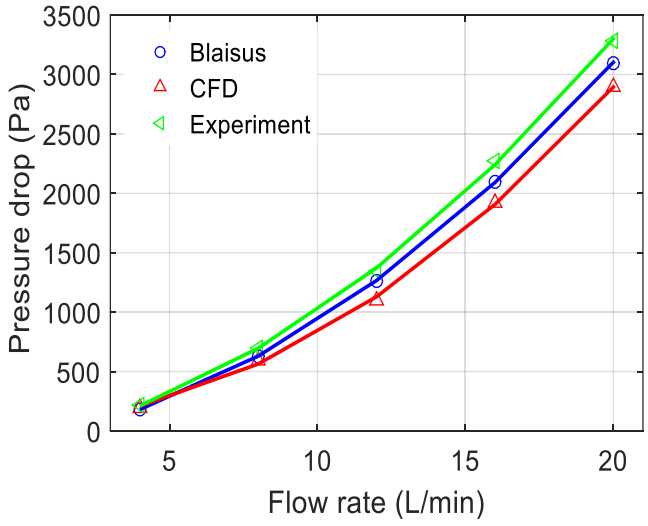

Fig. 7-3. Plots of the pressure drop with the flow rate.

The streamlines of coolant passing through the hollow-shaft in various N are shown in Fig. 7-4. The coolant is becoming helical due to the tangential forces caused by rotation

between the shaft and the fluid. The level of helix flow increases with the rise in N. It is also found that the swirl rate is sufficiently high in the region near to the wall. This swirl rate increases gradually in proportion to the direction of the flow direction and finally reaches the tangential speed of the inner shaft wall.

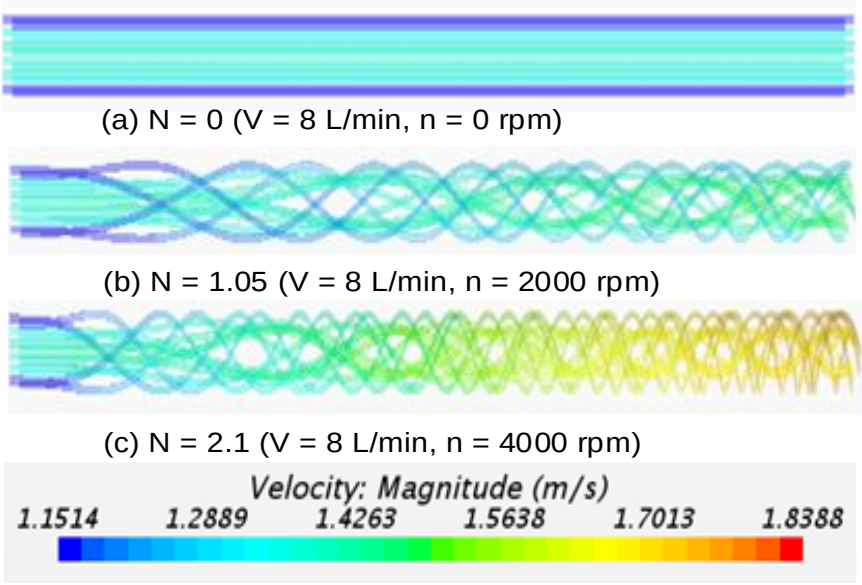

Fig. 7-4. Coolant streamlines passing through the hollow-shaft in various N.

The resulting rotational pressure loss is assumed to be due to the effect of rotation. This is because the fluid friction is associated with shear stresses developed between the flow and the wall that are moving relative to each other. In comparison with the stationary condition, the fluid suffers a different pressure drop due to the rotation. Fig. 7-5 presents the shear stress at the various N. It shows that the shear stress is constant when the shaft is at rest. However, when the shaft starts to rotate, the shear stress is not an even distribution any more. From Fig. 7-5 (b) and (c), it is noted that the shear stress is the highest at the entrance to the shaft. Then it reduces gradually in proportion to the direction of the flow. This fact can be explained by the abrupt change in the direction the flow in the hollow-shaft due to the rotation. This means that the rotation has a destabilizing effect on the flow. As a consequence, the flow becomes more turbulent. The level of turbulence at the entrance to the shaft is proportional to N. However, at the downstream of the flow, the turbulent effects slowly dwindle. The level of turbulence is dampened down due to the centrifugal force of the swirling velocity component. The shear stress is also decreasing along the shaft at the downstream of the flow.

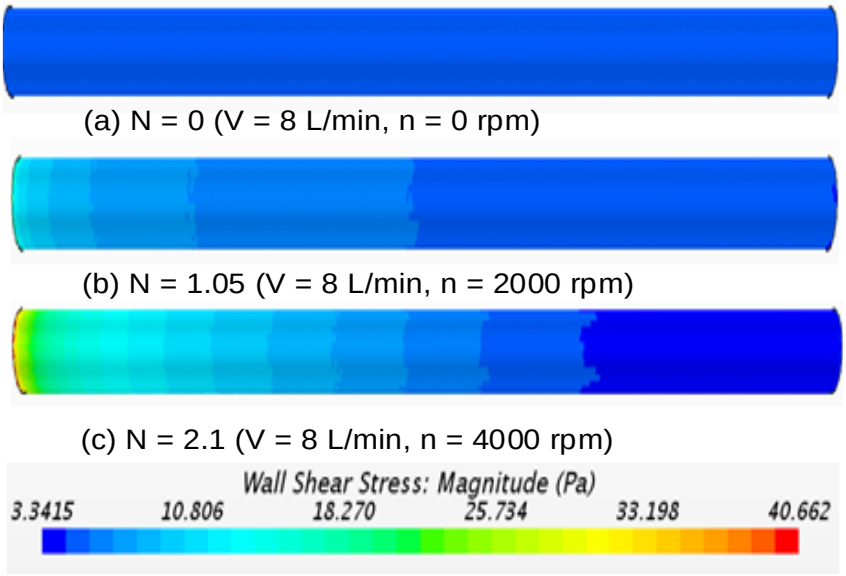

Fig. 7-5. The wall shear stress as compared with various N.

In order to provide a better understanding of the rotating effects on the flow and the friction factor, the rotating shaft is divided into 6 even parts (5D in length per each) and numbered from 1 to 6 (the direction of the flow). The values of the rotational friction factor f_r relative to the stationary case f_s at N have been plotted in Fig. 7-6. When the shaft begins rotating, it is noted that the pressure losses increase with the rise in the rotating speed. The value of the pressure losses reach its peak, then starts to decrease at the downstream of the flow. However, the effects of the pipe rotation on the pressure loss is not significant at a low tangential velocity. In contrast, the rotational effect is significant at a higher velocity throughout the whole length of the shaft. To explain the boosting and depressing effects, two phenomena can be addressed. At the entrance to the shaft, the centrifugal mass forces have a profound effect on the flow, increasing the turbulence arising from the external forces. This causes the pressure to drop sharply. However, at the downstream of the flow, a conservative effect on the flow can be observed. It leads to the suppression of the turbulence and the stability of the flow. The turbulence in the flow will be largely suppressed so that viscous effects become dominant. As a result, the pressure losses are decreasing.

When the coolant is discharged from the outlet into the stationary region, the nature of the flow changes abruptly again from a swirling state to a stationary position. This causes the pressure to drop more when downstream from the outlet. Fig. 7-7 shows the shear stress at the junction between the rotating and stationary regions. It is noted

that the shear stress is the highest at the junction of the two regions. The level of stress is proportional to the rotation ratio. A higher initial rotational energy will generate more pressure loss when the tangential force suddenly disappears. However, when the flow continuously dissipates downstream, the pressure loss gradually diminishes until the pressure loss becomes constant. In other words, the numerical value of the pressure loss remains the same.

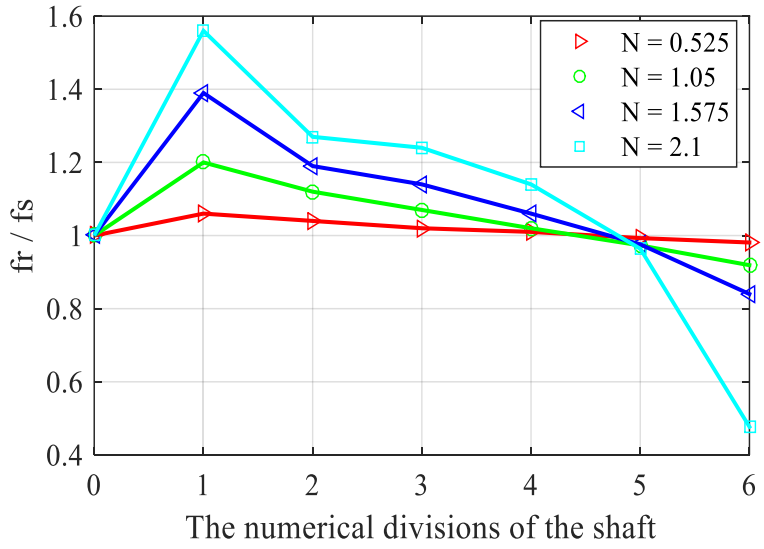

Fig. 7-6. f_r/f_s at various N in the numerical divisions of the shaft.

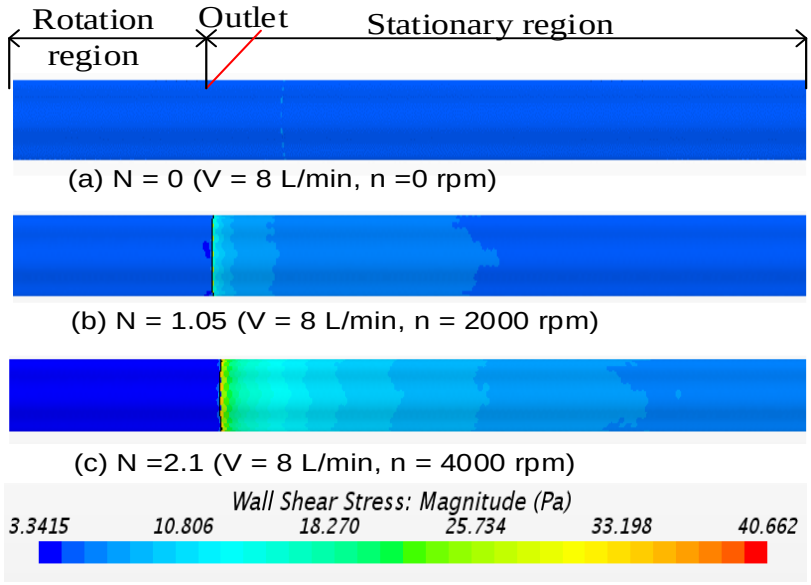

Fig. 7-7. The wall shear stress of the junction at various N.

A comparison of the results obtained from the CFD simulation on the one hand and the experiment on the other is presented in Fig. 7-8. It is noted that with the rise in the

rotational speed the overall pressure losses increase slightly. This phenomenon is the result of the combination of three parts of the testing shaft. The upstream stationary part has the same pressure loss due to the fixed axial flow rate. However, the pressure loss in the middle or rotating part gradually rises, as the rotation speed increases. This is because the increased pressure loss stems mainly from the destabilizing effects that take place at the entrance to the shaft. In contrast, a reduction in the pressure loss prevails once the swirling flow moves downstream. But overall there is a slight rise in the pressure drop, due to the fact that the increase in the pressure loss at the entrance to the shaft outweighs any contrary effect downstream. In short, the rise is the slightly dominant trend as against the marginally smaller reduction. Furthermore, the pressure loss in the downstream stationary shaft increases with the rotating speed rise. This can be explained by the fact that the destabilizing effects still affect the flow, even with the disappearance of the tangential force. The discrepancy between the numerical method or simulation on one side and the experimental tests on the other is due to two factors: first, the sectional changes in the flow disturbances; and second, the losses on account of the abrupt change in the direction of the flow around the entrance.

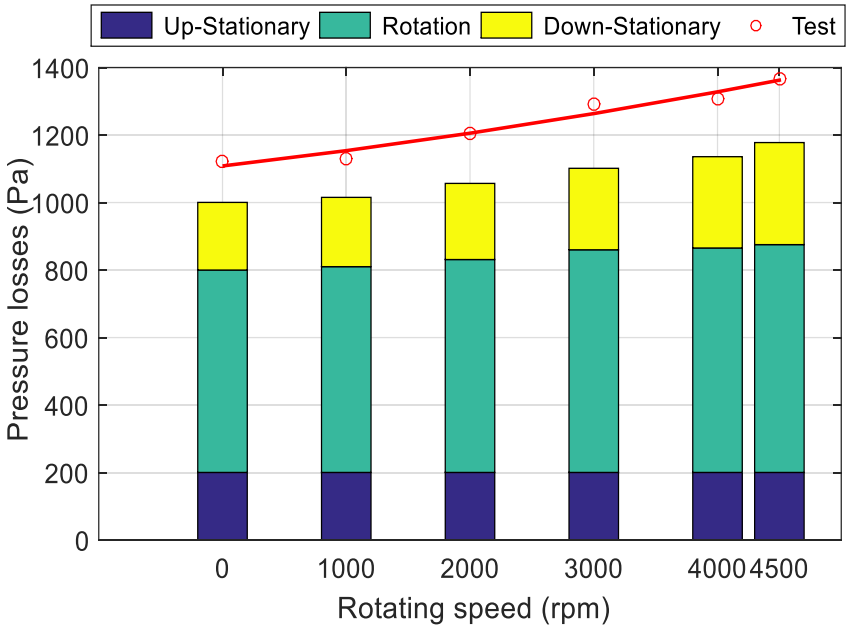

Fig. 7-8. Pressure loss at various rotational speeds.

The values of the rotational friction factor f_r relative to the stationary case f_s at N in the six numerical divisions of the shaft have been plotted in Fig. 7-9. The f_r/f_s is the highest at the entrance of shaft due to the high shear stress of the rotation. It is

concluded that the rotational speed can significantly increase the value of f_r/f_s about 2.4 times at a rotational ratio of 4.2 above the level of the stationary condition. Then f_r/f_s starts to decrease along the shaft at the downstream of the flow. The high speed rotation has a very marked influence on the suppression of the turbulent motion because of the centrifugal forces that are growing at the radius. The turbulence in the wall region of the rotating shaft will be largely suppressed at high rotational speeds. At the end of the shaft, the rotation friction factor is only about 50% of the stationary level when the rotation ratio is 4.2. The increase in the shaft rotation continuously reduces the hydraulic losses. This results in a shift from a turbulent type to a laminar one. However, the lower the rotational speed, the less effect on the friction factor. At the lower end, the friction factor in relation to rotation is almost the same as that attained at the stationary level. These facts point to two opposite effects on the flow: first, to the destabilizing effect which prevails in the inlet region and second, to the stabilizing effect which is predominant in the area far from the inlet.

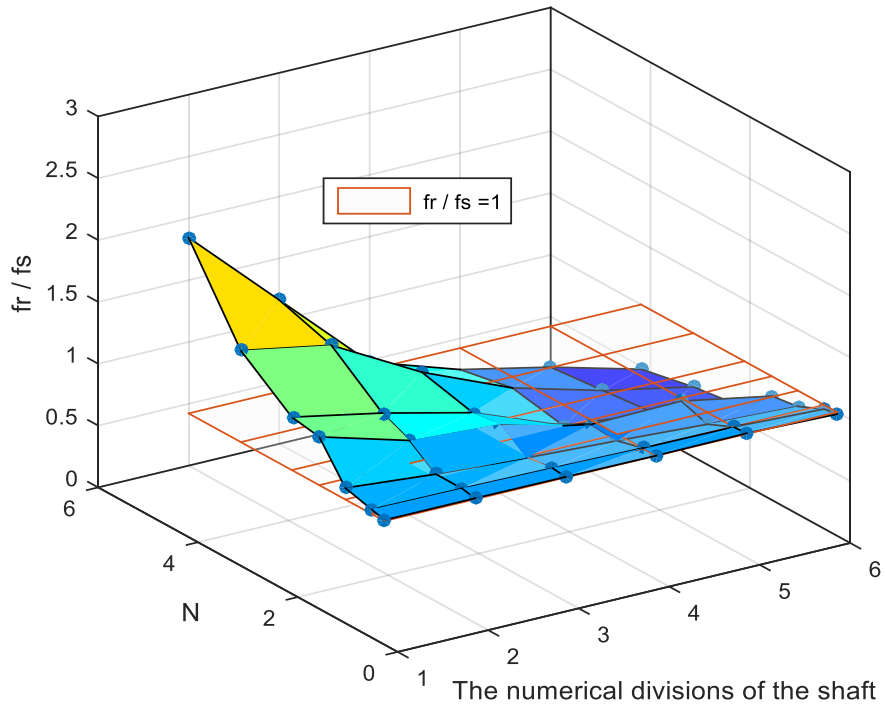

Fig. 7-9. f_r/f_s at various rotation ratios and the numerical divisions of the shaft.

7.4 Rotational Pressure Loss in a High-Speed Oil-Cooled Hollow-Shaft

7.4.1 Setup and measurement

The setup of pressure loss calculation for laminar flow has been shown in Fig. 6-1. The pressure measurements in this test are conducted using Gems Sensors 3100 series pressure transmitters. This pressure transmitter has a measurement range from -1 to 24 bar with an accuracy of $\pm$ 0.25% and provides a DC voltage output proportional to the pressure reading. The pressure transmitter is also connected to the Agilent Technologies 34970A for recording the output voltage. A linear relation is provided between output voltage V vs oil pressure P (bar).

$$p = 4.8 * V \tag{7-8}$$

The pressure drop of shaft cooling system can be calculated by the value of inlet p_{inlet} and outlet p_{outlet} pressure meters.

$$\Delta p = p_{outlet} - p_{Inlet} \tag{7-9}$$

7.4.2 Results and Discussion

In order to better highlight the dynamic effects due to the rotational speed, the shaft is required to be at rest. The results of the stationary pressure losses from, firstly, the CFD model (Presented in Section 5.3.1) and, secondly, the analytical method (Presented in Section 7.2) – are compared in Fig. 7-10.

Similar to the water-cooled hollow-shaft, the increase in the axial coolant flow rate also enhances the stationary pressure losses between the oil and the shaft's internal wall. Moreover, the plots on the graph show that the rise in coolant temperature has the effect of decreasing the pressure losses. This is because an increased temperature in oil leads to a decrease in the viscosity of the mediums. This viscosity drop leads to a decrease in the cohesive forces of the molecules and causes a lower shear stress during the rotation of the shaft. It is noted here that the numerical data show higher values than the analytical results. These variations can be partly explained due to the CFD model taking account the flow separation and secondary flow when change the

coolant velocity in magnitude or direction as compared to the perfectly flow assumed in the analytical modeling. These flow separations cause more pressure losses.

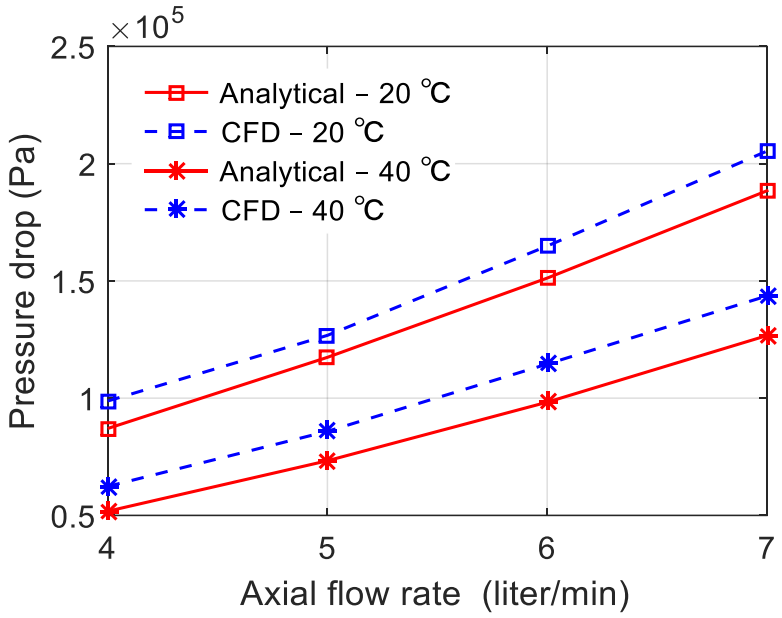

Fig. 7-10. Plots of the pressure drop for the stationary condition.

Fig. 7-11 presents the shear stress at the various N for a laminar flow. It is noted here that the shear stress is constant when the shaft is at rest. However, when the shaft starts to rotate, the shear stress increases with the rise in N. This fact can be explained the rotation has a destabilizing effect on the laminar flow. As a consequence, the flow becomes more turbulent. The level of turbulence is proportional to N. Moreover, the shear stress is the highest at the ends of the shaft. It is due to the sudden expansion and contraction occurs when there is a sudden change of the coolant velocity direction. Furthermore, the shear stress is almost an even distribution at the middle of shaft. This fact can be explained the rotational has the boosting effect on the laminar flow throughout the whole length of the shaft.

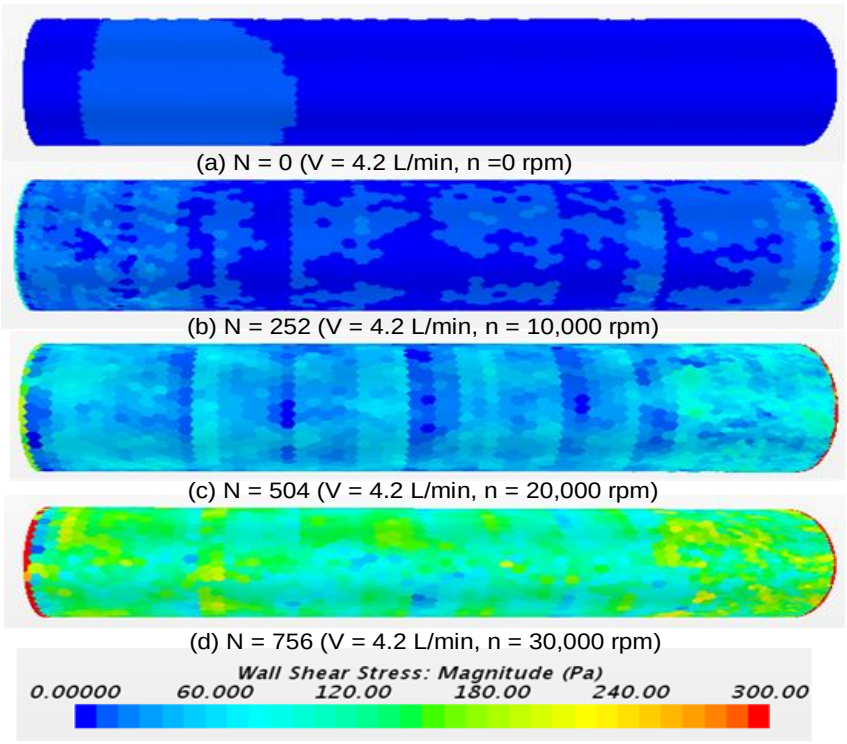

Fig. 7-11. The wall shear stress as compared with various N.

It is noted here that the locations of pressure transmitters in the test rig are not close to the inlet and outlet of the shaft. The testing value achieved based on (7-9) also include the pressure losses from the pipe and connect couplings. These losses are difficult to identify individually. Moreover, the aim of this test is to find out dynamic pressure loss due to the rotation. On account of these, only the extra pressure loss due to rotation are considered. As a result, two different steps were taken to identify the dynamic pressure losses with the shaft at rest and rotation, respectively.

- When the shaft is at rest, Δp_s is the static pressure losses which consist of friction, bending, sudden expansion and extraction losses.
- Rotating the shaft: Δp_r is the static pressure losses in addition rotational pressure losses. Therefore, $(\Delta p_s - \Delta p_r)$ is taken as the dynamic pressure loss due to rotation.

The extra pressure loss due to rotation obtained from the CFD simulation on the one side and the experiment on the other are presented in Fig. 7-12.

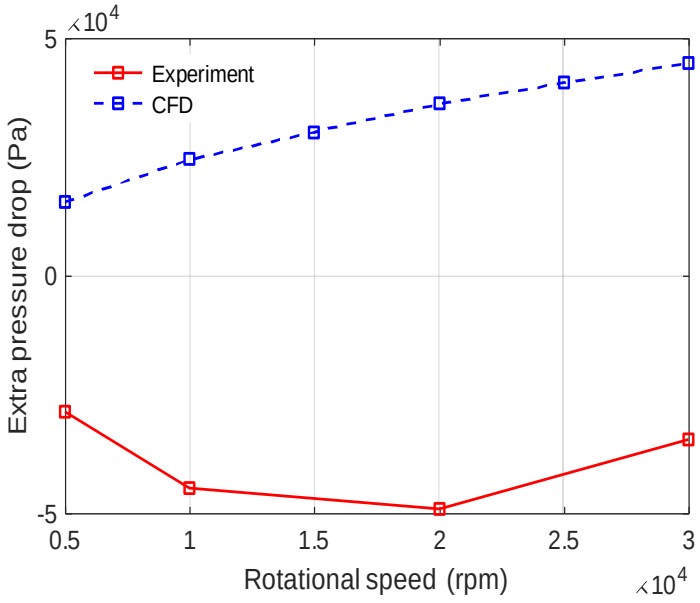

Fig. 7-12. Extra pressure loss due to rotation at various speeds.

It is noted that with the rise in the rotational speed the pressure losses increase slightly in CFD model. This fact can be explained the rotation has a destabilizing effect on the laminar flow. As a consequence, the flow becomes more turbulent and more pressure drop. However, in the experiment, this phenomenon cannot be observed. This is because the pressure drop stems mainly at the entrance and exit to the shaft due to the high rotating speed. A comparison of the test rig geometry in Fig. 5-1 and the CFD model geometry in Fig. 5-8 shows significant differences in the outlet path of the fluid. In the CFD model, the coolant is discharged axially out of the shaft end. Whereas in the test rig, the coolant flows radially out of shaft and impinges on the housing inner wall. As a consequence, the extra pressure losses generated in this outlet path are difficult to identify and have a huge influence on the final results. Moreover, the calculation of the flow pressure loss in the outlet path is beyond the scope of this thesis.

7.5 Summary

In this chapter, considerations are given to how the turbulent and laminar flows are introduced to a rotating hollow-shaft. The pressure losses distribution across various distances from the shaft entrance, along with a number of different flow patterns, were investigated based on a CFD simulation.

For the turbulent flow, the destabilizing effect, which prevails at the entrance to the shaft, leads to an increase in the friction losses due to the excessive external forces within the inner shaft wall. At the rotational ratio of 4.2, the f_r is about 2.4 times the f_s as compared with the stationary case. A stabilizing effect becomes dominant at the downstream of the flow, causing the rotational friction loss to decrease until the flow reaches the steady state and remains substantially unaltered. However, when the flow is discharged from the shaft outlet into the stationary region, the direction of the flow changes abruptly. This causes greater pressure drop at the downstream of the outlet.

For the laminar flow, the rotation has a destabilizing effect throughout the whole length of the shaft and make the flow more turbulent. Furthermore, the shear stress is the highest at the ends of the shaft due to a sudden change of the coolant velocity direction.

When such hollow-shaft rotor cooling system is employed, the more pressure loss would be generated as compared to the stationary case. As a result, the more powerful pump should be applied to keep the flow rate constant without changing the cooling performance.

8 Conclusion and Further Work

8.1 Conclusion

In this thesis, a detailed analysis of the active type cooling: the natural, forced air, forced liquid and phase change types are reviewed. On this basis, a comprehensive summary of the convection methods as applicable to the automotive traction motors cooling contexts have been provided with the advantages and disadvantages of each method being compared. The essential elements for optimizing the cooling performance of each method together with the leading applications are specifically highlighted. In addition, the latest automotive traction motor prototypes and products employing these methods, have been set out and evaluated. Furthermore, the use of the analytical lumped-circuit and the computational fluid dynamics techniques for calculating the cooling performance are proposed and discussed. This provides guidelines for selecting the appropriate cooling methods and estimating the performance of them in the early stages of their design.

Having an internal rotor is usually associated with a poor heat transfer due to the airgap acting as an insulating material. Poor heat transfer leads to a loss of electromagnetic performance. A hollow-shaft cooling system as an indirect way of dissipating heat can be employed in order to cool the rotor. On this basis, the HTC of the hollow-shaft rotor cooling for a traction motor is addressed.

Several turbulent flow models are developed in order to give a better understanding of the rotating effect on the flow and to evaluate the convective coefficient. It is concluded that the RST model provides a smaller relative error than the Realizable k-ε and SST k-ω models. The eddy viscosity model based on Boussinesq approximations is less accurate than directly calculating the parameters of the specific Reynolds stress tensors. However, the computational cost of eddy viscosity models is less demanding than a second order closure scheme. The LPTN and FEA model are constructed to represent the heat transfer of the test rig and to help obtain a number of experimental values that are hard to measure.

Through a series of CFD calculations and experiments, it is concluded that the rotational speed of the shaft can significantly enhance the convective HTC of a hollow-

shaft cooling system for both flows. This is explained that a destabilizing effect is generated by the wall rotation. Due to the centrifugal and Coriolis effects, heat transfer is thus promoted by the rotation. However, when the rotational speed increases, the flow seems to be saturated. And the effects of rotation on the heat transfer are weaken for a laminar flow when the rotation speed reaches 30,000 rpm. Furthermore, and first of all, the heat transfer rate is mainly governed by rotation and, secondly, it is almost independent of the inlet flow rate and of the viscosity of coolant. These latter two parameters show a very limited influence on the heat transfer of the cooling method under consideration.

The experimental findings have been summarized in the simple equations (8-1) (8-2). The results are presented in the non-dimensional Reynolds and Nusselt numbers respectively, which can be applied in different geometrical contexts with various axial flow rates and rotating speeds. This can provide the opportunity to optimize the thermal design of machines at an early stage without the need for extensive and costly experimentation.

For Turbulent flow:

$$Nu = (7.438E-03)Re^{0.9082}Pr^{0.4} + (9.183E-05)Re_r^{1.358}Pr^{0.4} \quad (8\text{-}1)$$

where $Pr^{0.4}$ for the heating of the water, 0 < Re_r< 16,890 (0 to 4500 rpm) and 3521 < Re < 10,563 (2 L/min to 7 L/min).

For Laminar flow:

$$Nu = (3.811E-3)(\ Re_r * Pr)^{0.641} \quad (8\text{-}2)$$

where Re< 180 (0 L/min to 7 L/min), Re_r ranging from 2,375 to 1.75e+5 (2000 rpm to 30,000 rpm), Pr varying between 145 and 712 and $Re_r * Pr$ ranging from 1.69e+6 to 2.54e+7.

Finally, the pressure losses distribution across various distances from the shaft entrance, along with a number of different flow patterns, were investigated. For the turbulent flow, the destabilizing effect, which prevails at the entrance to the shaft, leads to an increase in the friction losses due to the excessive external forces within the inner shaft wall. A stabilizing effect becomes dominant at the downstream of the flow,

causing the rotational friction loss to decrease until the flow reaches the steady state and remains substantially unaltered. However, when the flow is discharged from the shaft outlet into the stationary region, the direction of the flow changes abruptly. This causes greater pressure drop at the downstream of the outlet. In addition, for the laminar flow, the rotation has a destabilizing effect throughout the whole length of the shaft and make the flow more turbulent. Furthermore, the shear stress is the highest at the ends of the shaft due to a sudden change of the coolant velocity direction.

The aim of this thesis is to familiarize and equip the electrical machine designers with a concise knowledge of the thermal background to improve upon the overall performance of their products. This provides guidelines for selecting the appropriate cooling methods and estimating the performance of them in the early stages of their design. This thesis for the first time identifies and explains an important relation between the rotation effects and the heat exchange for a hollow-shaft rotor cooling system. This can provide an economical and practical solution to the rotor overheating. In addition, this thesis allows the designers to optimize the thermal design of machines at an early stage without the need for extensive and costly experimentation.

8.2 Further Work

In the future, a highly effective cooling and ventilating system is essential to meet the cooling demands placed on automotive traction motors with both small packaging as well as high torque and high power density. Besides the efficiency of a cooling system in enhancing the electromagnetic performance, the reliability, manufacturing complexity and maintenance costs of any proposed cooling architecture, are amongst the factors that must be considered in the design stage.

Based on the work presented in this thesis, some potential further research areas can be suggested as follows;

Further improvements of test rig and tests:

- The outlet path of oil from the cooled hollow-shaft can be optimised. This can improve the accuracy of the pressure loss measurement.

- The seal friction loss is very large, especially at high speeds. Lower friction rotary shaft seals or another method can be employed in order to supply the coolant to the rotating rotor.
- The maximum rotational speed for water-cooled hollow-shaft cooling is only 4500 rpm. Further work is required to investigate the effects of high speed on the heat transfer coefficient for turbulent flow.
- A static state test for an oil-cooled hollow-shaft have not been conducted. Hence, it is necessary to design a new test rig using resistance wires wound around the shaft to transfer the heat for the static state test.
- For heat transfer analysis of hollow-shaft cooling, the ideal scenario is to create a constant temperature at the inner wall of the shaft to represent a perfect thermal boundary condition. There is still more work to be done, such as evaluating the heat transfer coefficient with a constant temperature of inner wall.
- Technologies such as particle image velocimetry (PIV) and laser Doppler velocimetry (LDA) can be employed to obtain instantaneous velocity of the flow that passes through the hollow-shaft. Visualization experiments can be considered in order to provide visual observations of flow in the rotating shaft. These can provide a clearly path of fluid particles under the effects of rotation.
- Evaluate the effect of channel size on the cooling capacity by taking account the rotor mechanical properties.
- Implement this hollow-shaft rotor cooling system to a motor prototype to test the benefits in terms of intermittent and continuous performance.
- Two correlations obtained in this thesis have boundary constraints and may not be valid for some cases. If possible, a general correlation can be created by conducting more experiments, such as using other types of coolant, testing at broader range of axial flow rates and rotational speeds. As a result, the correlation can be used in a wider range of boundary conditions.

Further numerical and analytical modelling:

- URANS (Unsteady RANS) or Large Eddy Simulation turbulence model can be used to improve the accuracy of the convective heat transfer prediction by using finer modelling techniques.

- The calibration procedure of related parameters using in the CFD models can be performed as part of the investigation in order to improve the accuracy of turbulence models.
- Theoretical analysis can be developed in the future to investigate heat transfer phenomena for turbulent and laminar flows in an axially rotating pipe with uniform heat flux.

9 References

1. *[Online]. Available: https://www.wri.org/resources/data-visualizations/world-greenhouse-gas-emissions-2016*.

2. *CO2 emissions from cars: facts and figures (infographics)*. [Online]. Available https://www.europarl.europa.eu/news/en/headlines/society/20190313STO31218/co2-emissions-from-cars-facts-and-figures-infographics.

3. *[Online]. Available: https://www.gov.uk/government/news/uk-becomes-first-major-economy-to-pass-net-zero-emissions-law*.

4. *US DRIVE Electrical and Electronics Technical Team Roadmap*. 2017: [Online]. Available: https://www.energy.gov/sites/prod/files/2017/11/f39/EETT%20Roadmap%2010-27-17.pdf.

5. UK, A.c., *THE ROADMAP REPORT TOWARDS 2040: A GUIDE TO AUTOMOTIVE PROPULSION TECHNOLOGIES*. The Advanced Propulsion Centre.

6. Zhang, X. and K.S. Haran. *High-specific-power electric machines for electrified transportation applications-technology options*. in *2016 IEEE Energy Conversion Congress and Exposition (ECCE)*. 2016.

7. Montanari, G.C., G. Mazzanti, and L. Simoni, *Progress in electrothermal life modeling of electrical insulation during the last decades.* IEEE Transactions on Dielectrics and Electrical Insulation, 2002. **9**(5): p. 730-745.

8. Huger, D. and D. Gerling. *On the effects of high-temperature-induced aging on electrical machine windings*. in *2015 IEEE International Electric Machines & Drives Conference (IEMDC)*. 2015.

9. Lindner, A., et al. *Measurement of rare earth magnets at high temperatures*. in *2016 International Symposium on Power Electronics, Electrical Drives, Automation and Motion (SPEEDAM)*. 2016.

10. Ruoho, S., et al., *Interdependence of Demagnetization, Loading, and Temperature Rise in a Permanent-Magnet Synchronous Motor.* IEEE Transactions on Magnetics, 2010. **46**(3): p. 949-953.

11. Ayachit, A. and M.K. Kazimierczuk, *Thermal Effects on Inductor Winding Resistance at High Frequencies.* IEEE Magnetics Letters, 2013. **4**: p. 0500304-0500304.

12. Liu, Y., et al., *3D thermal stress analysis of the rotor of an induction motor.* IEEE Transactions on Magnetics, 2000. **36**(4): p. 1394-1397.

13. *[Online]. Available: https://web.archive.org/web/20100705130833/http://www.teslamotors.com:80/roadster/technology/motor . 2010*.

14. Burress, T.A., et al., *Evaluation of the 2010 Toyota Prius Hybrid Synergy Drive System*. 2011, Oak Ridge Nat. Lab., Oak Ridge, TN, USA, Rep. ORNL/TM-2010/253, .

15. Burress, T., *Benchmarking competitive technologies*. presented at the 2012 U.S. Dept. Energy Hydrogen Fuel Cells Program Veh. Technol. Program Annu. Merit Rev. Peer Eval. Meeting, U.S. Department of Energy, MD, USA, 2012.

16. Burress, T., *Benchmarking State-of-the-Art Technologies*. presented at the 2013 U.S. Dept. Energy Hydrogen Fuel Cells Program Veh. Technol. Program Annu. Merit Rev. Peer Eval. Meeting, U.S. Department of Energy, MD, USA, 2013.

17. Burress, T., *Electrical Performance, Reliability Analysis, and Characterization*. presented at the 2017 U.S. Dept. Vehicle Technologies Office Annual Merit Review, U.S. Department of Energy, MD, USA, 2017.

18. Popescu, M., et al., *Modern Heat Extraction Systems for Power Traction Machines-A Review.* IEEE Transactions on Industry Applications, 2016. **52**(3): p. 2167-2175.

19. Nerg, J., M. Rilla, and J. Pyrhonen, *Thermal Analysis of Radial-Flux Electrical Machines With a High Power Density.* IEEE Transactions on Industrial Electronics, 2008. **55**(10): p. 3543-3554.

20. Chong, Y.C., et al. *Thermal design of a magnet-free axial-flux switch reluctance motor for automotive applications*. in *2016 Eleventh International Conference on Ecological Vehicles and Renewable Energies (EVER)*. 2016.

21. Gai, Y., et al. *Shaft cooling and the influence on the electromagnetic performance of traction motors*. in *2017 IEEE International Electric Machines and Drives Conference (IEMDC)*. 2017.

22. Okoro, O.I., *Steady and transient states thermal analysis of a 7.5-kW squirrel-cage induction machine at rated-load operation.* IEEE Transactions on Energy Conversion, 2005. **20**(4): p. 730-736.

23. Tenconi, A., et al., *Temperatures Evaluation in an Integrated Motor Drive for Traction Applications.* IEEE Transactions on Industrial Electronics, 2008. **55**(10): p. 3619-3626.

24. Camilleri, R., et al., *Prediction and Measurement of the Heat Transfer Coefficient in a Direct Oil-Cooled Electrical Machine With Segmented Stator.* IEEE Transactions on Industrial Electronics, 2018. **65**(1): p. 94-102.

25. Mellor, P.H., et al. *Electromagnetic and thermal coupling within a fault-tolerant aircraft propulsion motor*. in *2017 IEEE International Electric Machines and Drives Conference (IEMDC)*. 2017.

26. Bonnett, A.H., *Operating temperature considerations and performance characteristics for IEEE 841 motors.* IEEE Transactions on Industry Applications, 2001. **37**(4): p. 1120-1131.

27. Albers, T. and A.H. Bonnett, *Motor temperature considerations for pulp and paper mill applications.* IEEE Transactions on Industry Applications, 2002. **38**(6): p. 1701-1713.

28. Bellettre, J., et al., *Transient state study of electric motor heating and phase change solid-liquid cooling.* Applied Thermal Engineering, 1997. **17**(1): p. 17-31.

29. Bennion, K., *Electric Motor Thermal Management R&D* April. 2016, NREL., Golden, CO, USA,.

30. Pechánek, R. and L. Bouzek. *Analyzing of two types water cooling electric motors using computational fluid dynamics*. in *2012 15th International Power Electronics and Motion Control Conference (EPE/PEMC)*. 2012.

31. El-Refaie, A.M., et al., *Advanced High-Power-Density Interior Permanent Magnet Motor for Traction Applications.* IEEE Transactions on Industry Applications, 2014. **50**(5): p. 3235-3248.

32. Zhang, B., et al., *Thermal Model of Totally Enclosed Water-Cooled Permanent-Magnet Synchronous Machines for Electric Vehicle Application.* IEEE Transactions on Industry Applications, 2015. **51**(4): p. 3020-3029.

33. Dorrell, D.G., et al., *A Review of the Design Issues and Techniques for Radial-Flux Brushless Surface and Internal Rare-Earth Permanent-Magnet Motors.* IEEE Transactions on Industrial Electronics, 2011. **58**(9): p. 3741-3757.

34. Polikarpova, M., *Liquid cooling solutions for rotating permanent magnet synchronous machines*, in *Dep. Mech. Eng.* 2014, Lappeenranta University of Technology: Lappeenranta, Finland.

35. Soong, W.L., *Sizing of electrical machines.* Power Eng. Briefing Note Ser., 2008. **9**: p. 17-18.

36. Staton, D.A. and A. Cavagnino, *Convection Heat Transfer and Flow Calculations Suitable for Electric Machines Thermal Models.* IEEE Transactions on Industrial Electronics, 2008. **55**(10): p. 3509-3516.

37. Huang, X., et al. *A Brushless DC motor design for an aircraft electro-hydraulic actuation system*. in *2011 IEEE International Electric Machines & Drives Conference (IEMDC)*. 2011.

38. Valenzuela, M.A. and J.A. Tapia, *Heat Transfer and Thermal Design of Finned Frames for TEFC Variable-Speed Motors.* IEEE Transactions on Industrial Electronics, 2008. **55**(10): p. 3500-3508.

39. Gilson, G.M., et al. *A combined electromagnetic and thermal optimisation of an aerospace electric motor*. in *2010 XIX International Conference on Electrical Machines (ICEM)*. 2010.

40. Güvenç, A. and H. Yüncü, *An experimental investigation on performance of fins on a horizontal base in free convection heat transfer.* Heat and Mass Transfer, 2001. **37**(4): p. 409-416.

41. Pol, D.V.d. and J. Tierney, *Free Convection Heat Transfer from Vertical Fin-Arrays.* IEEE Transactions on Parts, Hybrids, and Packaging, 1974. **10**(4): p. 267-271.

42. Jones, C.D. and L.F. Smith, *Optimum Arrangement of Rectangular Fins on Horizontal Surfaces for Free-Convection Heat Transfer.* Journal of Heat Transfer, 1970. **92**(1): p. 6-10.

43. Ulbrich, S., J. Kopte, and J. Proske, *Cooling fin optimization on a TEFC electrical machine housing using a 2D conjugate heat transfer model.* IEEE Transactions on Industrial Electronics, 2017.

44. Staton, D.A. and E. So. *Determination of optimal thermal parameters for brushless permanent magnet motor design*. in *Thirty-Third IAS Annual Meeting* 1998.

45. Mizuno, S., et al., *Development of a Totally Enclosed Fan-Cooled Traction Motor.* IEEE Transactions on Industry Applications, 2013. **49**(4): p. 1508-1514.

46. Herbert, W.A., *Totally Enclosed Fan-Cooled Squirrel-Cage Induction Motor Options.* IEEE Transactions on Industry Applications, 2014. **50**(2): p. 1590-1598.

47. Lahne, H.C., et al. *Design of a 50000 rpm high-speed high-power six-phase PMSM for use in aircraft applications*. in *2016 Eleventh International Conference on Ecological Vehicles and Renewable Energies (EVER)*. 2016.

48. Yung, C. *Cool facts about cooling electric motors*. in *Industry Applications Society 60th Annual Petroleum and Chemical Industry Conference*. 2013.

49. Stone, G.C., et al., *Electrical Insulation for Rotating Machines: Design, Evaluation, Aging, Testing, and Repair*. 2014: Wiley.

50. Kung, L., et al. *Improvement of the cooling performance of symmetrically self-ventilated induction machines in the 2-15 MW range*. in *2001 IEEE International Electric Machines and Drives Conference (IEMDC)*. 2001.

51. Nakahama, T., et al., *Improved cooling performance of large motors using fans.* IEEE Transactions on Energy Conversion, 2006. **21**(2): p. 324-331.

52. Nakahama, T., et al., *Effects of Fan Blade Forward-Swept and Inclined Amounts in Electric Motors.* IEEE Transactions on Energy Conversion, 2010. **25**(2): p. 457-464.

53. Bamberger, K. and T. Carolus, *Optimization of axial fans with highly swept blades with respect to losses and noise reduction.* Noise Control Engineering Journal, 2012. **60**: p. 716-725.

54. Yung, C., *Cool Facts About Cooling Electric Motors: Improvements in Applications That Fall Outside the Normal Operating Conditions.* IEEE Industry Applications Magazine, 2015. **21**(6): p. 47-56.

55. Chong, Y.C., *Thermal Analysis and Air Flow Modelling of Electrical Machines*, in *Dep. Mech. Eng.* 2015, Edinburgh Univ.: Edinburgh,UK.

56. Seshagiri-rao, G.V.R. and V.V. Subba-rao, *Design of cooling fan for noise reduction using CFD.* International Journal of Scientific & Engineering Research, 2011. **2**(9): p. 1-5.

57. Krishna, S.R., A.R. Krishna, and K. Ramji, *An experimental study on the reduction of motor-fan noise by modification of the blade and shroud configuration.* Mechanical Engineering Science, 2009. **224**: p. 315-320.

58. Cattanei, R.G. A., and A. Bongiovı, *Reduction of the tonal noise annoyance of axial flow fans by means of optimal blade spacing.* Applied Acoustics, 2007. **68**(11-12): p. 1323-1345.

59. Lezhi, Y., et al., *Design and Performance of a Water-cooled Permanent Magnet Retarder for Heavy Vehicles.* IEEE Transactions on Energy Conversion, 2011. **26**(3): p. 953-958.

60. Kral, C., A. Haumer, and T. Bauml, *Thermal Model and Behavior of a Totally-Enclosed-Water-Cooled Squirrel-Cage Induction Machine for Traction Applications.* IEEE Transactions on Industrial Electronics, 2008. **55**(10): p. 3555-3565.

61. Jiang, W. and T.M. Jahns, *Coupled Electromagnetic–Thermal Analysis of Electric Machines Including Transient Operation Based on Finite-Element Techniques.* IEEE Transactions on Industry Applications, 2015. **51**(2): p. 1880-1889.

62. Kulkarni, D.P., G. Rupertus, and E. Chen, *Experimental Investigation of Contact Resistance for Water Cooled Jacket for Electric Motors and Generators.* IEEE Transactions on Energy Conversion, 2012. **27**(1): p. 204-210.

63. Kimiabeigi, M., et al., *High-Performance Low-Cost Electric Motor for Electric Vehicles Using Ferrite Magnets.* IEEE Transactions on Industrial Electronics, 2016. **63**(1): p. 113-122.

64. Nategh, S., et al., *Thermal Modeling of Directly Cooled Electric Machines Using Lumped Parameter and Limited CFD Analysis.* IEEE Transactions on Energy Conversion, 2013. **28**(4): p. 979-990.

65. Huang, Z., et al. *Direct oil cooling of traction motors in hybrid drives*. in *2012 IEEE International Electric Vehicle Conference (IEVC)*. 2012.

66. Lu, Q., et al., *Modeling and Investigation of Thermal Characteristics of a Water-Cooled Permanent-Magnet Linear Motor.* IEEE Transactions on Industry Applications, 2015. **51**(3): p. 2086-2096.

67. Zheng, P., et al., *Research on the Cooling System of a 4QT Prototype Machine Used for HEV.* IEEE Transactions on Energy Conversion, 2008. **23**(1): p. 61-67.

68. Sikora, M., R. Vlach, and B. Navr´atil, *The Unusual Water Cooling Applied on Small Asynchronous Motor.* Engineering Mechanics 2011. **18**(2): p. 143-153.

69. Zhang, B., et al., *Development of a Yokeless and Segmented Armature Axial Flux Machine.* IEEE Transactions on Industrial Electronics, 2016. **63**(4): p. 2062-2071.

70. Arbab, N., et al., *Thermal Modeling and Analysis of a Double-Stator Switched Reluctance Motor.* IEEE Transactions on Energy Conversion, 2015. **30**(3): p. 1209-1217.

71. Semidey, S.A. and J.R. Mayor, *Experimentation of an Electric Machine Technology Demonstrator Incorporating Direct Winding Heat Exchangers.* IEEE Transactions on Industrial Electronics, 2014. **61**(10): p. 5771-5778.

72. Schiefer, M. and M. Doppelbauer. *Indirect slot cooling for high-power-density machines with concentrated winding*. in *2015 IEEE International Electric Machines & Drives Conference (IEMDC)*. 2015.

73. Lindh, P., et al., *Direct Liquid Cooling Method Verified With an Axial-Flux Permanent-Magnet Traction Machine Prototype.* IEEE Transactions on Industrial Electronics, 2017. **64**(8): p. 6086-6095.

74. Kimiabeigi, M., *Wind turbine generator and method of assembly of a wind turbine generator*. Jan.4, 2012.

75. Kimiabeigi, M. and J.L. Besnerais, *Generator, in particular for a wind turbine*. 2011.

76. Ponomarev, P., M. Polikarpova, and J. Pyrhönen. *Thermal modeling of directly-oil-cooled permanent magnet synchronous machine*. in *2012 XXth International Conference on Electrical Machines (ICEM)*. 2012.

77. La Rocca, A., *Thermal analysis of a high speed electrical machine*, in *Dept. Elect. Eng.* 2016, Nottingham Univ.: Nottingham,UK.

78. Tüysüz, A., et al., *Advanced Cooling Methods for High-Speed Electrical Machines.* IEEE Transactions on Industry Applications, 2017. **53**(3): p. 2077-2087.

79. Gai, Y., et al. *Power Losses and Thermal Analysis of a Hollow-Shaft Rotor Cooling System*. in *2019 22nd International Conference on Electrical Machines and Systems (ICEMS)*. 2019.

80. Gai, Y., et al. *Pressure Loss Modelling in a Water-Cooled Hollow-Shaft Rotor for an Automotive Traction Motor*. in *2018 XIII International Conference on Electrical Machines (ICEM)*. 2018.

81. Gai, Y., et al., *Cooling of Automotive Traction Motors: Schemes, Examples, and Computation Methods.* IEEE Transactions on Industrial Electronics, 2019. **66**(3): p. 1681-1692.

82. Gai, Y., et al., *On the Measurement and Modeling of the Heat Transfer Coefficient of a Hollow-Shaft Rotary Cooling System for a Traction Motor.* IEEE Transactions on Industry Applications, 2018. **54**(6): p. 5978-5987.

83. Gai, Y., et al., *Numerical and Experimental Calculation of CHTC in an Oil-Based Shaft Cooling System for a High-Speed High-Power PMSM.* IEEE Transactions on Industrial Electronics, 2020. **67**(6): p. 4371-4380.

84. Seghir-Ouali, S., et al., *Convective heat transfer inside a rotating cylinder with an axial air flow.* International Journal of Thermal Sciences, 2006. **45**(12): p. 1166-1178.

85. Costa-Patry, E., *Cooling High Heat Flux Micro-Electronic Systems using Refrigerants in High Aspect Ratio Multi-Microchannel Evaporators*, in *Dept. Elect. Eng*. 2011, EPFL Univ: Lausanne,Switzerland.

86. Zhenguo, L. and R. Lin. *Optimization design of the spray evaporative-cooling large electrical machine*. in *2016 19th International Conference on Electrical Machines and Systems (ICEMS)*. 2016.

87. Zhenguo, L., R. Lin, and T. Longyao. *Heat transfer characteristics of spray evaporative cooling system for large electrical machines*. in *2015 18th International Conference on Electrical Machines and Systems (ICEMS)*. 2015.

88. Li, Z., et al. *Study on spraying evaporative cooling technology for the large electrical machine*. in *2009 International Conference on Electrical Machines and Systems*. 2009.

89. Shedd, T.A., *Next Generation Spray Cooling: High Heat Flux Management in Compact Spaces.* Heat Transfer Engineering, 2007. **28**(2): p. 87-92.

90. Womac, D.J., S. Ramadhyani, and F.P. Incropera, *Correlating Equations for Impingement Cooling of Small Heat Sources With Single Circular Liquid Jets.* Journal of Heat Transfer, 1993. **115**(1): p. 106-115.

91. Ludois, D.C. and I. Brown, *Brushless and Permanent Magnet Free Wound Field Synchronous Motors for EV Traction*. 2017, ; Univ. of Wisconsin-Madison, Madison, WI (United States). p. Medium: ED; Size: 51 p.

92. Mitcham, A.J. and J.J.A. Cullen. *Permanent magnet generator options for the More Electric Aircraft*. in *2002 International Conference on Power Electronics, Machines and Drives*. 2002.

93. Fedoseyev, L. and E.M. Pearce, *Rotor Assembly with Heat Pipe Cooling System*. Dec. 18, 2014.

94. *[Online]. Avaliable: http://www.zytekautomotive.co.uk*.

95. *BU HEV Electrical Traction Drives: HEV E-Drive Development and Products*. 2012: Gifhorn, [Online]. Available: https://docplayer.net/8379513-Bu-hev-electrical-traction-drives-hev-e-drive-development-and-products-gifhorn-29-11-2012.html

96. Popescu, M., et al., *Electrical Vehicles—Practical Solutions for Power Traction Motor Systems.* IEEE Transactions on Industry Applications, 2018. **54**(3): p. 2751-2762.

97. Grunditz, E.A. and T. Thiringer, *Performance Analysis of Current BEVs Based on a Comprehensive Review of Specifications.* IEEE Transactions on Transportation Electrification, 2016. **2**(3): p. 270-289.

98. *Technical specifications of the BMW i3 (120 Ah)*, www.press.bmwgroup.com/global/article/detail/T0285608EN/technical-specifications-of-the-bmw-i3-120-ah-and-the-bmw-i3s-120-ah-valid-from-11/2018?language=en, Editor.

99. Mellor, P.H., D. Roberts, and D.R. Turner, *Lumped parameter thermal model for electrical machines of TEFC design.* IEE Proceedings B - Electric Power Applications, 1991. **138**(5): p. 205-218.

100. Vlach, R., R. Grepl, and P. Krejci. *Control of Stator Winding Slot Cooling by Water Using Prediction of Heating*. in *2007 IEEE International Conference on Mechatronics*. 2007.

101. Bumby, J.R. and R. Martin, *Axial-flux permanent-magnet air-cored generator for small-scale wind turbines.* IEE Proceedings - Electric Power Applications, 2005. **152**(5): p. 1065-1075.

102. Douglas, J.F., G. J.M., and S. J.A., *Fluid Mechanics*, ed. r. ed. 1995, Singapore: Longman.

103. Murakami, M. and K. Kikuyama, *Turbulent Flow in Axially Rotating Pipes.* Journal of Fluids Engineering, 1980. **102**(97): p. 97-103.

104. Yamada, Y., *Resistance of a Flow through an Annulus with an Inner Rotating Cylinder.* Bulletin of JSME, 1962. **5**(18): p. 302-310.

105. Johnson, A.R. and W.D. Morris, *An experimental investigation into the effects of rotation on the isothermal flow resistance in circular tubes rotating about a parallel axis.* International Journal of Heat and Fluid Flow, 1992. **13**(2): p. 132-140.

106. Chong, Y.C., et al., *An experimental study of rotational pressure loss in rotor-stator gap.* Propulsion and Power Research, 2017. **6**(2): p. 147-156.

107. Chong, Y.C., et al. *An experimental study of rotational pressure loss in rotor ducts*. in *14th UK Heat Transfer Conference*. 2015. Edinburgh.

108. Harahap, F. and J.H.N. McManus, *Natural Convection Heat Transfer From Horizontal Rectangular Fin Arrays.* Journal of Heat Transfer, 1967. **89**(1): p. 32-38.

109. Volker, G., *New Equations for Heat and Mass Transfer in Turbulent Pipe and Channel Flow.* NASA STI/Recon Technical Report 1976. **41**: p. 8-16.

110. Arslan, G. and M. Özdemir, *Correlation to predict heat transfer of an oscillating loop heat pipe consisting of three interconnected columns.* Energy Conversion and Management, 2008. **49**(8): p. 2337-2344.

111. Boglietti, A., et al., *Evolution and Modern Approaches for Thermal Analysis of Electrical Machines.* IEEE Transactions on Industrial Electronics, 2009. **56**(3): p. 871-882.

112. Airoldi, G., et al. *Computations on heat transfer in axial flux permanent magnet machines*. in *2008 18th International Conference on Electrical Machines*. 2008.

113. SanAndres, U., et al., *Design of Cooling Systems Using Computational Fluid Dynamics and Analytical Thermal Models.* IEEE Transactions on Industrial Electronics, 2014. **61**(8): p. 4383-4391.

114. Nachouane, A.B., et al., *Numerical Study of Convective Heat Transfer in the End Regions of a Totally Enclosed Permanent Magnet Synchronous Machine.* IEEE Transactions on Industry Applications, 2017. **53**(4): p. 3538-3547.

115. Fawzal, A.S., et al., *Fan Performance Analysis for Rotor Cooling of Axial Flux Permanent Magnet Machines.* IEEE Transactions on Industry Applications, 2017. **53**(4): p. 3295-3304.

116. Wang, W., et al., *Numerical investigation of tube-side fully developed turbulent flow and heat transfer in outward corrugated tubes.* International Journal of Heat and Mass Transfer, 2018. **116**: p. 115-126.

117. *User Guide STAR-CCM + Version 10.06*. CD-adapco, Melville, NY, USA, 2015.

118. Reich, G. and H. Beer, *Fluid flow and heat transfer in an axially rotating pipe—I. Effect of rotation on turbulent pipe flow.* International Journal of Heat and Mass Transfer, 1989. **32**(3): p. 551-562.

119. Reich, G., B. Weigand, and H. Beer, *Fluid flow and heat transfer in an axially rotating pipe-II. Effect of rotation on laminar pipe flow.* Heat and Mass Transfer, 1989. **32**(3): p. 563-574.

120. Kikuyama, K., M. Murakami, and K. Nishibori, *Development of Three-Dimensional Turbulent Boundary Layer in an Axially Rotating Pipe.* Journal of Fluids Engineering, 1983. **105**(2): p. 154-160.

121. Pickering, S.J., D. Lampard, and M. Shanel. *Modelling ventilation and cooling of the rotors of salient pole machines*. in *2001 IEEE InternationalElectric Machines and Drives Conference (IEMDC)* 2001.

122. Dang, D.D., et al., *CFD analysis of turbulent convective heat transfer in a hydro-generator rotor-stator system.* Applied Thermal Engineering, 2018. **130**: p. 17-28.

123. Carew, N.J. *Experimental determination of heat transfer co-efficients of salient pole rotors*. in *IEE Colloquium on Thermal Aspects of Machines*. 1992.

124. *[Online]. Available: http://www.adapted-solutions.com/web/adaptedsolutionsenglish/ASProductPortunus.html .2016*.

125. Reynolds, O., *On the Dynamical Theory of Incompressible Viscous Fluids and the Determination of the Criterion.* Philosophical Transactions of the Royal Society of London, 1895. **186**: p. 123-164.

126. Tennekes, H. and J.L. Lumley, *A first course in turbulence*, ed. p. ed. 1992, Cambridge: Mass.

127. Anderson, J.D., *Governing Equations of Fluid Dynamics*, in *Computational Fluid Dynamics*, J.F. Wendt, Editor. 2009, Springer Berlin Heidelberg: Berlin, Heidelberg. p. 15-51.

128. Shih, T.-H., et al., *A New K-epsilon Eddy Viscosity Model for High Reynolds Number Turbulent Flows: Model Development and Validation*. 1994, NASA Lewis Research Center: Cleveland, OH, United States

129. Rodi, W., *Experience with two-layer models combining the k-epsilon model with a one-equation model near the wall*, in *29th Aerospace Sciences Meeting*. 1991, American Institute of Aeronautics and Astronautics.

130. Wilcox, D.C., *Turbulence Modeling for CFD*, ed. n. edition. 1998, DCW Industries, Inc.

131. Menter, F.R., *Two-equation eddy-viscosity turbulence modeling for engineering applications.* AIAA Journal, 1994. **32**(8): p. 1598-1605.

132. Karman, T.v., *Mechanical Similitude and Turbulence.* Tech. Mem. NACA, 1931. **5**(611): p. 58-76.

133. Wu, D., et al., *A new transient CFD method for determining the dynamic coefficients of liquid annular seals.* Journal of Mechanical Science and Technology, 2016. **30**(8): p. 3477-3486.

134. Jungreuthmayer, C., et al., *A Detailed Heat and Fluid Flow Analysis of an Internal Permanent Magnet Synchronous Machine by Means of Computational Fluid Dynamics.* IEEE Transactions on Industrial Electronics, 2012. **59**(12): p. 4568-4578.

135. Huang, Z., et al., *Loss Calculation and Thermal Analysis of Rotors Supported by Active Magnetic Bearings for High-Speed Permanent-Magnet Electrical Machines.* IEEE Transactions on Industrial Electronics, 2016. **63**(4): p. 2027-2035.

136. *[Online]. Available: https://www.adapted-solutions.com/en/produkte-2/portunus/*.

137. *[Online]. Available: http://www.skf.com/uk/products/bearings-units-housings/principles/bearing-selection-process/operating-temperature-and-speed/friction-powerloss-startingtorque/index.html*.

138. J.Saari, *Thermal analysis of high-speed induction machines*, in *Dept. Elect. Commun. Eng.* 1998, Helsinki Univ. Technol.: Espoo, Finland.

139. Liu, Y., et al., *Application of an Amorphous Core to an Ultra-high-speed Sleeve-free Interior Permanent-magnet Rotor.* IEEE Transactions on Industrial Electronics, 2018. **PP**(99): p. 1-1.

140. *[Online]. Available: https://bearinx-online-easy-friction.schaeffler.com . 2018*.

141. Howey, D.A., P.R.N. Childs, and A.S. Holmes, *Air-Gap Convection in Rotating Electrical Machines.* IEEE Transactions on Industrial Electronics, 2012. **59**(3): p. 1367-1375.

142. Ma, C., et al., *Thermal characteristics analysis and experimental study on the high-speed spindle system.* The International Journal of Advanced Manufacturing Technology, 2015. **79**(1): p. 469-489.

143. Staton, D., A. Boglietti, and A. Cavagnino, *Solving the More Difficult Aspects of Electric Motor Thermal Analysis in Small and Medium Size Industrial Induction Motors.* IEEE Transactions on Energy Conversion, 2005. **20**(3): p. 620-628.

144. Camilleri, R., D.A. Howey, and M.D. McCulloch, *Predicting the Temperature and Flow Distribution in a Direct Oil-Cooled Electrical Machine With Segmented Stator.* IEEE Transactions on Industrial Electronics, 2016. **63**(1): p. 82-91.

145. *http://www.motor-design.com*.

146. A.White, *Flow of A Fluid in an Axially Rotating Pipe.* Journal Mechanical Engineering Science 1964. **6**(1).

147. Imao, S., Q. Zhang, and Y. Tamada, *The laminar flow in the developing region of a rotating pipe.* Bulletin of JSME, 1989. **32**: p. 317-323.

148. Kikuyama, K., et al., *Flow in an Axially Rotating Pipe : A calculation of flow in the saturated region.* Bulletin of JSME, 1983. **26**(214): p. 506-513.

149. Chong, Y.C., et al., *Pressure loss measurement in rotor-stator gap of radial flux electrical machines*, in *2014 International Conference on Electrical Machines (ICEM)*. Berlin, Germany, 2014.

150. Bui, B.T., *Modeling the Effect of Pipe Rotation on Pressure Loss Through Tool Joint*, in *SPETT 2012 Energy Conference and Exhibition*. 2012, Society of Petroleum Engineers: Port-of-Spain, Trinidad.

151. Idelchik, I.E., *Handbook of Hydraulic Resistance*, ed. t. edition. 2007: Redding: BegellHouse, Inc.

Appendix A Mesh Dependency Study

In this thesis, the CFD models were developed to predict the HTC and the pressure losses of the hollow-shaft rotor cooling system. A high velocity gradient in the tangential direction occurs as a result of the shaft rotation. Consequently, mesh refinement study is performed for the maximum rotational speed for different CFD models in order to ensure sufficient number of computational cells that are allocated for the qualitative CFD analysis. The mesh size set at 2 mm was also used for the developed CFD models. Four different mesh sizes were run on a single problem; one is finer (1 mm) than the mesh used to obtain the CFD results, but other two are coarser (3 mm and 4 mm).

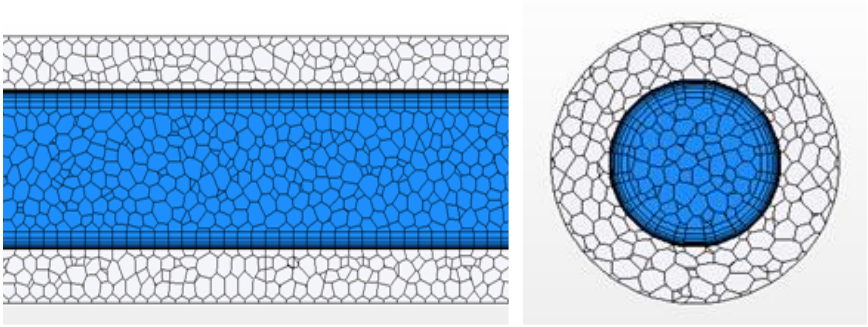

(a) Mesh size = 4 mm

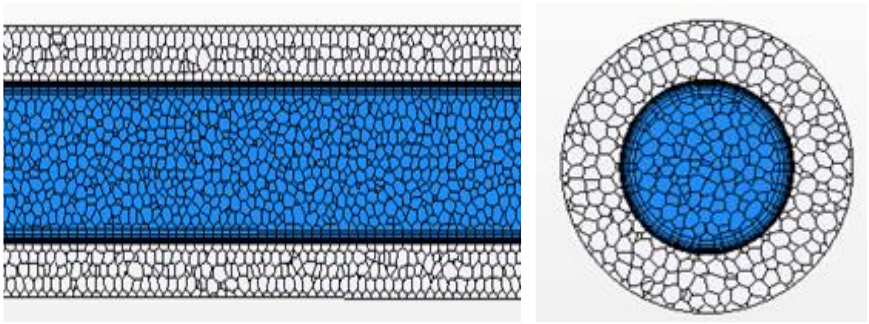

(b) Mesh size = 3 mm

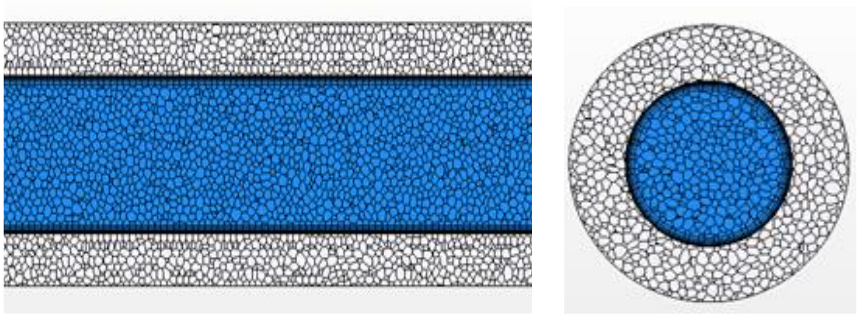

(c) Mesh size = 2 mm

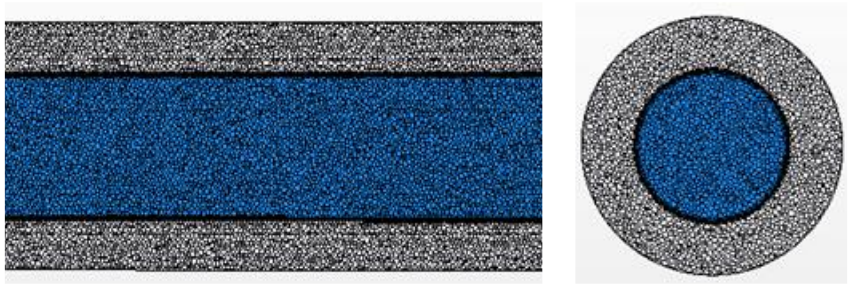

(d) Mesh size = 1 mm

Fig. Appendix A-1. The mesh size in the CFD models.

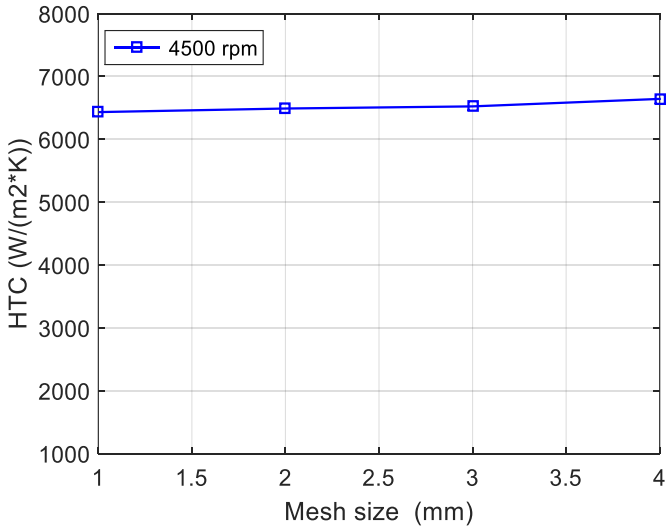

Fig. Appendix A-2. The variation of HTC with mesh size for water-cooled hollow-shaft cooling at 4500 rpm.

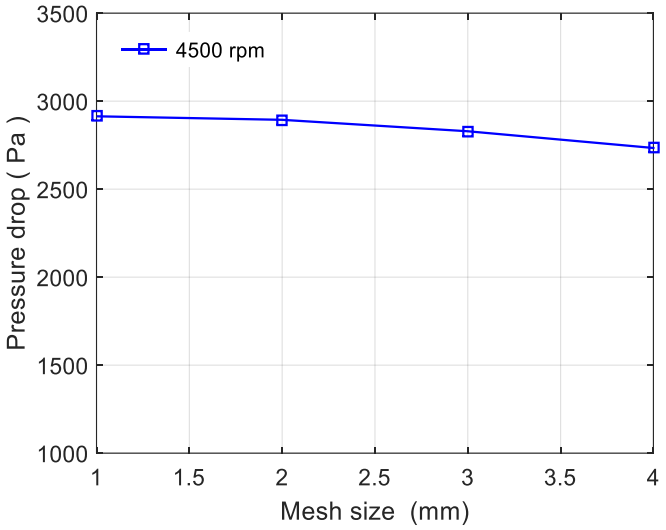

Fig. Appendix A-3. The variation of pressure drop with mesh size for water-cooled hollow-shaft cooling at 4500 rpm.

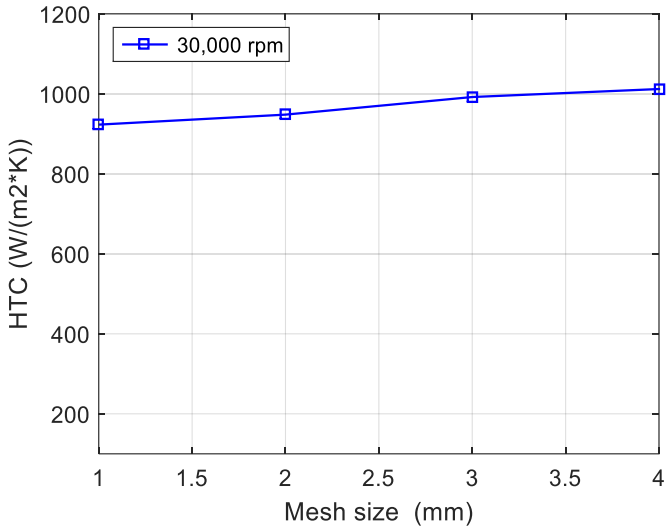

Fig. Appendix A-4. The variation of HTC with mesh size for oil-cooled hollow-shaft cooling at 30,000 rpm.

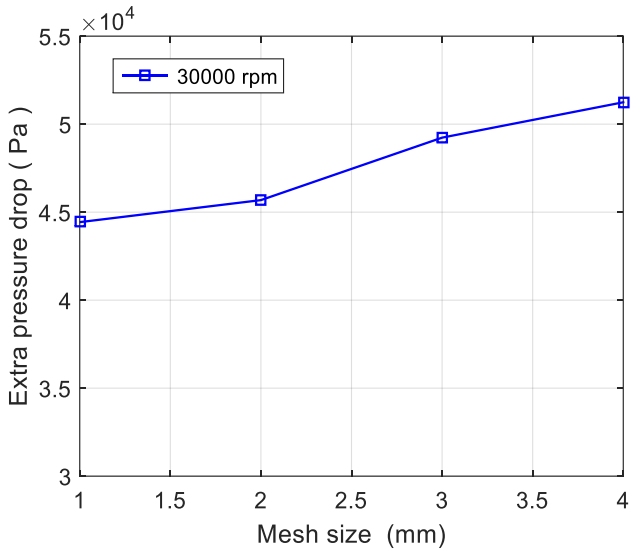

Fig. Appendix A-5. The variation of extra pressure drop with mesh size for oil-cooled hollow-shaft cooling at 30,000 rpm.

Appendix B Drawing

This appendix provides drawings of the key active components of the oil-cooled hollow-shaft test rig.

B.1. Housing.

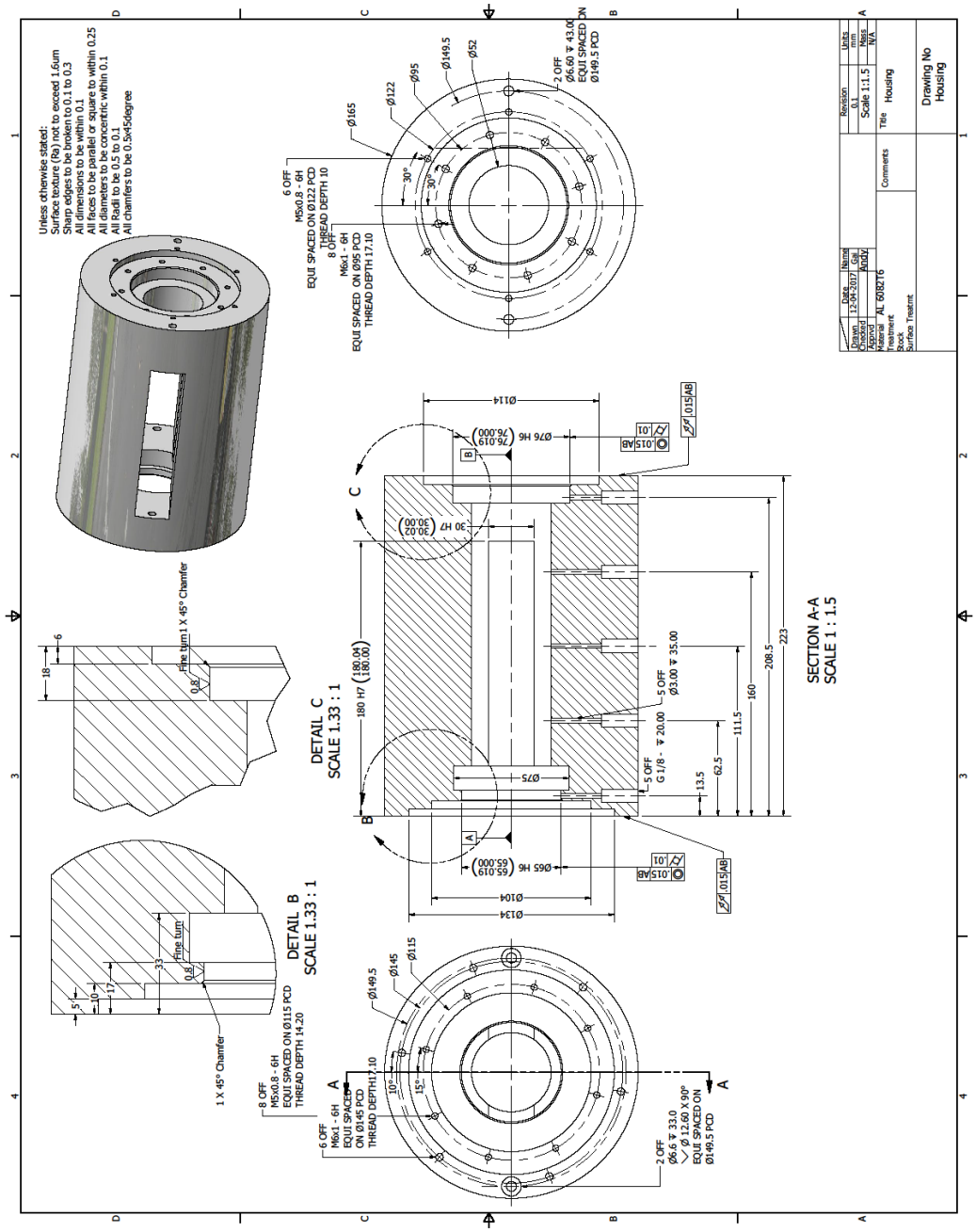

B.2. Oil Collecting Housing.

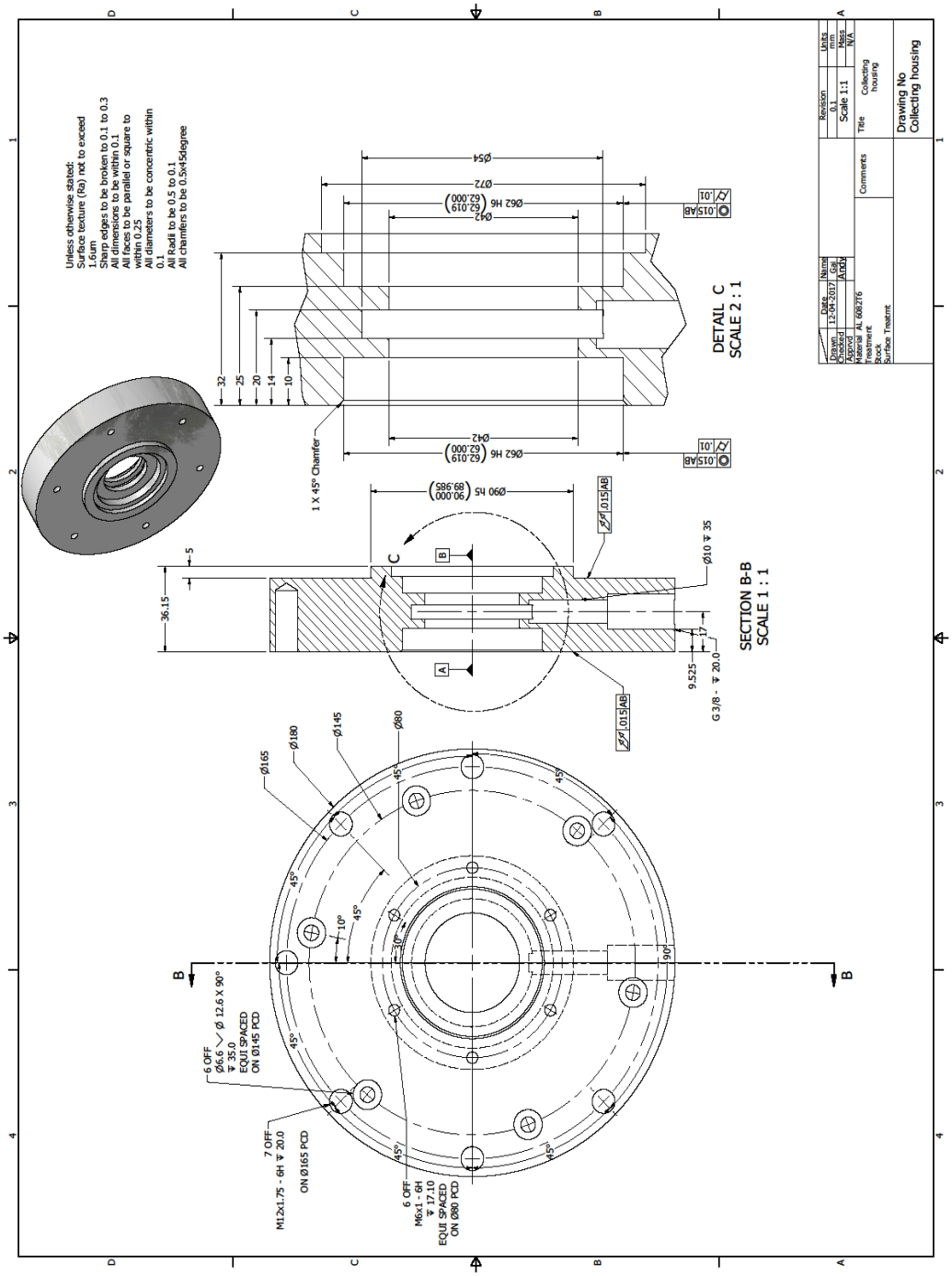

B.3. Seal Holder.

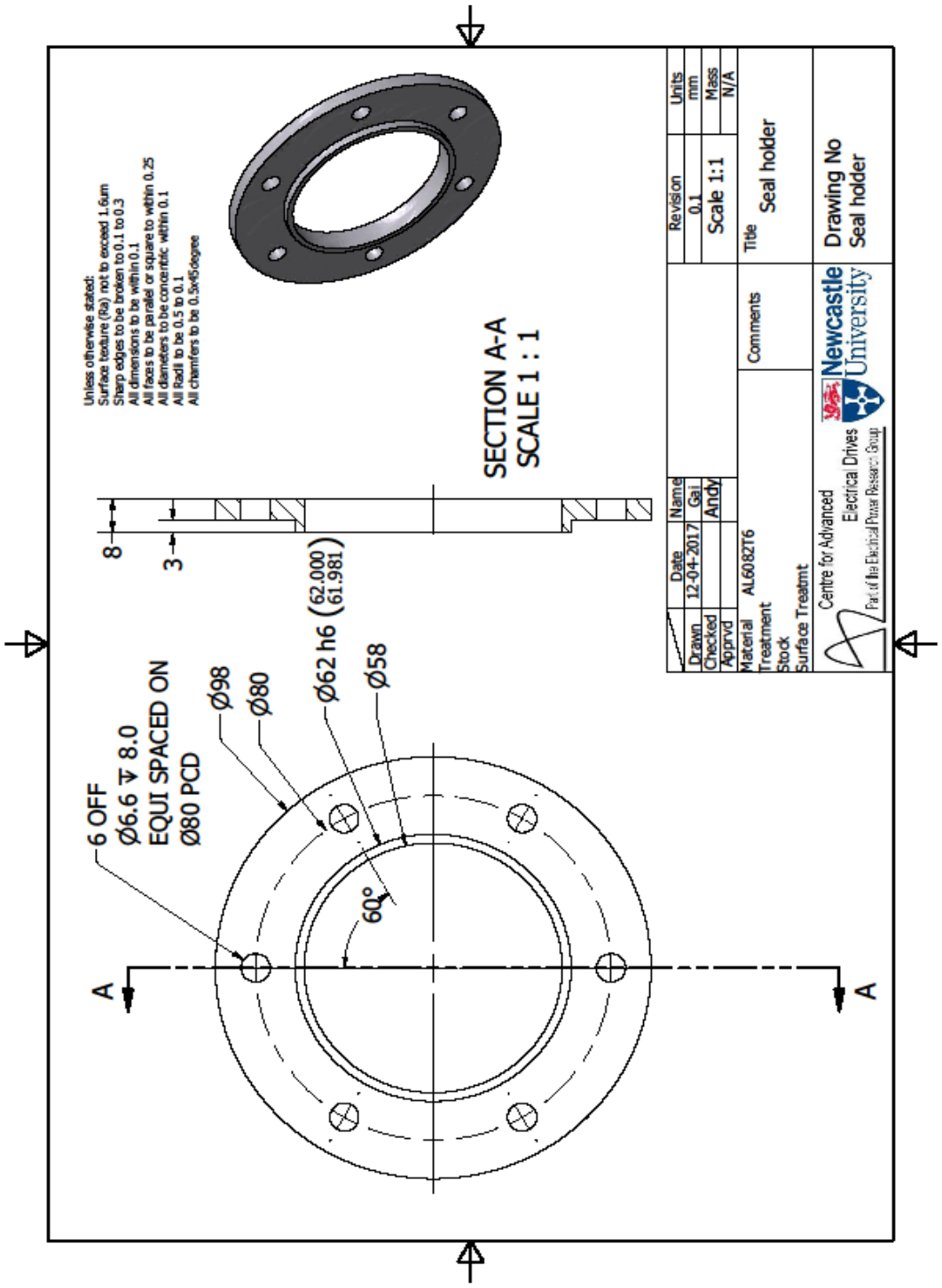

B.4. Rig Yoke.

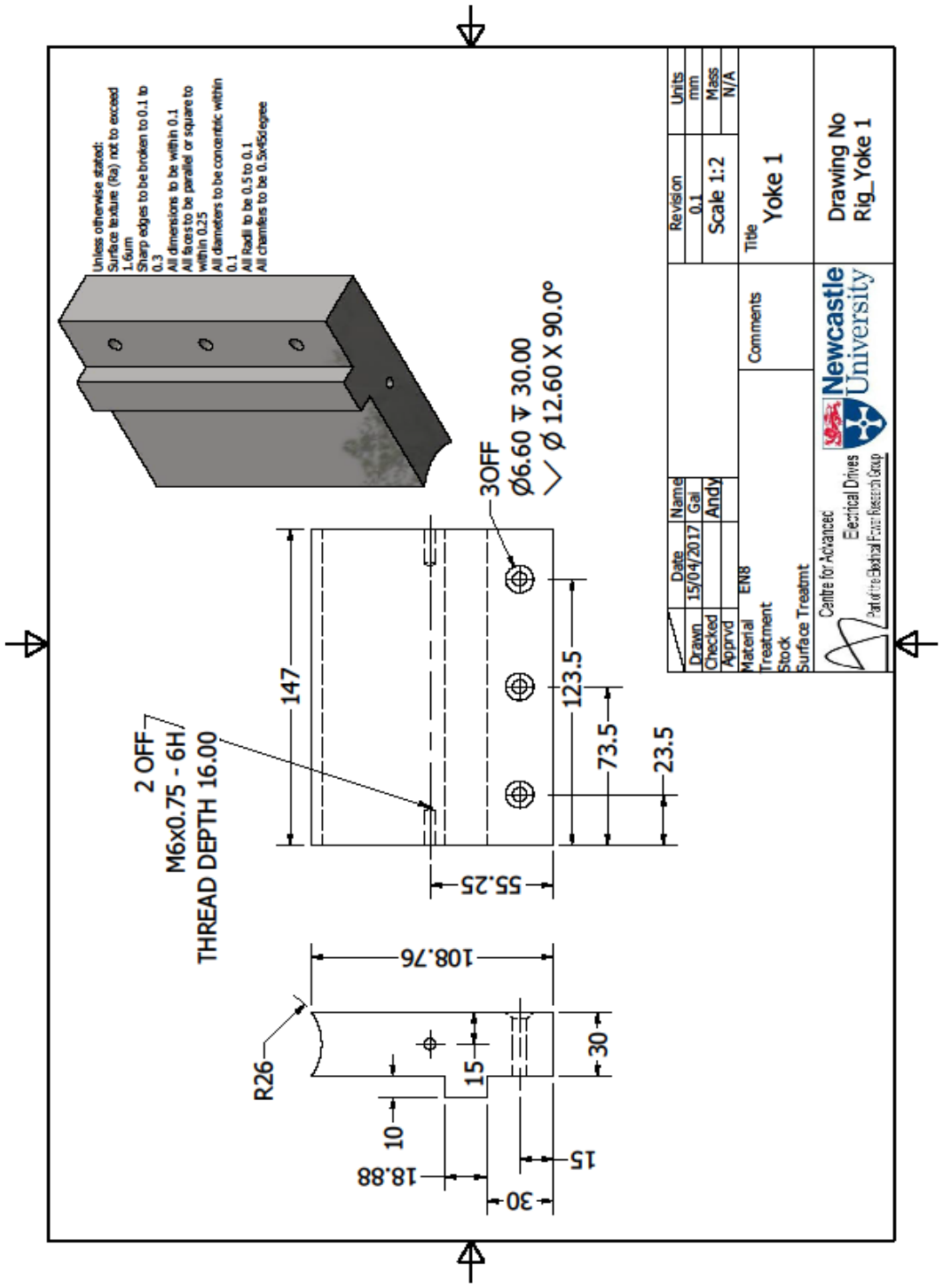
Unless otherwise stated:
Surface texture (Ra) not to exceed 1.6um
Sharp edges to be broken to 0.1 to 0.3
All dimensions to be within 0.1
All faces to be parallel or square to within 0.25
All diameters to be concentric within 0.1
All Radii to be 0.5 to 0.1
All chamfers to be 0.5x45degree
3OFF
Ø6.60 ↧ 30.00
⌵ Ø 12.60 X 90.0°
2 OFF
M6x0.75 - 6H
THREAD DEPTH 16.00
147
123.5
73.5
23.5
55.25
108.76
R26
15
30
10
18.88
15
30
Drawn
Checked
Apprvd
Material
Treatment
Stock
Surface Treatmt
Date
15/04/2017
Name
Gal
Andy
EN8
Comments
Revision
0.1
Scale 1:2
Units
mm
Mass
N/A
Title
Yoke 1
Drawing No
Rig_Yoke 1
Newcastle University
Centre for Advanced Electrical Drives
Part of the Electrical Power Research Group

B.5. Rig Yoke2.

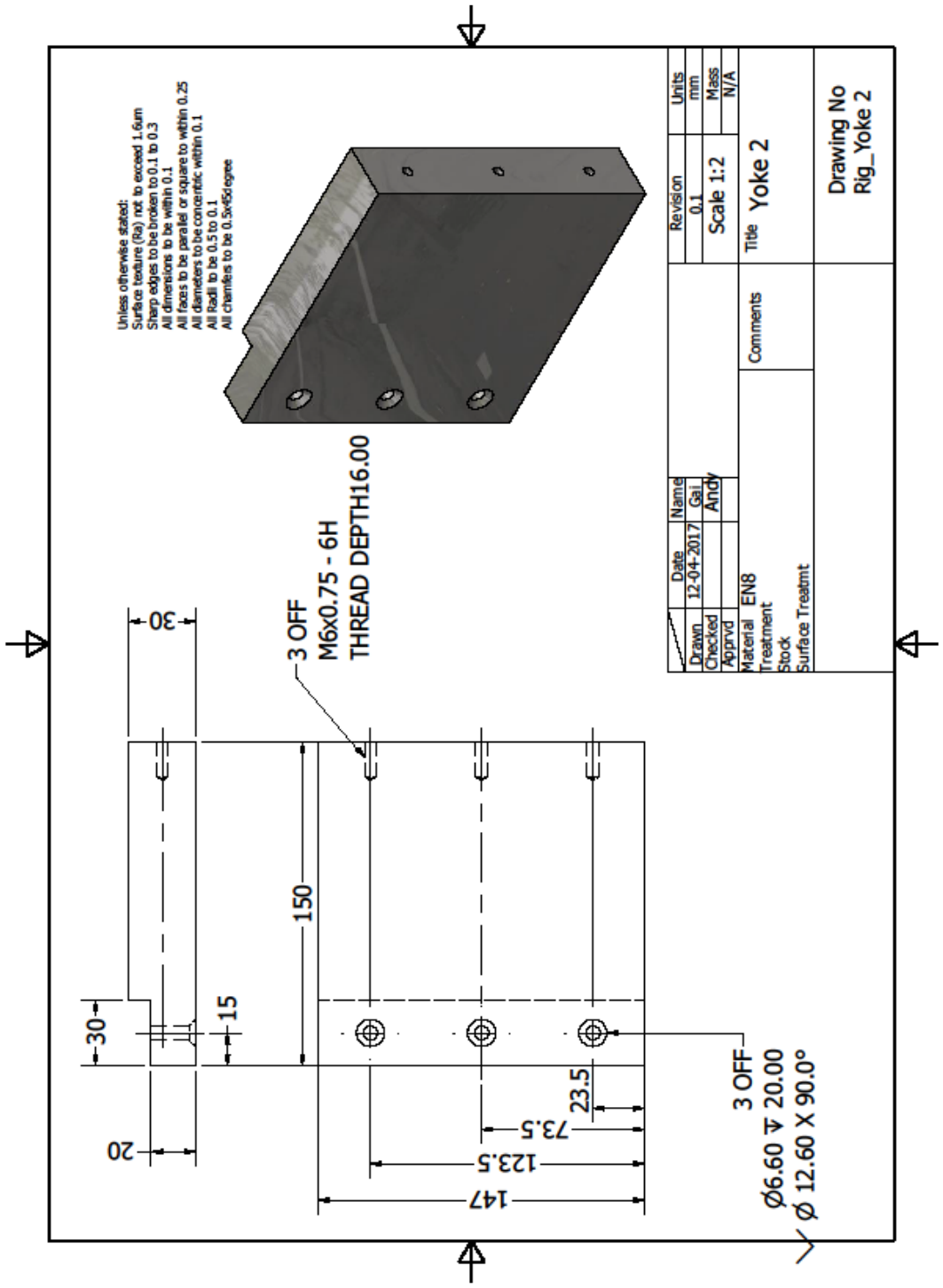
Unless otherwise stated:
Surface texture (Ra) not to exceed 1.6um
Sharp edges to be broken to 0.1 to 0.3
All dimensions to be within 0.1
All faces to be parallel or square to within 0.25
All diameters to be concentric within 0.1
All Radii to be 0.5 to 0.1
All chamfers to be 0.5x45degree
Revision
0.1
Scale 1:2
Units
mm
Mass
N/A
Title Yoke 2
Drawing No
Rig_Yoke 2
Comments
Date
Name
Drawn 12-04-2017 Gai
Checked Andy
Apprvd
Material EN8
Treatment
Stock
Surface Treatmt
3 OFF
M6x0.75 - 6H
THREAD DEPTH16.00
30
150
30
15
20
23.5
73.5
123.5
147
3 OFF
Ø6.60 ↧ 20.00
⌀ 12.60 X 90.0°

B.6. Yoke Bar.

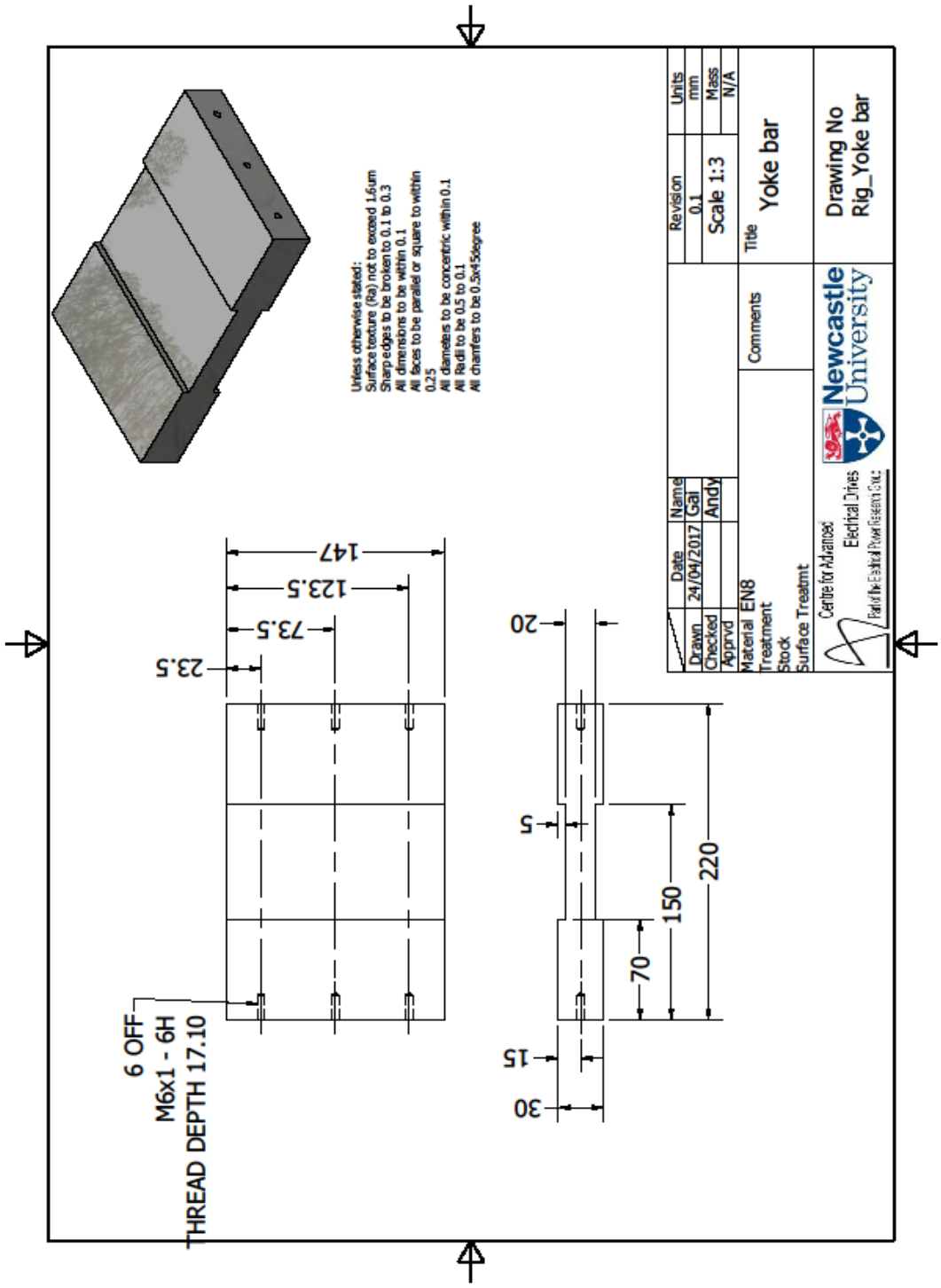
Unless otherwise stated:
Surface texture (Ra) not to exceed 1.6um
Sharp edges to be broken to 0.1 to 0.3
All dimensions to be within 0.1
All faces to be parallel or square to within 0.25
All diameters to be concentric within 0.1
All Radii to be 0.5 to 0.1
All chamfers to be 0.5x45degree
Revision 0.1
Units mm
Scale 1:3
Mass N/A
Title Yoke bar
Drawing No Rig_Yoke bar
Date Name
Drawn 24/04/2017 Gal
Checked Andy
Apprvd
Material EN8
Treatment
Stock
Surface Treatmt
Comments
Newcastle University
Centre for Advanced Electrical Drives
Part of the Electrical Power Research Group
147
123.5
73.5
23.5
6 OFF
M6x1 - 6H
THREAD DEPTH 17.10
20
5
150
220
70
15
30

B.7. DE Bearing Housing.

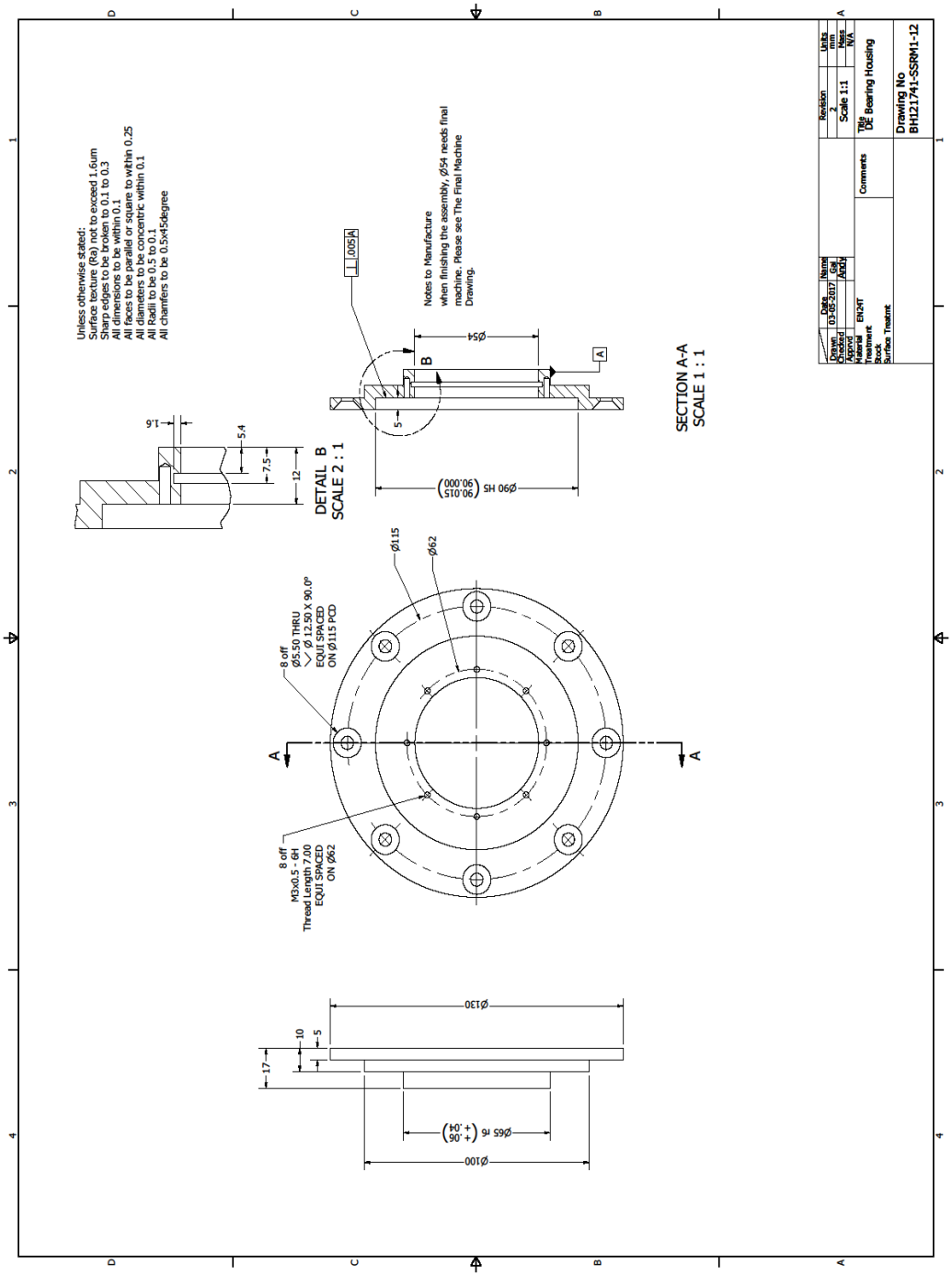

B.8. NDE Bearing Housing.

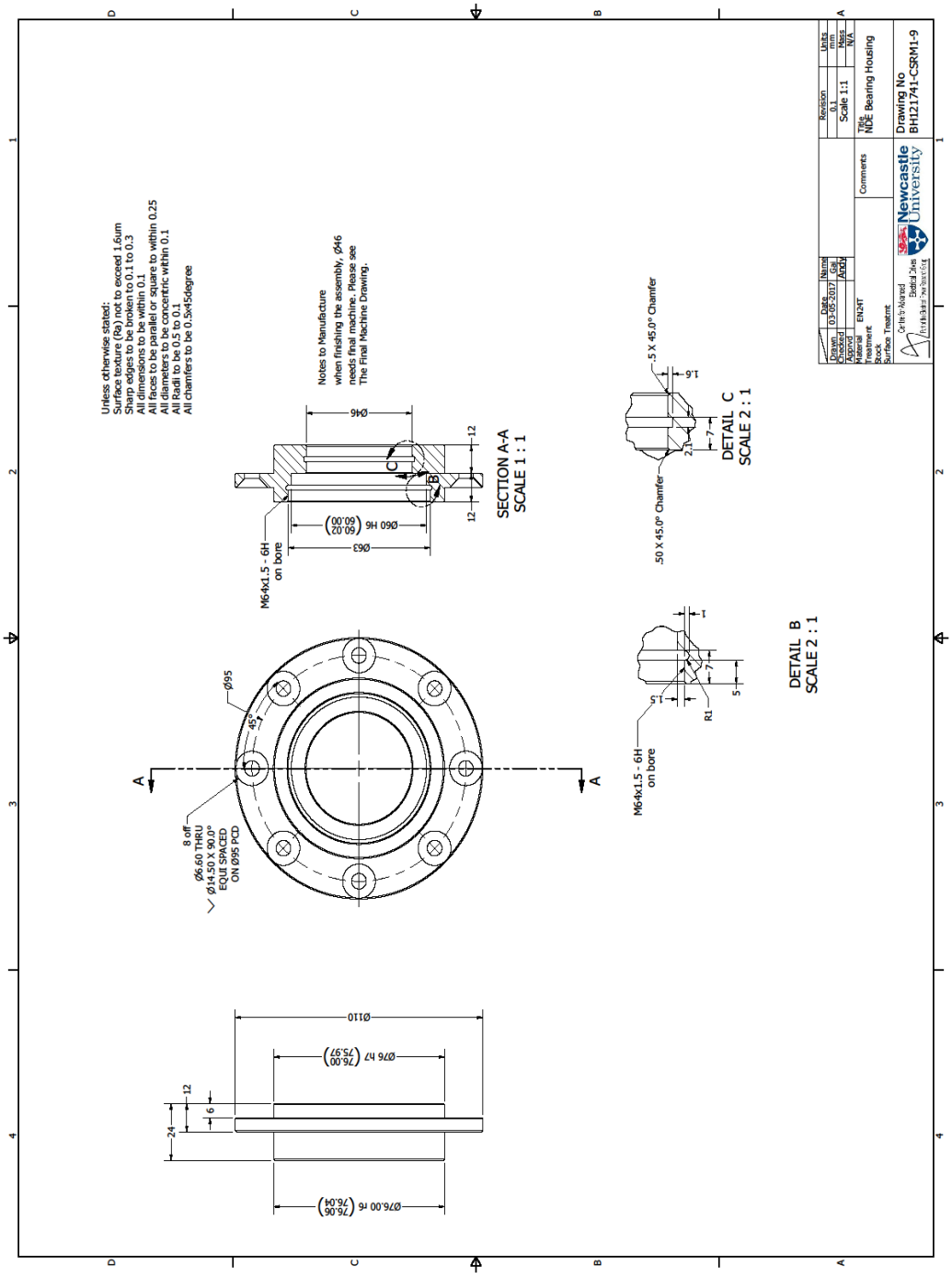

B.9. Retaining Ring.